Defect chemistry of heterointerfaces in ion conducting oxides

Sarmad W. Saeed

Dissertation for the degree of Philosophiae Doctor

Department of Chemistry
Faculty of Mathematics and Natural Sciences

UNIVERSITY OF OSLO

2019

Preface

This thesis is submitted in partial fulfilment of the requirements for the degree of Philosophiae Doctor (Ph.D.) at the Department of Chemistry, Faculty of Mathematics and Natural Sciences, University of Oslo, Norway. The work has been carried out at the Centre for Materials Science and Nanotechnology (SMN) in the Group for Electrochemistry during the period August 2013 to July 2019, under the supervision of Prof. Truls Norby, Dr. Tor S. Bjørheim and Prof. Reidar Haugsrud.

I would like to thank my three supervisors for their encouragement, and for all the valuable discussions, especially in the last few months. I would also like to thank all students and colleagues at the Group for Electrochemistry, who contributed for a fantastic work environment.

Finally, my biggest thanks go to my family for always supporting me, and for always being there when needed.

Oslo, July 2019

Sarmad W. Saeed

Summary

Significant space-charge effects can result at the interfaces between materials that exhibit different electronic structure and/or defect chemical properties. Such effects may lead to for instance enhanced charge carrier concentrations, and thus improved electrical conductivity, or enable mass storage in nanostructured materials. A fundamental understanding of the underlying physicochemical properties of such heterointerfaces is crucial to control and improve the functional properties of nanomaterials. The main objective in this work is to adress the thermodynamics underlying the electrostatic potential difference, which determines the concentration profiles of charged defects across interfaces between different materials.

Ab initio energy and phonon calculations have been employed to obtain the free energy and entropy of defect formation in the considered bulk materials. To compare the relative stability and determine the defect segregation energies across interfaces between different materials, a simple and computationally effective model has been developed. In addition to the defect formation energies in bulk, the model only requires the ionization potential of the perfect oxide, which can be obtained from a single-shot DFT calculation, and thus allows high throughput calculations and screening over a wide range of materials and interfaces.

The defect chemistry of interfaces is mainly governed by two parameters; the defect concentration in the bulk materials and the electrostatic potential difference across the interface, where the latter is dependent on the relative stability of defects in the joining materials. A model system that has been thoroughly studied in this work, is the interface between $BaZrO_3$ and $SrTiO_3$. This system has been investigated due to the similar atomic structure yet different defect chemistry of the two materials, which results in various scenarios as a function of temperature. While acceptor-doped $BaZrO_3$ is dominated by protons in the form of substitutional hydroxide ions ($OH_O^{\bullet}$) as majority charge compensating defect at low and intermediate temperatures, and by oxygen vacancies ($v_O^{\bullet\bullet}$) at high temperature, $SrTiO_3$ is dominated by $v_O^{\bullet\bullet}$ at temperatures higher than 200 K (*i.e.* at all practical temperatures). At conditions where both materials are dominated by the same defect, the electrostatic potential difference across the interface, Φ, is determined by the segregation energy of the dominating defect, and its temperature dependency is given by the segregation entropy. (Here, segregation refers to transfer of defects from the near interface region of one material to that in another material.) For this system, the energies for segregation of $OH_O^{\bullet}$ and $v_O^{\bullet\bullet}$ to $BaZrO_3$ are −0.58 and

−0.64 eV, respectively, and the segregation entropies are 10 and −40 J/mol K. Consequently, Φ is fairly constant at low temperature, exhibiting a value of −0.58 V. At high temperature or dry conditions, Φ exhibits a strong, positive temperature dependence (*i.e.* causes Φ to become less negative) and reaches −0.25 V at 600 K. At intermediate temperature, difference in the defect structure of the two materials results in a rapid change in Φ. In all cases, the concentration of all positive defects is enhanced in the space-charge zone in $BaZrO_3$ and reduced in $SrTiO_3$. Since the diffusivity of $OH_O^\bullet$ is higher than that of $v_O^{\bullet\bullet}$, the total ionic conductivity in heterostructures and nanocomposites of acceptor-doped $BaZrO_3$ and $SrTiO_3$ will be significantly higher than that of the individual materials, owing to the overall increase in the concentration of $OH_O^\bullet$.

Large difference in the concentration of defects in the bulk materials can significantly affect Φ – therefore, the influence of substitutional (homogeneous) doping, which determines the defect concentration in the bulk, has been addressed by considering the interfaces between acceptor-doped $BaZrO_3$ and donor-doped or undoped $SrTiO_3$. The defect structure of donor-doped $SrTiO_3$ is dominated by electrons under reducing conditions, which makes it attractive as negative electrode (negatrode) in electrochemical cells, or as electronic conductor in composite based hydrogen separation membranes, due to its high electronic conductivity. These applications rely on enrichment of ionic and electronic charge carriers in the space-charge layer; however, the low activity of $OH_O^\bullet$ and $v_O^{\bullet\bullet}$ in $SrTiO_3$ causes Φ to be large and positive. Consequently, both defects are depleted, suggesting that composites between donor-doped and acceptor-doped oxides are unsuitable in these applications. Nevertheless, depletion of electrons and $OH_O^\bullet$, which exhibits a strong temperature dependence, corresponds to a job-sharing process where H_2 gas is released. Thus, such interfaces can be used as H_2 (or O_2, under dry conditions) storage system. At 400 K, a charge of 0.44 C/m^2 can be reversibly stored as $OH_O^\bullet$ deficiency. For a temperature change of 300 K, it is estimated that ~40 kg (~8 L) of oxide composite is needed to store 1 kg of H_2.

Reversal of the sign of Φ occurs also at the interface between undoped $SrTiO_3$ and acceptor-doped $BaZrO_3$ due to low activity of $OH_O^\bullet$ and $v_O^{\bullet\bullet}$ in the former. Although Φ is as low as 0.01 V at 600 K, which leads to a negligibly small enrichment of all positive defects in $SrTiO_3$, this example illustrates that decoupling transporting and charge compensating (*i.e.* dopant) defects may be possible even when the defect concentration in the bulk is low, and the segregation enthalpies are positive. Reversing the doping levels of the two materials results in substantial

transfer of defects across the interface; the amount of charge in undoped $BaZrO_3$ is 0.25 C/m^2 at 600 K, increasing with decreasing temperature. As such, the high defect concentration and absence of dopant in $BaZrO_3$, which thus eliminates the association between the charge carriers and the dopant, result in improved conductivity. A conservative estimate, assuming an activation energy for $OH_O^{\bullet}$ mobility of 0.20 eV, yields a conductivity that is four orders of magnitude higher in heterogeneously doped $BaZrO_3$ than in Y-doped $BaZrO_3$ at room temperature. This is substantially higher than what can be achieved in homogeneously doped materials – A-site acceptor-doping of $BaZrO_3$ can reduce the activation energy for $OH_O^{\bullet}$ transport by 0.1 eV, which is significantly lower than the reduction of 0.3 eV for the heterogeneously doped material.

The absolute formation energies of $OH_O^{\bullet}$ and $v_O^{\bullet\bullet}$ in a wide range of oxides have been calculated, and used to predict a correlation of the segregation energies of these species with the physical properties of the solids. It is shown that the segregation energies of these species correlate with, and thus can be estimated from, the ionization potential of the bulk oxides, and thus provide a predictive tool in the search for materials couples with specific interface defect chemistries.

The interfaces between $BaZrO_3$ and Ni, Pd, Pt, Cu, Ag, or Au have been considered in an attempt to connect the formation of space-charge layer at the electrode/electrolyte contact to the electrode resistance. The results presented here show that for most metals, space-charge formation does not limit the performance of electrodes at typical operation temperature of electrochemical cells. However, at lower temperatures, charge carrier depletion at the contact may contribute to or dominate the charge transfer resistance of the electrode. Finally, the prospects for utilising the space-charge at metal/oxide interfaces in electrochemical capacitors, and to conduct "thermo-electrochemical" H_2O splitting, are discussed.

Altogether, this work addresses the thermodynamics and characteristics of space-charge formation at heterogeneous interfaces, and explores the strategies to improve the functional properties of ionic solids beyond what can be achieved in single-phase materials.

Contents

1 Introduction

There is no doubt that the technological development the world has experienced during the last century can be traced back to the development of advanced functional materials, which find a wide range of applications in, for example, information and communication technology, sensors, medicine and energy harvesting and conversion devices.

In order to improve the functional properties of materials, a fundamental understanding of the underlying physical phenomena is required. The functional properties of solid oxides, such as electrical conductivity and catalytic activity, are usually determined by the type and concentration of the defects present in the material. The thermodynamic description of defect equilibria and kinetics is provided by defect chemistry, which makes the foundation of the topics treated in this thesis.

At any temperature, there is a non-zero concentration of defects in otherwise perfect crystals, owing to the configurational entropy arising from the formation of defects. In ionic and mixed conductors, which find application in *e.g.* fuel cells, electrolysers, gas separation membranes and sensors, a high concentration and fast mobility of certain ionic defects is desired. Traditionally, the concentration of defects is altered through doping (substituting of regular ions with aliovalent ones), which may allow the control of type (*i.e.* *p* or *n*) and concentration of the mobile charge carriers. Still, doping may not always be the solution to enhanced concentration. For instance in $LaNbO_4$, the solubility limit of the acceptor dopant CaO is only 0.5-1 % at the high temperatures used in phase formation and sintering.[1] A drawback of traditional doping is the possibility for defect association between $OH_O^{\bullet}$ (or $v_O^{\bullet\bullet}$) and the frozen-in dopant that increases the activation energy of charge carrier transport. This effect can have a very negative impact for proton conductors as these are considered as low to intermediate temperature electrolytes. For example, the activation energy for proton mobility in $BaZrO_3$ is measured to 0.45 eV. As much as 0.29 eV of this is due to association with the Y dopant [2-4]. Thus, the proton conductivity of $BaZrO_3$ may become much higher if the association energy can be reduced or eliminated.

In this thesis, the potential of defect chemistry at heterogeneous interfaces (here hetero refers to different materials rather than different physical states), which introduces an additional degree of freedom, is explored and constitutes the main topic. To illustrate this, consider the simplest type of interfaces; grain boundaries (which are homogeneous interfaces) in polycrystalline materials. In many ion conducting oxides such as acceptor-doped CeO_2 and $BaZrO_3$, the grain boundary core is positively charged due to preferred segregation of $v_O^{\bullet\bullet}$ and $OH_O^{\bullet}$ [5-7]. Consequently, charge compensating space-charge zones in the vicinity of the grain boundary core are formed. In these zones, the concentration of positive charge carriers is depleted, and that of negative carriers is increased. Since the total electrical conductivity involves charge carriers crossing grain boundaries with reduced defect concentration, the observed total conductivity of a ceramic polycrystalline sample is often orders of magnitude lower than in a corresponding single crystal [5, 8-11]. However, reducing the particle size to a few nanometres can cause up to four orders of magnitude increment in the conductivity in the case of CeO_2.[7] This increment is a result of the high grain boundary to bulk volume ratio and charge carrier inversion in which fast electrons become dominating (in the space-charge region). As such, the grain boundary acts as a higher dimensional (donor) dopant. This kind of doping can be beneficial in reducing/eliminating the effect defect association poses on the electrical conductivity.

Interfaces between different materials give raise to several interesting effects such as ferromagnetism in nonmagnetic materials [7, 12, 13], metallicity [14] and superconductivity in electrical insulators [15], improved catalytic activity compared to the individual phases [16], and orders of magnitude higher ionic conductivity [17, 18]. However, in this work we focus on the possibilities interfaces provide for enhancing the transport properties in proton conductors and mass/charge storage in nanostructured chemical capacitors. **Fig. 1** is adapted from reference [19], and shows a few examples of job-sharing storage of Li (**a** and **b**) and H_2 (**c**) in battery materials, artificial electrodes consisting of ultrathin layers of ion and electron conductors where space-charge overlap results in high, nearly homogeneous carrier concentrations (**d**), and excess and deficiency storage of silver at $RbAg_4I_5$-graphite interfaces (**e** and **f**).

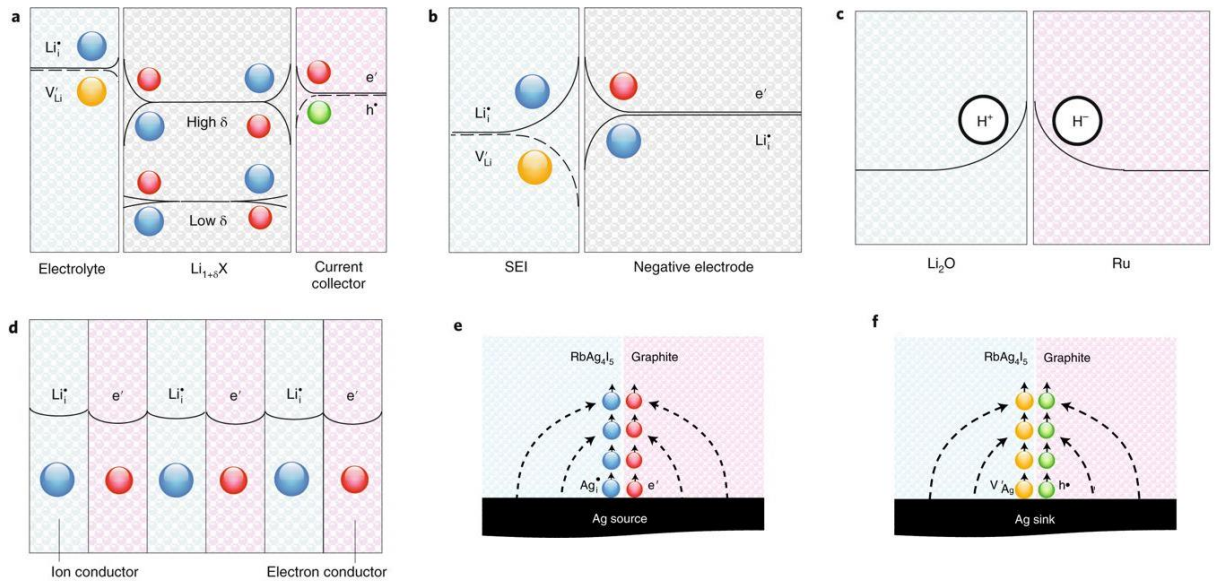

Fig. 1. Examples that lead to job-sharing situations such as storage of Li (a and b), H_2 (c), mixed conductivity (d), and different types of storage of Ag, *i.e.* excess (e) and deficiency (f) storage. Adapted from reference [19], reprinted with permission from Nature Publishing Group.

In particular hydrogen storage in oxides is considered challenging due to thermodynamic limitations. In this context job sharing, in which the constituents of a species are stored separately in either of the materials, may be beneficial. For instance, one can attempt to store H_2 as $OH_O^{\bullet}$ in a proton conductor and e^- in an electron conductor, which may also be beneficial in electrodes and gas separation membranes that rely on ambipolar/mixed conductivity. Such storage has been reported for composites of Li_2O and Ru [20], where neither of the individual phases can store H_2. In the thesis, interfaces between a number of materials are considered but the main focus is on the interfaces between $BaZrO_3$, $SrTiO_3$, CeO_2 and Pt. $BaZrO_3$ is one of the state-of-the-art proton conductors that has attracted much interest due to its high bulk conductivity, while $SrTiO_3$ is a well-studied model material that becomes oxide ion conducting upon acceptor doping and electron conducting upon donor-doping. CeO_2 is an excellent oxide ion conductor that becomes mixed ionic-electronic conducting under reducing conditions owing to the formation of electron polarons due to reduction of Ce atoms. Pt is considered due to its wide use as electrode, current collector and/or catalyst in solid state ionics research.

The promise of interfaces as a tool for tailoring the functional properties of solid state ionic conductors was first realized in LiI containing dispersed Al_2O_3 particles.[17] A significant increase in the conductivity was observed that could not be interpreted in terms of conventional doping. Later on, a wide range of halides were studied [18, 21-26], and the change in conductivity was ascribed to the formation of space-charge layers that resulted from differences

in relative stability of defects in the two components of a composite. In general, due to thermodynamic reasons, ions are transferred across the interface to create (mobile) interstitial defects, leaving behind (mobile) vacancies. Thus, the concentration of defects in the vicinity of the interface is significantly higher than in bulk, which results in conductivities that may be several orders of magnitude higher than in each of the individual materials. It was also found that accumulation of interstitial defects in the space-charge zone can be beneficial for enhancing the Li storage capacity of Li-ion battery materials, as has been shown for Li/RuO_2 [27] and LiF/Ti [28] and a number of other systems [21, 22, 29].

The defect chemistry of heterogeneous interfaces involving proton conducting oxides has not been much studied. Among the few studies on such interfaces are the works by Yang *et al*. [30] and Foglietti *et al*. [31], who reported enhanced conductivity at the interface of $BaZrO_3$ on $NdGaO_3$ substrates. The increased conductivity was ascribed to decrease in the activation energy for the mobility of protons at misfit dislocation. Chan *et al*. [32] studied composites of $CsHSO_4$ and TiO_2 or SiO_2 experimentally. A substantial jump in the conductivity of the composites were observed near room temperature, resembling the transition to the superprotonic phase of $CsHSO_4$ that occurs at significantly higher temperatures. NMR experiments showed that protons were transferred from the sulphate to titania which allows rotation of the SO_4 tetrahedra as in the superprotonic phase due to the formed proton vacancies. The formation of space-charge layers due to proton transference across the interface was supported by a computational study performed by Haverkate *et al*. [33]. In another computational study, Polfus *et al*. [34] considered the interface between $BaZrO_3$ and MgO. The authors found the segregation to uncoordinated O ions in the first MgO plane to be very favourable, leading to accumulation of protons in that plane and subsequent depletion of positively charged defect in $BaZrO_3$. The authors applied a simplified space-charge model where the segregation of $v_O^{\bullet\bullet}$ and $OH_O^{\bullet}$ from MgO to $BaZrO_3$ was neglected, despite of negative segregation energies, due to low concentration of these defects in bulk MgO.

Metals are often used as electrodes in electrochemical devices such as fuel cells and electrolysers; however, little is known about the role of space-charge layers between metals and solid ionic conducting oxides in these devices, and the dependence of the space-charges on temperature and atmospheric conditions at such interfaces. In that respect, one can recall the work by Matsumoto *et al*. [35] who reported an order of magnitude decrease in the electrical conductivity of Y-doped $SrZrO_3$ containing dissolved platinum upon reduction. This behaviour,

which was reversible upon reoxidation, was interpreted in terms of negative space-charge layers (where predominating positive charge carriers are depleted) around Pt nanoparticles that form under reducing conditions and dissolve in oxidizing conditions. Tong *et al*. [36], on the other hand, reported somewhat higher conductivity in Y-doped $BaZrO_3$ loaded with Pd nano-particles than in the Pd-free specimen. Further, Caldes *et al*. [37] reported an order of magnitude improvement in the electrical conductivity of Y-doped $BaCeO_3$ containing Ni-nanoparticles. The conductivity improvement was interpreted in terms of space-charge layers with enhanced proton concentration around the Ni-particles and improved catalytic properties that facilitate proton incorporation.

Computationally, Kasamatsu *et al*. [38, 39] studied the interface between ZrO_2 and Pt, assuming interface potentials of 1-3 V. The authors concluded, however, that the concentration of the majority defect $v_O^{\bullet\bullet}$ is enhanced in reducing conditions, and reduced in oxidizing conditions – contrary to the measurements performed by Matsumoto *et al*. [35] for the $Pt/SrZrO_3$ system. In an attempt to address the stability of protonic defects at the interfaces of $BaZrO_3$, Tauer *et al*. [40] carried out DFT calculations on surfaces and interfaces between $BaZrO_3$ and a range of metals. In the first atomic plane of the oxide, under the metal cluster, protons were somewhat more stable, in the case of Pt and Pd, than in bulk. In subsequent planes, no further stability was observed. These results are in line with the results obtained for Pd, by Malagoli *et al*. [41].

As the brief literature review above shows, interfaces involving proton conducting oxides are far less studied than for instance their halide counterpart, and the few studies that exist do not provide in-depth analysis of the interface chemistry and the effect of for instance choice of materials. Knowledge of the interface defect chemistry as a function of control parameters such as temperature, atmosphere and doping type/level is valuable for the development of composite electrolytes, electrodes and gas separation membrane that may exhibit superior performance.

While the experimental studies mainly report the observed physical properties without in-depth analysis of the interface chemistry, the computational studies suffer from the use of simplified models where the phase boundary is treated as grain boundary neglecting the difference in defect affinity across the interface, or only provide defect energetics without further analysis of the interface defect structure.

The thesis is based on five manuscripts that treat different aspects of the defect chemistry of bulk, homogeneous and heterogeneous interfaces and their application. The main focus is on

the development the theory/methodology to describe heterogeneous interfaces involving oxides with complex defect structure. The results are obtained from first principles calculations, which in combination with thermodynamic modelling is used to predict the defect chemistry of these interfaces at finite temperatures and pressures. In the next chapter, a brief review of the theory central for this work is provided before the manuscripts are presented in Chapter 3. A broader discussion and conclusions are presented in Chapter 4 and 5, respectively.

2 Theoretical approaches and methodology

In this chapter, a brief overview of the most central theoretical aspects is provided. The main focus is on density functional theory (DFT), which, besides thermodynamic modelling, is the main tool used to obtain the results presented in this thesis. The rest of this chapter is devoted to the thermodynamics of defect formation in bulk and near interfaces. The methodology used to obtain the results is presented in brief throughout the chapter.

2.1 DFT

The development of first principles calculations together with the increasing availability of high performance computers have made computational materials science increasingly popular. Being powerful predictive tools, DFT and other computational approaches are today at the fore in the development and search for new materials.

To get a brief insight into the theory underlying DFT, we need to consider a simplified form of Schrödinger equation, namely the time independent, non-relativistic form:

$$\hat{H}\psi(\mathbf{R}_1, \dots, \mathbf{R}_M, \mathbf{r}_1, \dots, \mathbf{r}_N) = E\psi(\mathbf{R}_1, \dots, \mathbf{R}_M, \mathbf{r}_1, \dots, \mathbf{r}_N) \quad (1)$$

where H, E and ψ are the Hamiltonian operator, energy of the system and wave function, respectively. The latter is a function of the position of all nucleus and electrons ($\mathbf{R}_i$ and $\mathbf{r}_j$, respectively) in the system. Solving this equation involves a 3(M+N) dimensional problem, where M and N denotes the number of nucleus and electrons, respectively. An important observation that simplifies this equation considerably is that the mass of protons/neutrons is 3 orders of magnitude higher than the mass of an electron. Therefore, electrons would respond much faster to a change in their surroundings than nuclei do, and consequently the Schrödinger equation can be solved for the electrons in the field of fixed atomic nuclei. This splitting of Schrödinger equation in two parts is known as the Born-Oppenheimer approximation, and corresponds to setting the kinetic energy of the nuclei to zero. With this approximation, Eq. (1) becomes:

$$\left[\frac{h^2}{2m}\sum_{i-1}^{N}\nabla_i^2 + \sum_{i-1}^{N}V(\mathbf{r}_i) + \sum_{i-1}^{N}\sum_{j<i}^{N}U(\mathbf{r}_i,\mathbf{r}_j)\right]\psi(\mathbf{r}_1,\ldots,\mathbf{r}_\mathrm{N}) = E\psi(\mathbf{r}_1,\ldots,\mathbf{r}_\mathrm{N}) \quad (2)$$

where m and $\mathbf{r}$ are the mass and position of electron *i*, respectively. The terms in brackets represent the kinetic energy of electron *i*, the interaction energy between electron *i* and the set of fixed nuclei and the interaction energy between electron *i* and *j*, respectively. Eq. (2) can be further simplified by approximating the wave function as a Hartree product, $\psi(\mathbf{r}_1,\ldots,\mathbf{r}_\mathrm{N}) = \psi(\mathbf{r}_1)\psi(\mathbf{r}_2)\ldots\psi(\mathbf{r}_\mathrm{N})$, and thus expressing the Schrödinger equation in terms of one-electron wave functions. Despite of being simpler, the wave function still is 3N dimensional and thus computationally demanding to solve (23 000 dimensions are required to describe a nanocluster of 100 Pt atoms). Still, the major challenge is the electron-electron interaction term, which makes the equation a many-body problem. Consequently, it is challenging to find the wave function of one electron without simultaneously knowing the wave functions of all other electrons. An observation that can help to circumvent this, and that is at the core of the development of DFT, is that the wave function tells the probability of finding the electrons at certain positions, which is closely related to the electron density. The latter can be expressed in terms of one-electron WF.

$$n(\mathbf{r}) = 2\{\psi\} = 2\sum_i \psi^*(\mathbf{r})\psi(\mathbf{r}) \quad (3)$$

Thus, it is to be expected that the electron density can describe all the properties of a given system. This was first realised by Hohenberg and Kohn [42], who formulated two theorems that constitute the bases of DFT. The first theorem states that the potential, and hence the total energy, of the ground state is a unique functional of the electron density, while the second theorem defines an important property of the functional; the electron density that minimizes the energy of the functional corresponds to the solution of the Schrödinger equation. The fact that electron density is a function of only 3 variables would significantly reduce the time needed to solve the Schrödinger equation.

The density functional defined by Hohenberg and Kohn can be written as

$$E[\{\psi\}] = E_{known}[\{\psi\}] + E_{XC}[\{\psi\}] \quad (4)$$

where the known part, reads $E_{known}[\{\psi\}] = \frac{h^2}{2m}\sum_i \int \psi^* \nabla^2 \psi d^3r + \int V(\mathbf{r}) n(\mathbf{r}) d^3r + \frac{e^2}{2} \int\int \frac{n(\mathbf{r}) n(\mathbf{r}')}{|\mathbf{r}-\mathbf{r}'|} d^3r d^3r' + E_{ion}$, that can be determined exactly. The term E_{ion} corresponds to the Columb interaction between the nuclei. The $E_{XC}[\{\psi\}]$ term contains quantum mechanical effects such as the exchange energy, which arises from the asymmetric nature of the WF. Moreover, E_{XC} also includes corrections for E_{known}. For example, the Hartree term (the double integral in the expression for E_{known}) includes self-interaction where an electron interacts with it self, which is clearly unphysical. The self-interaction is caused by the fact that the electron at position **r'** is also part of the total electron density n(**r**).

Even though the Hohenberg-Kohn theorems show that the solution of Schrödinger equation for the ground state can be reduced to three dimensions, they do not provide a way to find the solution. Thus, it is not sure that solving Eq. (4) would be easier than solving Eq. (2) since finding the kinetic energy requires knowledge of the full wave function. The breakthrough came when Kohn and Sham [43] found an approximate XC-functional and showed that Eq. (4) can be expressed as a set of equations involving one-electron wave functions, according to

$$\left[\frac{h^2}{2m}\nabla^2 + V(\mathbf{r}) + V_H(\mathbf{r}) + V_{XC}(\mathbf{r})\right]\psi_i(\mathbf{r}) = \varepsilon_i \psi_i(\mathbf{r}) \tag{5}$$

This equation differs from Eq. (2) in the sense that it only depends on one-electron WF and the absence of the summation. It should be noted that these are Kohn-Sham wave functions, which differ from the real one-electron wave function.

The true exchange correlation functional in Eq. (5) is unknown. There is however one case where it is known exactly, namely for the homogeneous electron gas (HEG), also called jellium. In a HEG, the exchange energy can be determined exactly, and so does the correlation energy in the limits of very high or low electron density. For intermediate cases, approximated correlation energy can be obtained from Monte-Carlo simulations (which yields results close to exact). Although this may seem useless at first, since the electron density varies very much within an atom/molecule, it turns out to be a good approximation creating the foundation for the so-called local density approximation (LDA) functional. In LDA, the electron density at each point in the space is locally treated as a HEG, allowing the application of KS equations. LDA gives adequate/reasonable results for systems without strong local variation in the electron

density; however, it suffers from overestimating binding energies and hence underestimating lattice constants, besides failing to predict correct metallic ground states [44].

In real systems the electron density on a local scale can vary significantly, so including the local gradient in the functional (as is done in the generalized gradient approximation, GGA) could present a significant improvement over LDA. Since there are many ways to include the gradient, there exist many distinct GGA functionals that have been developed to address different properties. The most widely used GGA functional, which is also the one applied in this thesis, was proposed by Perdew, Burke and Ernzerhof (thereof the name PBE) [45]. One may expect that GGA would give improved results compared to LDA since it applies more information. Unfortunately, this is generally not the case. For instance, in contrast to LDA, GGA underestimates the binding energy, and hence overestimates the lattice parameter. Due to over-/underestimation of lattice parameters, LDA and GGA would predict vibrational properties that deviate from experiments. However, in many cases properties are calculated relatively such that errors cancel and reliable results still can be obtained, as for instance when calculating formation entropies of defects.

Both functionals severely fail in predicting the correct band gaps of solids, usually underestimating it by more than 1 eV. There is some discussion whether this is due to the approximations done throughout DFT or if it is due to the fact that DFT is a ground state theory and would fail in describing exited states. Moreover, the two sets of functionals often fail in describing localized states in strongly correlated systems. To circumvent this, post-DFT functionals have been developed. The simplest of them being DFT+U, in which an on-site repulsion term, U, is added to the LDA or GGA functionals. The U parameter is usually determined semi-empirically and set depending on the property of interest, for instance by choosing a U value that gives correct oxidation/reduction enthalpy. It is also possible to determine the U parameter ab initio, choosing a value that gives piecewise linear behaviour (as have been done in this work). This works however best for localised electronic states. Generally, DFT+U yields slightly better bandgaps and is often able to predict localized states and hence magnetic ordering.

Next in complexity, are hybrid functionals [45-47] where a portion exchange in the DFT calculation is replaced by a corresponding amount of exact exchange from Hartree-Fock based calculations. These functionals generally result in bandgaps close to experimental for a wide

range of materials and provide good prediction of most properties even for strongly correlated systems. A drawback is that they are computationally demanding.

The best description of materials properties can be obtained from GW based quasi particle calculations, in which the exchange-correlation potential in DFT is replaced by the many-body self-energy. GW calculations are very costly and would be difficult to apply for large, defective systems.

In addition to the included references, the theory in this section is based on the book by Sholl and Steckel [48].

2.2 Implementation of DFT

The use of DFT as a computational tool does not require a complete knowledge of all the theoretical details underlying it. In practice, a DFT code is used where one or several functionals are implemented. Then performing a calculation is a matter of specifying/supplying a set of parameters such as the functional to be used, structural information and a range of other parameters. These and some possible pitfalls and sources of errors that the reader should be aware of are briefly mentioned below.

The first choice to be done is specifying the method to describe the electron density. In KS equations, the electron density can be described using localized or extended functions. The former decays rapidly to zero and therefore is more suitable for isolated atoms and molecules, but can also be used for periodic structures. The disadvantage of localized functions is related the difficulty of convergence of the electronic structure during structural relaxation due to changing basis set; on the other hand, they present an advantage in calculating aperiodic structures such as surfaces. Extended functions are usually based on plane waves (as in VASP [49-52], the DFT code used in this work), and are more suitable for calculations involving periodic structures, making them popular in materials science. In such calculations, it is assumed that crystals are infinite in all spatial directions, which has some disadvantages when dealing with charged defects.

The periodicity of solids makes it possible to solve the KS equations in reciprocal space, with the advantage that the energy can be evaluated at a limited number of k-points in the first

Brillouin zone. The number of k-points (which is one of the parameters to be specified) needed is dependent on the size of the system – the larger the unit cell (supercell) is, the fewer k-points are needed.

In order to make DFT calculation fast, the plane wave basis set should be as small as possible, but at the same time big enough to yield reliable results. The size of the basis set is defined by a cut-off energy. The larger the variation in electron density on a local scale, as the situation is close to core, the higher the cut-off energy needs to be. In this context, it is worth noticing that core electrons take no/little part in chemical bonding and hence can be considered inert. This leads to the frozen core approximation, in which core electrons are replaced by an effective potential, significantly reducing the size of basis set. In practice, one needs to check the convergence of total energy – or the property of interest – with respect to cut-off energy and k-mesh density.

2.3 Point defects

Defects represent deviation from the perfect structure of a crystal and can be zero dimensional as represented by point defects (such as vacancies, interstitials and localized electrons and holes) or higher dimensional such as dislocations, grain boundaries, interfaces and ordered collections of interacting point defects. This thesis mainly deals with point defects in bulk and in the vicinity of interfaces between different solids, *i.e*. two dimensional defects.

Point defects may form intrinsically, *i.e*. through internal reactions, or extrinsically, in which defects form through reactions involving the surroundings. An example of the former is the Frenkel reaction where a lattice ion occupies an interstitial site and leaves behind a charge compensating vacancy. On the other hand, formation of oxygen vacancies, which is responsible for oxide ion transport, is a good example of external reactions that are often encountered in oxides:

$$O_O^{\times} \rightleftarrows v_O^{\bullet\bullet} + 2e' + {}^{1}/_{2}\, O_2(g) \qquad (6)$$

Under ideal conditions, the corresponding equilibrium constant can be expressed in terms of equilibrium concentrations, which, further can be expressed by standard thermodynamic parameters that can be measured experimentally:

$$K_{\mathrm{red}} = X_{\mathrm{v_O^{\bullet\bullet}}} X_{e'}^2 X_{\mathrm{O_O^{\times}}} p_{\mathrm{O_2}}^{1/2} = \exp\left(-\frac{\Delta G_{\mathrm{red}}^{\circ}}{k_B T}\right) = \exp\left(-\frac{\Delta H_{\mathrm{red}}^{\circ}}{k_{\mathrm{B}} T}\right) \exp\left(\frac{\Delta S_{\mathrm{red}}^{\circ}}{k_{\mathrm{B}}}\right) \quad (7)$$

where X_i, $p_{\mathrm{O_2}}$, ΔH° and ΔS° denote the concentration in site fractions, oxygen partial pressure and standard reaction enthalpy and entropy, respectively. Here $X_{\mathrm{e^-}}$ refer to *n/N*, *i.e.* the concentration of electrons divided by the integrated density of states of the conduction band. ΔS_{red}° represents the vibrational contribution, only. Eq. (7) shows that the concentration of $\mathrm{v_O^{\bullet\bullet}}$ and electrons is affected by changes in the surroundings (*e.g.* a change in $p_{\mathrm{O_2}}$). The concentration of defects can also be affected through the introduction of aliovalent substituents, *i.e.* doping. Upon doping with effectively negatively charged ions (lower valent ions), the concentration of all negatively charged defects, except for the dopant itself, decreases, while that of positively charged defects increases. As an example, doping $BaZrO_3$ with Y results in a substantial increase in the concentration of $\mathrm{v_O^{\bullet\bullet}}$. In the presence of water vapour, protons ($\mathrm{OH_O^{\bullet}}$) may be incorporated in the oxide through hydration of the $\mathrm{v_O^{\bullet\bullet}}$, leading to the protonic conductivity that is observed at low temperatures in acceptor-doped $BaZrO_3$. Whether $\mathrm{v_O^{\bullet\bullet}}$ or $\mathrm{OH_O^{\bullet}}$ predominates as charge-compensating defect, is determined by the hydration thermodynamics, ΔH_{hydr}° and ΔS_{hydr}°, which are a measure of the relative stability of the two defects.

From DFT, reaction thermodynamics and defect concentrations can be calculated from the formation energy of single defects, which – when calculated at constant pressure – can be expressed as [53]

$$\Delta G_d^f = \Delta G_d^{f,el} + \Delta G_d^{f,vib,atomic} + p\Delta V^f \quad (8)$$

where $\Delta G_d^{f,el}$ is the change in electronic energy due to defect formation (*i.e.* breaking and formation of bonds), $\Delta G_d^{f,vib,atomic}$ corresponds to the vibrational entropy and $p\Delta V^f$ represents the energy due to change in volume upon defect formation. The last term is usually small and can be neglected. The vibrational entropy contribution to the free energy can be evaluated from finite difference phonon calculations (as implemented in for instance the phonopy code [54], which has been used throughout this thesis), where the ions can be assumed non-interacting, harmonic oscillators. For a system of N atoms, the vibrational free energy becomes

$$F_{vib} = \sum_i^{3N} \left[\frac{\hbar\omega(q,\nu)}{2} + k_B T \ln\left(a - \exp\left(\frac{\hbar\omega(q,\nu)}{k_B T} \right) \right) \right] \quad (9)$$

where $\omega(q,\nu)$ is the phonon frequency at wave vector q with band index ν.

The electronic contributions to the formation energy can be obtained directly from the total energies resulting from DFT calculations according to

$$\Delta G_d^{f,electronic} = E_d^{tot} - E_p^{tot} + \sum_i \Delta n_i \mu_i + q(\varepsilon_f + \Delta\epsilon) \quad (10)$$

where the first two terms are the total energies of a supercell containing a defect of charge q and a perfect supercell, while Δn_i is the change in the number of atomic species i, with a chemical μ_i. ε_f is the chemical potential of electrons (Fermi level wrt. the valence band top), while $\Delta\epsilon$ is a correction for the shift in the core potential that is caused by the jellium background involved in the calculation of charged defects. At 0 K, the chemical potential of atomic species such as O and H can be obtained from the total energies of gas molecules, *e.g.* $\mu_O = \frac{1}{2}\mu_{O_2}$. However, due to the shortcoming of DFT when treating small molecules, the total energies of gaseous species are calculated from the energies of isolated atoms, experimental binding energies and ZPEs according to:

$$\mu_O^\circ = \frac{1}{2} E_{O_2} = \frac{1}{2}\left(2E_O^{DFT} + E_{O_2}^{exp,binding} + E_{O_2}^{exp,ZPE}\right) \quad (11)$$

At finite temperature and pressure, the chemical potential becomes

$$\mu_i(T,p) = \mu_i^\circ + H_i(T,p^\circ) - TS_i(T,p^\circ) + k_B T \ln\left(\frac{p_i}{p^\circ}\right) \quad (12)$$

where the enthalpy and entropy can be obtained from thermodynamic tables.

So far the configurational entropy contribution, which is significant, and in fact the main reason why defects (in undoped materials) form, has not been considered. It can be shown that distributing N_d on N lattice sites with $N - N_d$ regular particles results in a configurational entropy that amounts to [55]

$$S_{cfg} = k_B \ln\left(\frac{N_d}{N - N_d}\right) = k_B \ln\left(\frac{c_d}{c_{0,s}}\right) \tag{13}$$

where c_d and $c_{0,s}$ are the concentration of defect *d* and regular particles on lattice site *s*, respectively. The chemical potential can then be written as

$$\mu_d = \mu_d^\circ + k_B T \ln\left(\frac{c_d}{c_{0,s}}\right) \tag{14}$$

which at equilibrium, *i.e.* when the chemical potential is zero ($\mu_{defect} = 0$), gives:

$$\frac{c_d}{c_{0,s}} = \exp\left(-\frac{\mu_d^\circ}{k_B T}\right) = \exp\left(-\frac{\Delta G_d^f}{k_B T}\right) \tag{15}$$

where $\mu_d^\circ = \Delta G_d^f$ since ΔG_d^f is calculated for a single defect.

The concentrations of all defects can now be determined at any partial pressure and temperature. However, two conditions have to be fulfilled; the first is the electroneutrality condition

$$\sum_i q_i c_i = 0 \tag{16}$$

where q_i and c_i denote the charge and concentration of defect *i*, respectively. The summation runs over all charged defects in the material. Usually, only defects with significant concentration need to be considered. The second condition is related to site balance, which is required for correct thermodynamic description of defect reactions:

$$\sum_i c_{i,s} + c_{0,s} = c_s \tag{17}$$

where c_s is the concentration of lattice site s and *i* runs over all defects that reside on site s.

2.4 Defect affinities

The energy levels obtained from DFT are usually calculated with respect to the bulk potential, which is different for different materials. Therefore, segregation energies are typically calculated using a supercell containing the respective materials. An advantage of this method is the inclusion of lattice mismatch (and thus strain effects) which, in principle, may result in more realistic segregation energies. However, lattice parameters obtained from standard DFT calculations often deviate from the experimental values by 1-2 %. Thus, strain effects may be heavily over/underestimated. Moreover, presence of for instance dislocations at the interface – such the case is for $BaZrO_3/SrTiO_3$ heterostructures – may result in less strained interfaces. Another disadvantage of the supercell method – which is of fundamental interest in the search for materials with specific interfacial properties – is the need to perform new calculations for every material couple under consideration, as the difference in lattice mismatch between different material couples affect the obtained segregation energies in a non-systematic way. To circumvent this, it is possible to align the energy levels by considering inner states of common ions, such as O 1s states, which can be considered inert. However, when no common elements are present, such alignment will not be possible. In addition, strain effects are omitted.

In order to compare the stability of defects in different solids, irrespective of material type and composition, the energy levels have to be aligned with respect to a global reference point. This can be done by calculating the defect formation energies with respect to the valence band maximum (VBM) after aligning it with respect to the vacuum level, which represents a global reference. Thus, the formation energy, or more precisely, the *defect affinity*, becomes

$$\Delta G_{\mathrm{d}}^{f} = E_{\mathrm{d}}^{\mathrm{tot}} + E_{\mathrm{p}}^{\mathrm{tot}} + \Delta_{\mathrm{f}} G_{\mathrm{def}}^{\mathrm{vib}} - \sum_{i} \Delta n_i \mu_i(T,p) + q\left(\varepsilon_{\mathrm{VBM,aligned}} + \Delta\epsilon\right) \qquad (18)$$

The main difference between the equation above and Eq. (10), is the replacement of ε_{F} with the aligned valence band maximum, $\varepsilon_{\mathrm{VBM,aligned}}$. Although the bandgap error affects the defect affinity on an absolute scale, the relative stability of defects is unaffected. This has been confirmed by performing several test calculations on various systems where the supercell method was employed. As such, the calculated segregation energies are correct within the accuracy of DFT.

To align the VBM, the ionization potential, IP – which for a solid is the same as the work function – has to be determined through DFT calculations on slabs of the respective materials. Although the IP can be obtained from a single DFT calculation, the presence of band bending and electronic states at the surface makes it challenging to determine the actual VBM position in the slab calculation. Therefore, we use the VBM from a bulk calculation such that

$$IP = U_{vac} - \varepsilon_{VBM} = U_{vac.slab} + U_{diff} - \varepsilon_{VBM} \tag{19}$$

where U_{vac} is the potential of vacuum with respect to bulk and $U_{diff} = U_{bulk} - U_{slab}$, is the difference in the average electrostatic potential of the bulk region in the slab and bulk calculations, as illustrated in **Fig. 2a**. The actual potentials in $BaZrO_3$ are shown in **Fig. 2b**.

The main advantage with the method outlined here, is that the obtained ionization potential/work function is independent of surface related properties such as orientation, relaxation, surface termination and surface adsorbates. Although these phenomena affect the dipole moment at the surface, and hence the experimentally measured ionization potentials of real surfaces, the situation at a solid-solid interface is very different and may as such – at least for coherent interfaces – be better described by the method presented here.

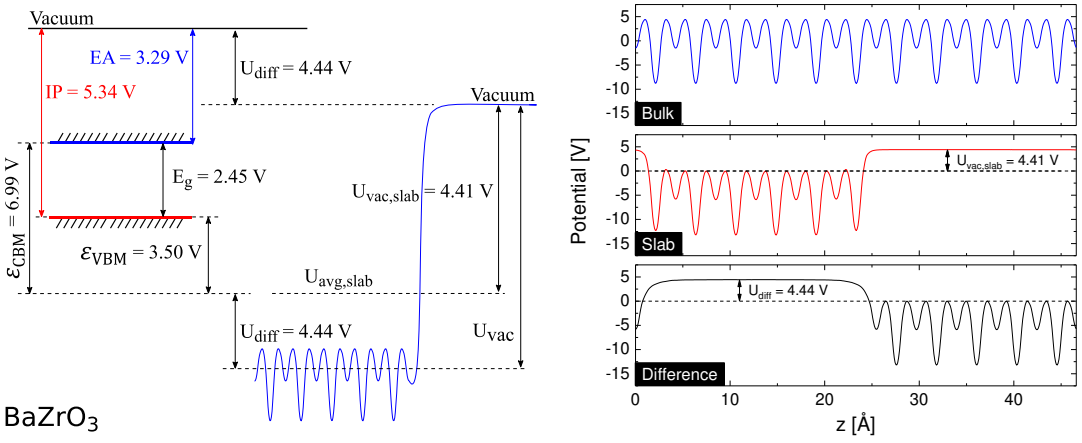

Fig. 2. A schematic representation of the alignment of band structure of $BaZrO_3$ wrt. the vacuum level to determine the ionization potential, IP, (left). The average electrostatic potential in bulk and a slab of $BaZrO_3$ and their difference, (right).

2.5 Interfaces

In this section, a brief presentation of the thermodynamics necessary to describe the defect chemistry of interfaces is provided. Since an interface represents a structural discontinuity, where the stability of defects and lattice ions may differ from that in bulk, defects may segregate to the interfacial plane if there is a gain in the free energy. Moreover, if the segregating defects are charged, an electrical field that limits further segregation is produced. The charge accumulated at the interfacial plane is then compensated by adjacent space-charge layers that are enriched in oppositely charged defects and depleted in defects having the same charge. The amount and type of defects that segregate is governed by the thermodynamics involved. Formation of space-charge layers near interfaces does not rely on segregation to interfacial planes, for instance in the case epitaxial interfaces between materials having the same atomic structure, the defect segregation energy is close to zero. However, the defect affinity of the joining materials may be different and cause defects to segregate across the interface such that charge compensating space-charge layers form. In both cases, the formation of space-charge layers represents deviation from the local electroneutrality that has to be obeyed by bulk. Instead, a global electroneutrality that is governed by Poisson's equation and a set of boundary conditions applies, as described below.

As with point defects, the free energy of space charge formation can be split into several distinct contributions

$$\Delta G_{sc} = \Delta \mathrm{G}_{\mathrm{el,defect}} + \Delta \mathrm{G}_{\mathrm{cfg}} + \Delta \mathrm{G}_{\mathrm{el.stat}} \tag{20}$$

where $\Delta \mathrm{G}_{\mathrm{el,defect}}$ is the difference in electronic energy of a defect at position x and x'. Usually, when treating interfaces it is assumed (as we do throughout thesis) that the SC zone is structurally part of the bulk, and thus formation energies and transport properties remain unaffected. As such, within the same material $\Delta \mathrm{G}_{\mathrm{el,defect}}$ is zero (*i.e.* assuming abrupt boundary conditions), while at the interfacial plane and in the adjacent material, it takes on different values. $\Delta \mathrm{G}_{\mathrm{el,defect}}$ is usually the driving force for defect segregation, and (in the dilute limit) scales linearly with the number of segregating particles. The second term on the right hand side of Eq. (20), $\Delta \mathrm{G}_{\mathrm{cfg}}$, represents the change in configurational entropy that arises from redistribution of defects. This term may be positive or negative, depending on the defect concentrations and available number of lattice sites in the two materials/interfacial plane. The

third term, $\Delta G_{el.stat}$, represents the energy cost arising from the difference in electrostatic potential. This term makes it more energy demanding, the more defects segregate, and sets a limit on the number of segregating species and spatial extent of the SC layer.

We are mainly interested in finding the concentration of defects as a function of distance from the interface. For this purpose, we consider the situation at a heterogeneous interface where a charged defect A is transferred from the position x to x', lying within the same or within the adjacent material (for simplicity, we assume that both materials contain one and the same defect, A). The transference of A can be written in the form of a reaction:

$$A(x) \rightleftarrows A'(x') \tag{21}$$

At equilibrium, the electrochemical potential of A should be constant throughout the interface such that

$$\tilde{\mu}_A(x) = \tilde{\mu}_{A'}(x') \tag{22}$$

which, when expressed in terms of the different contributions mentioned above, becomes

$$\mu_A^\circ + k_B T \ln\left(\frac{c_A(x)}{c_s - c_A(x)}\right) + z\varphi(x) = \mu_{A'}^\circ + k_B T \ln\left(\frac{c_{A'}(x')}{c_s - c_{A'}(x')}\right) + z\varphi(x') \tag{23}$$

where μ_A° is the standard chemical potential of A and $\varphi(x)$ is the electrical potential at position *x*. Rearranging this equation gives the concentration as a function of distance in terms of the electrical potential and segregation energy, $\mu_{\mathrm{seg}}^\circ = \mu_{A'}^\circ - \mu_A^\circ$:

$$c_{A'}(x') = \big(c_s - c_A(x)\big) \exp\left(-\frac{\mu_{A'}^\circ - \mu_A^\circ}{k_B T}\right) \exp\left(-\frac{z\Delta\varphi(x)}{k_B T}\right) \tag{24}$$

where $\Delta\varphi(x) = \varphi(x') - \varphi(x)$ and $\mu_{A'}^\circ = \mu_A^\circ$ if x and x' is within the same material. Thus, within the space-charge layer, the defect concentration increases (or decreases) exponentially towards the interface.

At this point, finding the concentration relies on knowledge of the electrostatic potential, which can be determined through Poisson's equation that relates the potential to the charge density through

$$\frac{\mathrm{d}^2}{\mathrm{d}x^2}\Delta\varphi(x) = -\frac{\rho(x)}{\epsilon} \tag{25}$$

where the charge density, $\rho(x)$, is given by

$$\rho(x) = \sum_i eq_i c_i(x) \tag{26}$$

For our problem with multiple defects, Poisson's equation cannot be solved analytically without making several approximations. However, the equation can be solved numerically (as we have done in this thesis) with appropriate boundary conditions. The first boundary condition required is constant electrostatic potential in bulk:

$$\frac{d}{dx}\varphi(x) = 0\Big|_{x=\pm\infty} \tag{27}$$

In addition, for a heterogeneous interface, constant dielectric function at the interface is required. In absence of charge accumulation at the interfacial plane, it reads

$$\varepsilon\frac{d}{dx}\varphi(x) = -\varepsilon'\frac{d}{dx}\varphi(x)\Big|_{x=0} \tag{28}$$

This condition ensures continuity of the electrical potential.

Since the difference in relative the electrostatic potential across the interface is determined by the difference in chemical potential, a restriction has to be set:

$$\Phi = \varphi(x=\infty) - \varphi(x=-\infty) = \Phi_{\mathrm{rel,interface}} - \Phi'_{\mathrm{rel,interface}} \tag{29}$$

where Φ is the potential across the interface, *i.e*. difference in electrostatic potential between the bulk regions in the two materials. Φ can be obtained by rearranging Eq. (23) and setting $x = \pm\infty$

$$\Phi = \varphi - \varphi' = \frac{1}{z}\left[\left(\mu_{A'}^{\circ} - \mu_{A}^{\circ}\right) + k_B T \ln\left(\frac{c_{A'}[c_s - c_A]}{c_A[c_s' - c_{A'}]}\right)\right] \tag{30}$$

where c_i refers to bulk concentrations. When both materials have the same defect concentration – as the situation is for acceptor doped $BaZrO_3$ and $SrTiO_3$ at low or high temperature – the potential becomes only a function of formation energy difference, normalized by the charge state of the defect.

The situation at a metal/oxide interface can be treated in a similar manner, but with a small modification; the potential drop within the metal can be set to zero, such that $\Phi = \varphi(x = 0)$ in the oxide phase. Otherwise, the same equations as in the case of oxide/oxide interfaces are applied (however, there is no need to evaluate the charge). If an external electric field, φ_{ext}, is applied to the interface, then total electrostatic potential at the interface becomes $\Phi_{ext} = \Phi + \varphi_{\text{ext}}$.

When an external electric field is applied to an ionic conductor using ion blocking electrodes, the charge carriers start to migrate from one electrode to the other. Consequently, chemical polarization occurs as a result of the electric field and blocking nature of the electrodes. At some point, the electrical field produced by the transference of charge carriers completely counteracts the applied field, such that equilibrium is reached. The polarization corresponds to chemical capacitance, and allows storage of electrical energy. The same principle is used in supercapacitors, suggesting that ionic conductors may be suitable as solid-state electrolytes in supercapacitors. The chemical capacitance is given by

$$C = \frac{dQ_{rel}}{dV} \tag{31}$$

where V is the applied voltage and Q_{rel} is the excess charge that is stored in response to the external potential, and is given by

$$Q_{rel} = Q_V - Q_{V=0} = \int_0^{x_b} \rho(x)\mathrm{d}x\Big|_V - \int_0^{x_b} \rho(x)\mathrm{d}x\Big|_{V=0} \tag{32}$$

The energy stored in the capacitor is then obtained by integrating the voltage with respect to charge:

$$E = \int_0^Q V(q)\mathrm{d}q \tag{33}$$

2.6 Electrical transport

The presence of mobile, charged defects in solids gives rise to electrical conductivity that for a defect *i* can be expressed as

$$\sigma_i = Z_i e c_i u_i \tag{34}$$

where $Z_i e$, c_i and u_i denote the charge, concentration and electrical (charge) mobility, respectively. The electrical conductivity increases exponentially with temperature due to both c (given by Eq. (15)) and u being activated processes. At lower temperature where the concentration of defects can be considered frozen in, the conductivity would only be dependent on the temperature dependence of the mobility

$$u_i = u_{0,i}\frac{1}{T}\exp\left(-\frac{\Delta H_{\mathrm{A},i}}{k_\mathrm{B}T}\right) \tag{35}$$

where $u_{0,1}$ and $\Delta H_{\mathrm{A,i}}$ are the pre-exponential term and activation enthalpy, respectively. The activation enthalpy can be viewed as the energy barrier that a defect has to overcome in order to migrate from one site to another. For protons, the apparent $\Delta H_{\mathrm{A,i}}$ is for many perovskites in the range 0.4-0.6 eV. A big fraction of the $\Delta H_{\mathrm{A,i}}$ is caused by trapping – *i.e.* association between mobile and immobile defects of opposite charge. As such the activation enthalpy can be split into a "mobility" term and trapping term; $\Delta H_{\mathrm{A,i}} = \Delta H_{\mathrm{mob,i}} + \Delta H_{\mathrm{T,i}}$. For instance in Y-doped $BaZrO_3$, where the activation energy for proton transport is measured to 0.45 eV, it was found that defect association at lower temperatures is responsible for 0.29 eV [2]. Therefore, the

electrical conductivity would be much higher if defects can be introduced to the material without doping.

The total bulk conductivity of a material is the sum of partial conductivities of all defects. Although, the conductivity is directly proportional the concentration, defects with minor concentration may predominate the total conductivity if their mobility is high. This situation is often encountered at elevated temperatures in oxidizing atmosphere for acceptor-doped oxides where $v_O^{\bullet\bullet}$ are predominating concentration-wise, while the measured conductivity is dominated by electron holes, which are minority defects.

2.7 Uncertainties and limitations

The approximations underlying DFT may lead to some errors in the results. Some of these, such as over/underestimation of lattice parameters and the severe underestimation of bandgap, which enters directly in the calculation of defect formation energies and affects the prediction of localized states, have already been mentioned in Chapter 2.1 and when relevant in subsequent chapters.

The use of periodic boundary conditions for calculations on charged defects has some disadvantages due to charge compensation by jellium background and Coulombic interactions between a defect and its periodic images, which affect the calculated defect formation energies. These effects can be reduced by using a sufficiently large supercell at expense of increased computational time. The jellium background can be corrected for by considering the change in the electrostatic potential of ions far from the defect upon introducing charged defects.[56]. When it comes to image interactions between point defects, a supercell of 10-15 Å is usually sufficient to keep the interaction energy at a minimum for materials with high dielectric constant (above 40) due to better screening of the charge. For materials with low dielectric constant (under 10) the error in formation energies can be up to several eV for highly charged defects. Several methods for correcting for image interactions exist [57-61]; however, they usually result in different formation energies. Therefore the method to be applied has to be chosen carefully. Another factor that sets a limit to the minimum size of a supercell is the local structural relaxation around a defect. If the supercell is not large enough to accommodate for structural relaxations, then the crystal would be distorted and the energy may be significantly affected. A final effect that can be related to the periodicity of extended functions is the

formation of electric dipole in calculation of *e.g.* asymmetric surfaces and interfaces. Dipoles would result in lowering the formation energy of defects.

In defect calculations where the stoichiometry of the material changes (*e.g.* upon formation of $v_O^{\bullet\bullet}$), the chemical potential is determined by assuming equilibrium with gaseous phases, which involves calculation of total energies of gas molecules. In DFT, small molecules are poorly described, resulting in significant errors in their energy. For instance, O_2 is overbound by 1 eV.[62] To circumvent this, experimental binding energies are used as described in the next sections.

Since DFT is a ground state theory, calculations on high temperature polymorphs, which represent local minima, may be challenging as introduction of symmetry breaking defects may push the structure towards the ground state polymorph, which represents a global minimum. Cubic $SrTiO_3$ represents a shallow minimum in the energy landscape. Upon introduction of $OH_O^{\bullet}$, the O-octahedra may undergo a rotation that results in the ground state tetragonal structure. To avoid that different defects are calculated in different polymorphs (for instance $v_O^{\bullet\bullet}$ does not cause structural transformation), the tetragonal structure of $SrTiO_3$ is used throughout this thesis. Moreover, imaginary frequencies may be encountered when vibrational properties of non-ground state structures are calculated, as is the case in $SrTiO_3$.

Besides the uncertainties and limitations of DFT calculations, a number of simplifications in the thermodynamic modelling have been employed, that may affect the final results. For instance, segregation of defect to the interfacial plane (phase boundary core) between $BaZrO_3$ and $SrTiO_3$, which is caused by structural distortions, has not been considered in the manuscripts. Such distortions are the main reason for defect segregation and space charge formation at grain boundaries. In Manuscript I it was argued that segregation to the phase boundary core may be neglected for epitaxial interfaces between materials exhibiting the same atomic structure and that the defect segregation energies to non-epitaxial interfaces are expected to be similar to that of corresponding grain boundaries. This is confirmed by calculations on $BaZrO_3$/$BaHfO_3$ system where the energy for segregation of $v_O^{\bullet\bullet}$ from $BaZrO_3$ to the (001) epitaxial phase boundary plane is 0.03 eV, and from $BaHfO_3$ to the phase boundary is −0.34 eV. This is in line with $v_O^{\bullet\bullet}$ in $BaZrO_3$ being stabilised by 0.34 eV relative to in $BaHfO_3$. The effect of segregation to the phase boundary core is briefly discussed in Chapter 4 of this thesis.

Within the space charge layer, the concentration of defects may be very high, and in some cases close to unity. This implies that defect-defect interactions may be significant and if not considered, as done here, the calculated concentrations be somewhat overestimated in the first and eventually second plane near then interface, where the concentration of defects exhibits its maximum value (if defects are enriched within the space-charge layer). Moreover, a change in the dielectric constant due to strain, potentially affects the spatial distribution of defects and to some extent the total defect concentration in the space-charge zone. However, the effect strain poses on the defect formation energies in the vicinity of the interface may be more significant than the change in dielectric constant. Whether a defect is stabilised or destabilised near the interface, depends on the formation volume. In general, compressive strain stabilises defects with negative formation volume, and destabilises defects with positive formation volume. The opposite applies for tensile strain. Test calculations on $v_O^{\bullet\bullet}$ ($\Delta V^f = -16\,\text{Å}^3$) in a $3 \times 3 \times 3$ supercell of $BaZrO_3$ show that 5 % compressive strain in the a-b plane further stabilises the $v_O^{\bullet\bullet}$ by 2.0 eV, while a tensile strain of 5 % destabilises it by 1.2 eV. Due to the periodic boundary conditions, it is difficult to include strain effects near interfaces in a realistic way. It should be noted that in reference(s) [40, 41], the formation energy as a function of distance from the interface between $BaZrO_3$ and various metals was found to be fairly constant, except in the first atomic plane in the oxide where the chemistry may differ significantly.

3 Manuscripts/papers

I. **Charge-carrier enrichment at $BaZrO_3/SrTiO_3$ interfaces**, S.W. Saeed, T. Norby and T.S. Bjørheim, *Accepted for publication in The Journal of Physical Chemistry C*

II. **First principles analyses of nanoionic effects at oxide heterointerfaces for electrochemical applications**, S.W. Saeed, *To be submitted*

III. **Surface Segregation Entropy of Protons and Oxygen Vacancies in $BaZrO_3$**, T.S. Bjørheim, M. Arrigoni, S.W. Saeed, E. Kotomin and J. Maier, *Chemistry of Materials*, 2016, **28** (5), 1363-1368

IV. **The role of space-charge at metal/oxide interfaces in protonic ceramic cells**, S.W. Saeed, *To be submitted*

V. **Alkali metals as efficient A-site acceptor dopants in proton conducting $BaZrO_3$**, A. Løken, S.W. Saeed, M.N. Getz, X. Liu and T.S. Bjørheim, *Journal of Materials Chemistry A,* 2016, **4** (23), 9229-9235

Manuscript I

Charge-carrier enrichment at $BaZrO_3/SrTiO_3$ interfaces, S.W. Saeed, T. Norby and T.S. Bjørheim, *Accepted for publication in The Journal of Physical Chemistry C*

Charge-Carrier Enrichment at $BaZrO_3/SrTiO_3$ Interfaces

Sarmad W. Saeed, Truls Norby, and Tor S. Bjørheim*

Centre for Materials Science and Nanotechnology, Department of Chemistry, University of Oslo, FERMiO, Gaustadalléen 21, NO-0349 Oslo, Norway

Keywords: Heterogeneous doping, DFT, $BaZrO_3$, $SrTiO_3$, space charge, nanoionics, proton

Abstract

Heterogeneous doping through nano-structuring has been demonstrated to greatly enhance the transport and mass storage properties of halides and Li-ion conductors by decoupling of charge-compensating species. In this contribution, we explore the potential of heterogeneous doping of ionically conducting oxides through first principles and thermodynamic calculations of a model system consisting of acceptor-doped $SrTiO_3$ and $BaZrO_3$. We show that the two dominating defects, $v_O^{\bullet\bullet}$ and $OH_O^{\bullet}$, are thermodynamically favored in $BaZrO_3$ compared to $SrTiO_3$ by 0.64 and 0.56 eV, respectively – in turn leading to an electrostatic potential barrier as large as 0.64 V (relative to $BaZrO_3$) at 800 K. $v_O^{\bullet\bullet}$ and $OH_O^{\bullet}$, and electron holes as such accumulate on the $BaZrO_3$ side of the interface, leading to a charge-depletion layer in $SrTiO_3$, which thus acts as a heterogeneous acceptor for $BaZrO_3$. These interface effects may as such by used to drastically enhance the charge-carrier concentration of weakly doped ionic systems which in turn may lead to novel nanostructured composite materials with enhanced transport properties or for instance kinetics for oxygen reduction or water splitting.

1. Introduction

Interfacial effects give rise to a variety of interesting phenomena in functional materials, such as enhanced conductivity in ionic solids,[1] ferromagnetism in nonmagnetic materials,[2] metallicity [3] and superconductivity in electrical insulators [4]. Interface effects may become

dominant when the particle size is reduced to the nano-domain, both due to decreased diffusion length and increased interface-to-bulk volume ratio. The importance of such effects can be illustrated by considering one of the simplest types of interfaces; grain boundaries, which represent a structural discontinuity where chemical properties can differ from those in bulk. In many oxygen deficient and commonly acceptor-doped oxides, grain boundary cores are positively charged due to accumulation of oxygen vacancies.[5-8] In order to maintain electroneutrality, adjacent charge-compensating space-charge zones are formed, where the concentration of oxygen vacancies and electron holes is depleted, while that of electrons is enhanced. Consequently, the DC ionic conductivity in polycrystalline oxides is typically orders of magnitude lower than anticipated from bulk conductivity. However, reducing the particle size to a few nm may lead to orders of magnitude increase in the total conductivity due to the grain boundary induced enhancement of the n-type conductivity, as has been observed in Gd-doped CeO_2.[9] In a sense, the grain boundary acts as a structural *donor dopant* leading to deviations from the local electroneutrality imposed by the *homogenous acceptor dopant* (Gd'_{Ce}). In general, any aperiodicity in an otherwise periodic crystalline lattice, such as surfaces, dislocations, and domain boundaries, affects the chemistry of the lattice sites and may lead to effective doping. The same applies to interfaces between different materials, offering more flexibility in tailoring the defect structure of the interface through the physicochemical properties of the two bulk phases, leading to effectively *heterogeneously doped* nanocomposites. In such two-phase systems, heterogeneous doping may result in considerable separation of dopants and charge carriers, consequently eliminating the effect of defect association that otherwise lowers the mobility of charge carriers in *e.g.* H^+, O^{2-} and Li^+ conductors.[10-13]

Heterogeneous doping has been explored for several halide systems, typically sharing a common cation or anion, as in for instance BaF_2/CaF_2, where lattice ions segregate across the interface forming mobile interstitial defects in one phase and vacant lattice sites in the other. The extent of the doping effect is determined by the thermodynamics of heterogeneous defect reactions of common species, which in the case of BaF_2/CaF_2 [14, 15] is

$$F^{\times}_{F,BaF_2} + v^{\times}_{i,CaF_2} \rightleftharpoons v^{\bullet}_{F,BaF_2} + F'_{i,CaF_2}. \quad (1)$$

It is worth noting that we deliberately let the equation break the common principle of restricting defect chemistry and balancing effective charges to only one phase. Here, the shift of defect-originated charge from one side to the other is the central principle. The driving force for defect

segregation is the difference in the chemical potential of charged species in the two phases, which can be divided into the standard chemical potential and an activity dependent component.

Near the interface, the defect concentration can be significant, and yield ionic conductivities orders of magnitude higher than that of the bulk phases as shown for layered structures and composites of BaF_2/CaF_2 [14] and AgCl/AgI [16]. Moreover, the availability of two phases with widely different electronic and defect structure can allow so-called *job-sharing* storage of chemical species. Such storage has been demonstrated in composites of Ru and Li_2O, where excess Li is stored separately as e^- in Ru and interstitial Li^+-ions in Li_2O.[17] The same composite was reported to store H_2 as e^- or H^- in Ru and H^+ in Li_2O.[18] Except for these examples, only a handful of studies exist on job-sharing storage of H-related species and the chemistry of interfaces in systems where at least one of the constituents is a proton conducting oxide. Polfus *et al.* [19] considered the heterogeneous interface between $BaZrO_3$ and MgO, showing that $v_O^{\bullet\bullet}$ and $OH_O^{\bullet}$ are depleted at the $BaZrO_3$ side of the interface due to accumulation of protons at the first plane in MgO. The role of segregation of $v_O^{\bullet\bullet}$ and $OH_O^{\bullet}$ from the bulk-like layers of MgO to $BaZrO_3$ was neglected, despite of both defects exhibiting favorable bulk-to-bulk segregation thermodynamics. In nanocomposites of $CsHSO_4$ and TiO_2, Chan *et al*. [20] reported that space-charge formation due to segregation of H^+ from the solid acid to TiO_2 promoted superionic transition in $CsHSO_4$ at much lower temperatures than in the pure phase. The existence of such space-charge layer was later confirmed in a density functional theory (DFT) study by Haverkate *et al*. [21]. As in the halides, a single chemical species (here H^+) is involved in the heterogeneous defect reaction

$$O_{O,TiO_2}^{\times} + H_{H,CsHSO_4}^{\times} \rightleftharpoons OH_{O,TiO_2}^{\bullet} + v_{H,CsHSO_4}^{\prime}. \qquad (2)$$

Yang *et al*. [22] and Foglietti *et al*. [23] studied the spatially resolved electrical conductivity of the interface between Y-doped $BaZrO_3$ films deposited on $NdGaO_3$, revealing significantly higher conductivities with lower activation energy near misfit dislocations than in bulk-like regions. The authors, however, ascribed this behavior to strain effects, rather than space-charge formation. It is worth to mention that, contrary to the heterointerfaces between $BaZrO_3$ and $SrTiO_3$, the pristine surfaces of these materials have been addressed by numerous computational studies.[24, 25]

In contrast to halides, where the heterogeneous doping effect is determined (and limited) by the segregation of a single species, the complex defect structure of oxides may result in widely different

defect structures at the interface depending on the dominating defect disorder of the two oxides, and their relative chemistries. To the best of our knowledge, no studies exist which are explicitly devoted to heterogeneous doping and its dependence on external factors such as temperature, pressure, etc. in ion conducting oxides. A fundamental understanding of heterogeneous doping in oxides is essential to improve their functional properties beyond what can be achieved through homogeneous doping. In this work, we explore the defect chemistry and potential for job-sharing mechanisms through heterogeneous doping at interfaces in a model system of oxides with complex defect structures; acceptor-doped $SrTiO_3$ and $BaZrO_3$. These materials have been chosen due to the similarity in their defect structure and differences in their chemistry. While $BaZrO_3$ is a state-of-the-art proton conductor where the positive defects are mainly protons at low temperature and oxygen vacancies at high temperature, $SrTiO_3$ is dominated by oxygen vacancies at all practical temperatures and is widely used as a model material in the field of solid-state ionics.

2. Theoretical approaches and methodology

2.1 DFT calculations

All calculations were performed with plane-wave DFT as implemented in the VASP code [26-28] using the GGA-PBE [29] and GGA-PBE+U functionals to describe the exchange-correlation part of the electronic energy in $BaZrO_3$ and $SrTiO_3$, respectively. A U-parameter of 4 eV, applied to the Ti *d*-states according to the approach introduce by Dudarev *et al*. [30], has been determined according to the method presented in reference [31]. However, the results are merely unaffected by the choice of U-parameter; for instance applying a U-parameter of 3 eV, affects the formation energy of defects by less than 50 meV. Projector augmented wave (PAW) potentials [32, 33] having the valence configurations $4s^24p^65s^2$, $5s^25p^66s^2$, $3s^23p^63d^24s^2$, $4s^24p^64d^25s^2$ and $2s^22p^4$ for Sr, Ba, Ti, Zr and O, respectively, were used. The calculations were performed with constant cut-off energy of 500 eV and ionic and electronic convergence criteria of 10^{-4} and 10^{-8} eV, respectively. Calculations on defects were performed with 3×3×3 and 2×2×2 supercells of cubic ($Pm\bar{3}m$) $BaZrO_3$ and tetragonal (I4/mcm) $SrTiO_3$, respectively. The Monkhorst-Pack scheme was used to sample the k-meshes of 2×2×2 and 3×3×2, which were found to yield sufficient convergence (within a few meV) of the total energies. For alignment of the defect energy levels (see details below), supercells of 1×1×11 and 1×1×6, with a corresponding **k**-mesh of 6×6×1, were used. Surface calculations were performed with 11 and 13 layers of $BaZrO_3$ and $SrTiO_3$, respectively.

To calculate the vibrational formation entropies and zero point energies of defects, we performed phonon calculations according to the finite displacement method (with displacements of ±0.01 Å) as implemented in the phonopy code.[34] The phonons were evaluated at the Γ-point, only.

2.2 Bulk thermodynamics

The free energy of defect formation is calculated according to

$$\Delta_f G_{\mathrm{def}} = E_{\mathrm{def}}^{\mathrm{el}} - E_{\mathrm{bulk}}^{\mathrm{el}} + \Delta_{\mathrm{f}} G_{\mathrm{def}}^{\mathrm{vib}} - \sum_i \Delta n_i \mu_i(T,p) + q(\varepsilon_{\mathrm{F}} + \Delta\varepsilon), \tag{3}$$

where $E_{\mathrm{def}}^{\mathrm{el}}$ and $E_{\mathrm{bulk}}^{\mathrm{el}}$ are the total energy of a defect and a perfect supercell, respectively, and $\Delta_f G_{\mathrm{def}}^{\mathrm{vib}}$ is the vibrational free energy contribution to the formation energy. Δn_i is the change in the number of atom type i and μ_i is the corresponding chemical potential. q and ε_{F} are the effective charge of the defect and Fermi level, respectively. $\Delta\varepsilon$ compensates for the shift in band edges due to the jellium background for charged defects, and is calculated from the difference in electrostatic potential of atoms in the defective supercell and the perfect supercell far from the defect. The chemical potentials of gaseous species are obtained from:

$$\mu_i = \mu_i^\circ + E_i^{\mathrm{ZP}} + H_i^\circ(T) - TS_i^\circ(T) + k_{\mathrm{B}}T\ln\left(\frac{p_i}{p^\circ}\right), \tag{4}$$

where μ_i° is the standard chemical potential of gas molecule i. Due to poor description of small molecules in standard DFT, we calculated it from the energy of the separated atoms as obtained from DFT calculations, and experimental binding energies:

$$\mu_i^\circ = \sum E^{atom,DFT} + E^{binding,exp}. \tag{5}$$

E_i^{ZP} is the zero point energy and $H_i^\circ(T)$ and $S_i^\circ(T)$ are the standard enthalpy and entropy, respectively. The first is obtained from experimental vibrational spectroscopy, while the latter two are obtained from thermodynamic tables. The defect concentration is related to the formation Gibbs energy through:

$$\frac{c_i}{c_s - c_i - c_d} = \exp\left(-\frac{\Delta_f G}{k_{\mathrm{B}}T}\right). \tag{6}$$

Here, c_i is the concentration of defect i that forms on lattice site s with concentration c_s. c_d is the concentration of all defects, other than i, that form on lattice site s. Site balance has been accounted for by:

$$\sum_i [i_{\mathrm{O}}] + [\mathrm{O}_{\mathrm{O}}^{\times}] = 3. \tag{7}$$

Here, i runs on all defects that form on the oxygen site.

2.3 Segregation energies

The large lattice mismatch between $SrTiO_3$ and $BaZrO_3$ results in a heavily strained interface between these two materials causing DFT calculations to fail in describing the present system in the sense that a supercell containing both materials would have tilting of oxygen octahedra and consequently incorrect segregation energies. To avoid computational artefacts, we calculate the standard segregation energies of defects, *i.e.* the bulk-to-bulk segregation energies. This is done by calculating the defect formation energies with respect to the valence band maximum (VBM) after aligning it with respect to the vacuum level, which represents a global reference. Thus, the formation energies used to compare the stability and calculate the segregation energy of a defect is

$$\Delta_f G_{\mathrm{def}} = E_{\mathrm{def}}^{\mathrm{el}} - E_{\mathrm{bulk}}^{\mathrm{el}} + \Delta_{\mathrm{f}} G_{\mathrm{def}}^{\mathrm{vib}} - \sum_i \Delta n_i \mu_i(T,p) + q\left(\varepsilon_{\mathrm{VBM,aligned}} + \Delta\varepsilon\right). \tag{8}$$

The main difference between this equation and Eq. (3), is the replacement of ε_{F} with $\varepsilon_{\mathrm{VBM,aligned}}$. The calculations can also be performed by including the valence band offset, $\Delta\varepsilon_{\mathrm{VBM}}$, with respect to one of the two materials, for instance $BaZrO_3$ (as we have done in this work) in Eq. (3), which becomes

$$\Delta_f G_{\mathrm{def}} = E_{\mathrm{def}}^{\mathrm{el}} - E_{\mathrm{bulk}}^{\mathrm{el}} + \Delta_{\mathrm{f}} G_{\mathrm{def}}^{\mathrm{vib}} - \sum_i \Delta n_i \mu_i(T,p) + q(\varepsilon_{\mathrm{F}} + \Delta\varepsilon + \Delta\varepsilon_{\mathrm{VBM}}). \tag{9}$$

The standard defect segregation energy is, as such, given by

$$\mu_{i,\mathrm{seg}}^{\circ} = \mu_i^{\circ} - \mu_i^{\circ\prime} = \Delta_f G_{\mathrm{def}} - \Delta_f G'_{\mathrm{def}}, \tag{10}$$

where the prime denotes a different phase.

Fig. 1 shows a schematic representation of the alignment of the VBM in $BaZrO_3$ and the VBM offset between $BaZrO_3$ and $SrTiO_3$. The latter is given by the difference in the ionization potential, IP, between the two materials,

$$\Delta\varepsilon_{\mathrm{VBM}} = IP - IP', \tag{11}$$

which for the current system is 0.40 V (wrt. $BaZrO_3$) as shown in **Fig. 1a**. To determine the *IP*, DFT calculations on slabs of $BaZrO_3$ and $SrTiO_3$ are necessary. Although the *IP* can be obtained from a single DFT calculation, the presence of band bending and electronic states at the surface makes it challenging to determine the actual VBM position in the slab calculation. Therefore, we use the VBM from a bulk calculation such that

$$IP = U_{vac} - \varepsilon_{VBM} = U_{vac.slab} + U_{diff} - \varepsilon_{VBM}, \tag{12}$$

where U_{vac} is the potential of vacuum with respect to bulk and $U_{diff} = U_{bulk} - U_{slab}$, is the difference in the average electrostatic potential of the bulk region in the slab and bulk calculations, as illustrated in **Fig. 1b**. The actual potentials are shown in **Fig. 2**.

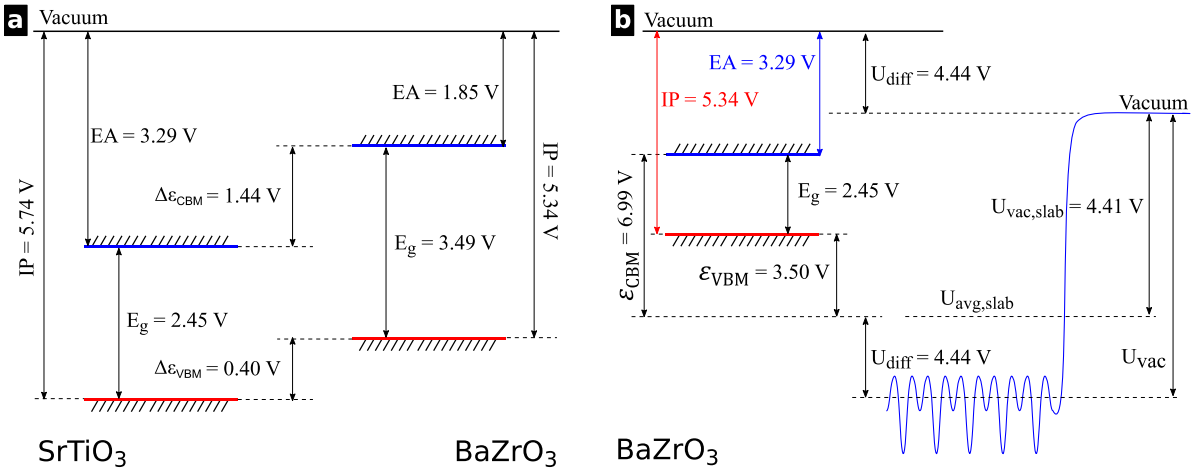

Fig. 1. A schematic representation of the alignment of (a) VBM between $BaZrO_3$ and $SrTiO_3$ and (b) band structure of $BaZrO_3$ wrt. vacuum level to determine the ionization potential, *IP*. Figure (b) is not at scale.

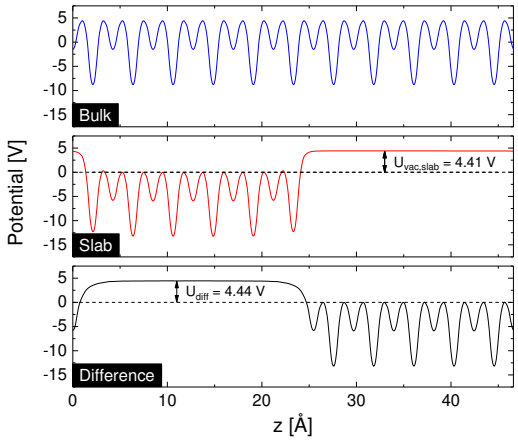

Fig. 2. The average electrostatic potential in bulk and a slab of $BaZrO_3$ and their difference.

Our method for evaluation of segregation energies is computationally feasible as it avoids the explicit treatment of the interface system, thus allowing high throughput screening. Neglection of segregation to the interfacial plane itself can for this system be justified by the structural and chemical similarity of the two phases, and we expect the formation energy of defects at epitaxial interfaces to fall within the range of the two bulk phases (as opposed to in *e.g.* bulk/grain boundary or bulk/surface system). For more chemically and structurally different interfaces, such as heterointerfaces with inherent charge imbalance (*e.g.* $A^{2+}B^{4+}O_3/A^{3+}B^{3+}O_3$), defect segregation to the interface plane(s) should be explicitly included. Furthermore, it should be mentioned that although the GGA-PBE(+U) exchange correlation functional significantly underestimates the bandgap of perovskite oxides compared to hybrid functionals,[35, 36] the defect segregation energies are not affected since the alignment of band edges we perform yields the same relative band edge positions as in a supercell containing both materials.

2.4 Space-charge thermodynamics

We apply the widely adopted abrupt model to describe the interface, *i.e.* we assume that the defect formation energies and the atomic structure in the space-charge region is the same as in the bulk materials and that these properties change abruptly across the interface plane. As such, the electrochemical potential of species i, $\tilde{\mu}_i$, within one material can be written as

$$\tilde{\mu}_i = \mu_i^\circ + k_B T \ln\left(\frac{c_i(x)}{c_s - c_i(x)}\right) + q_i\varphi(x), \tag{13}$$

where $\varphi(x)$ is the electrostatic potential at a distance x from the interface (note that $x = \infty$ corresponds to bulk, where $\varphi = 0$). At equilibrium, the electrochemical potential becomes constant throughout the interface, such that:

$$\mu_i^\circ + k_B T \ln\left(\frac{c_i(x)}{c_s - c_d(x) - c_i(x)}\right) + q_i\varphi(x) = \mu_i^{\circ\prime} + k_B T \ln\left(\frac{{c'}_i(x')}{c_s' - c_d'(x') - {c'}_i(x')}\right) + q_i\varphi(x'), \tag{14}$$

where the prime denotes that the defect resides in the adjacent phase or at a different position within the same phase (then $\mu_i^{\circ\prime} = \mu_i^\circ$). Rearranging Eq. (14) and setting $x' = +\infty$ gives the concentration of defects as a function of bulk concentrations and the electrostatic potential with respect to that in bulk, $\Delta\varphi(x) = \varphi(x) - \varphi_{bulk}$:

$$c_i(x) = \frac{\big(c_s - c_d(x)\big)c_{i,bulk}' \exp\left(\frac{\mu_i^{\circ\prime} - \mu_i^\circ}{k_B T} + \frac{q_i\big(\varphi(x') - \varphi(x)\big)}{k_B T}\right)}{c_s' - c_{i,bulk}' - c_{d,bulk}' - c_{i,bulk}' \exp\left(\frac{\mu_i^{\circ\prime} - \mu_i^\circ}{k_B T} + \frac{q_i\big(\varphi(x') - \varphi(x)\big)}{k_B T}\right)}, \tag{15}$$

where $c_s' = c_s$ when x is in the reference material. If the electrostatic potential at the interface ($\phi = \Delta\varphi(x = 0)$) is known, then the potential as a function of distance can be determined from Poisson's equation,

$$\frac{\mathrm{d}^2}{\mathrm{d}x^2}\Delta\varphi(x) = -\frac{\rho(x)}{\epsilon}, \tag{16}$$

which relates the charge density, $\rho(x)$, to the electrostatic potential. ϵ is the dielectric constant. The charge density is given by

$$\rho(x) = \sum\nolimits_i e q_i c_i(x). \tag{17}$$

Although ϕ and ϕ' are unknown, the total electrostatic potential difference across the interface, Φ, is known. Rearranging Eq. (14) and setting $x = -\infty$ and $x' = +\infty$ give Φ in terms of the segregation energies, $\mu_{i,seg}^\circ = \mu_i^{\circ\prime} - \mu_i^\circ$, and bulk concentrations of defects:

$$\Phi = \phi - \phi' = \frac{1}{q_i}\left[\big(\mu_{i,seg}^\circ\big) + k_B T \ln\left(\frac{c_{i,bulk}'\big[c_s - c_{i,bulk}\big]}{c_{i,bulk}\big[c_s' - c_{i,bulk}'\big]}\right)\right]. \tag{18}$$

Solving this set of equations numerically with appropriate boundary conditions gives the spatial electrostatic potential and concentration profiles.

The required boundary conditions are constant electrostatic potential in bulk,

$$\frac{d}{dx}\varphi(x) = 0\Big|_{x=\infty}, \tag{19}$$

and, in absence of charge accumulation at the interface plane, constant dielectric function at the interface,

$$\varepsilon\frac{d}{dx}\varphi(x) = -\varepsilon'\frac{d}{dx'}\varphi(x')\Big|_{x=x'=0}, \tag{20}$$

which ensures charge neutrality in the system.

3. Results and discussion

Two defects are included in this work; oxygen vacancies, $v_O^{\bullet\bullet}$, and protons, $OH_O^{\bullet}$. Although electron holes dominate the electrical conductivity in $BaZrO_3$ and $SrTiO_3$ at high temperatures and oxygen partial pressures, they have been omitted due to their low concentration. The relative concentrations of $v_O^{\bullet\bullet}$ and $OH_O^{\bullet}$ in $SrTiO_3$ and $BaZrO_3$ are determined by the hydration enthalpies, which are calculated to −0.84 and −0.39 eV, respectively, in line with previous computational and experimental works.[37-39] Including vibrational effects (*i.e.,* ZPEs and entropies) for the defects and gaseous species increases the enthalpies somewhat to −0.81 and −0.29 eV. Although these differ slightly from the experimental enthalpies, it will not affect our analysis significantly. Thus, $BaZrO_3$ will be predominated by protons below 600 K, above which the concentration of $v_O^{\bullet\bullet}$ becomes significant, as shown in **Fig. 3b**. On the other hand, $SrTiO_3$ starts to lose $OH_O^{\bullet}$ already at 150 K, and becomes completely predominated by oxygen vacancies above 200 K, **Fig. 3a**. $SrTiO_3$ will as such never be dominated by protons under realistic conditions. However, it is still of interest as a model material since it exhibits a transition from a $OH_O^{\bullet}$ to a $v_O^{\bullet\bullet}$ dominated defect structure under conditions where the counter-phase (here $BaZrO_3$) remains dominated by $OH_O^{\bullet}$, allowing evaluation of the implications of hydration/dehydration of both phases on the heterogeneous doping effect.

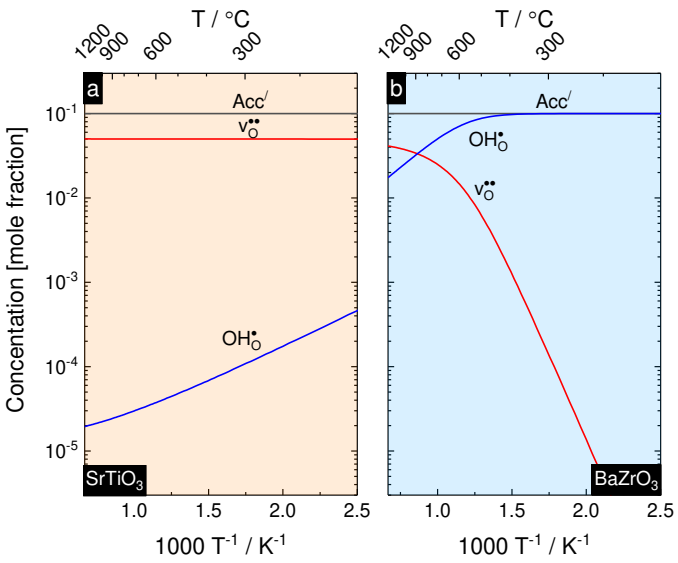

Fig. 3. Defect concentrations in bulk acceptor doped (10 mole %) $SrTiO_3$ (a) and $BaZrO_3$ (b) as a function of inverse temperature in wet (p_{H_2O} = 0.03 atm) oxygen.

In the defect chemistry of interfaces, an essential parameter is the defect segregation enthalpy, ΔH_{seg}, which is a measure of the relative stability of defects in the two phases. ΔH_{seg} is usually calculated from the defect formation energies in bulk-like layers of a supercell containing slabs of two materials. In the $BaZrO_3/SrTiO_3$ system, which exhibits relatively large lattice mismatch (~7 %),[40] DFT fails in predicting the correct interface structure, thus resulting in unphysical structural distortion, and consequently inaccurate defect energetics. To circumvent this artefact, we, initially, calculate and use standard segregation enthalpies, *i.e.* bulk-to-bulk segregation energies. The role of strain will be addressed explicitly towards the end of this section. Furthermore, defect segregation to the interface plane is negligible compared to the bulk-to-bulk segregation energy in epitaxial thin films of materials having the same structure, and is therefore not included. The latter has been confirmed by calculations on other, similar perovskite interfaces.

According to our model, segregation of $v_O^{\bullet\bullet}$ from $SrTiO_3$ to $BaZrO_3$ according to

$$v_{O,SrTiO_3}^{\bullet\bullet} + O_{O,BaZrO_3}^{\times} \rightleftharpoons O_{O,SrTiO_3}^{\times} + v_{O,BaZrO_3}^{\bullet\bullet}, \qquad (21)$$

exhibits a strongly negative enthalpy of −0.64 at 0 K, which may arise from the more basic character of $BaZrO_3$ than $SrTiO_3$. The segregation enthalpy of $OH_O^{\bullet}$ to $BaZrO_3$, on the other hand,

is somewhat weaker, −0.56 eV. The segregation energies of the two defects are coupled through the bulk hydration enthalpies, and can be expressed as

$$\Delta H^{\mathrm{seg}}_{\mathrm{OH}^{\bullet}_{\mathrm{O}}} = \frac{\Delta H^{\mathrm{seg}}_{\mathrm{v}^{\bullet\bullet}_{\mathrm{O}}} + \Delta\left(\Delta H_{\mathrm{hydr}}\right)}{2}. \tag{22}$$

This equation shows that $\Delta H^{\mathrm{seg}}_{\mathrm{OH}^{\bullet}}$ can even be positive if materials with a large enough difference in ΔH_{hydr} are chosen. Moreover, if one segregation enthalpy is known, then segregation enthalpies of all other defects that can be related through a defect reaction can be determined from, for instance experimental, reaction enthalpies.

The electrostatic potential, Φ, that arises from defect segregation across the interface is directly coupled to the segregation enthalpies (Eq. (18)). In the limit where both materials are dominated by $\mathrm{v}^{\bullet\bullet}_{\mathrm{O}}$ or $\mathrm{OH}^{\bullet}_{\mathrm{O}}$, Φ is −0.32 or −0.56 V, respectively, at 0 K. The temperature dependence of Φ is shown in **Fig. 4**. The red curve shows the electrostatic potential that arises from $\mathrm{v}^{\bullet\bullet}_{\mathrm{O}}$ segregation, *i.e.* in the limit where reaction Eq. (21) dominates. In that limit, Φ exhibits a strong, positive temperature dependence and eventually exceeds 0.0 V at 1550 K. This curve is valid under dry conditions and/or high temperature. Under such conditions, the temperature dependence of Φ is given by the vibrational segregation entropy, under the assumption that the parent materials have the same doping level such that the configurational term in Eq. (18) cancels. For the current system, the segregation entropies are −40 J/mol K for $\mathrm{v}^{\bullet\bullet}_{\mathrm{O}}$ and 10 J/mol K for $\mathrm{OH}^{\bullet}_{\mathrm{O}}$. Interestingly, the negative segregation entropy of $\mathrm{v}^{\bullet\bullet}_{\mathrm{O}}$ suppresses defect segregation to $BaZrO_3$, hence the positive temperature dependence and inversion of Φ at high temperature, which eventually causes defects to segregate to $SrTiO_3$. At lower temperatures, where $\mathrm{OH}^{\bullet}_{\mathrm{O}}$ is the dominating defect, Φ is increasingly negative with increasing temperature as a result of the positive segregation entropy of $\mathrm{OH}^{\bullet}_{\mathrm{O}}$, which contributes to increased defect segregation to $BaZrO_3$. Thus, this example illustrates how materials can be chosen in order to tune the defect chemical properties of interfaces based on knowledge of their thermodynamics.

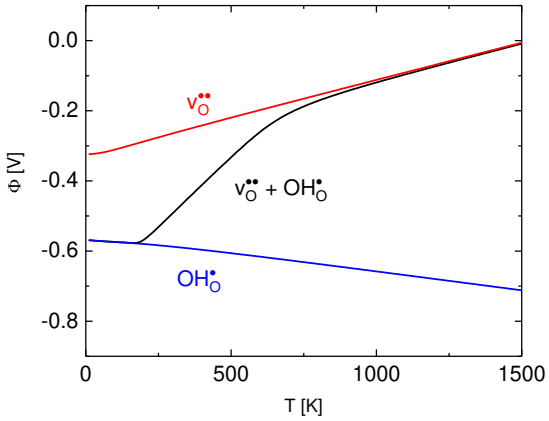

Fig. 4. The electrostatic potential across the interface between $SrTiO_3$ and $BaZrO_3$ as a function of temperature. The red and blue curves show the potential if both materials contain only $v_O^{\bullet\bullet}$ or $OH_O^{\bullet}$, respectively. The black curve shows the development of the potential when both defects are included.

The defect structure is rarely dominated by a single defect, and in $SrTiO_3$ and $BaZrO_3$, the presence of $v_O^{\bullet\bullet}$ and $OH_O^{\bullet}$ results in three distinct defect situations at low, intermediate and high temperatures. At high and low temperatures, the materials are dominated by $v_O^{\bullet\bullet}$ and $OH_O^{\bullet}$, respectively, and the electrostatic potential difference between the two bulk phases is described according to the discussion in the previous paragraph. At intermediate temperatures, $SrTiO_3$ is dominated by $v_O^{\bullet\bullet}$, with $OH_O^{\bullet}$ as minority defect, while $BaZrO_3$ is dominated by $OH_O^{\bullet}$, with $v_O^{\bullet\bullet}$ as minority defect. In this region, both defects contribute to Φ through the second term on the right hand side of Eq. (18), which becomes substantial due to the large difference in the chemical activity of defects in the two materials. The black curve in **Fig. 4** shows the potential when both $v_O^{\bullet\bullet}$ and $OH_O^{\bullet}$ are included in the calculation. In the transition region, the potential takes on values in between the two extremes, where either $v_O^{\bullet\bullet}$ or $OH_O^{\bullet}$ dominates. The dependence of Φ on the defect concentration in the constituting materials reflects that it is strongly affected by changes in external parameters such as doping type/level and atmospheric conditions. For instance, reducing p_{H_2O} at constant temperature would result in shifting the transition region in **Fig. 4** to the left and consequently increasing the potential, which would affect the defect chemistry and conductivity as discussed below.

In all three limiting cases, $v_O^{\bullet\bullet}$ and $OH_O^{\bullet}$ accumulate on the $BaZrO_3$ side of the interface due to their high chemical potential in $SrTiO_3$. Thus, $BaZrO_3$ acts as a donor phase, while $SrTiO_3$, effectively, acts as an acceptor, in conjunction with each other. The situation is the opposite of that at a grain

boundary in $BaZrO_3$, which acts as a structural donor dopant due to the positively charged core. Consequently, with respect to the bulk materials, the electrostatic potential arising from defect segregation becomes negative in $BaZrO_3$ and positive in $SrTiO_3$. Examples of the concentration and electrostatic potential profiles at 150, 600 and 1200 K in wet O_2 are shown in **Fig. 5**. These profiles have been calculated according to the Mott-Schottky model, where cations are assumed to be immobile, which represents the defect situation in samples made at low temperature, for instance by PLD. Towards the interface, the concentration of $v_O^{\bullet\bullet}$ and $OH_O^{\bullet}$ increase in $BaZrO_3$ and significantly decrease in $SrTiO_3$. In both materials, the enrichment/depletion effect is stronger for $v_O^{\bullet\bullet}$ than for $OH_O^{\bullet}$, due to the charge difference of the two species. Except for the first 1-3 nm from the boundary, which corresponds to the extent of the space-charge layer, the defect concentrations and other parameters are expected to be as in the bulk phases. For $SrTiO_3$, the space-charge layer is wider compared to $BaZrO_3$, which stems from its higher dielectric constant and the limited number of defects that can be depleted. In $BaZrO_3$, availability of many regular lattice sites where defects can form results in a narrower space-charge layer. The resulting space-charge layer width and concentration profiles in $SrTiO_3$ at 600 K are very similar to those calculated for grain boundaries [41]. As **Fig. 5** shows, the space-charge layer width decreases with increasing temperature, at the same time the concentration enrichment (depletion) is suppressed. This is a consequence of the thermal energy that balances the segregation enthalpy and the increase of Φ (*i.e.* smaller absolute value).

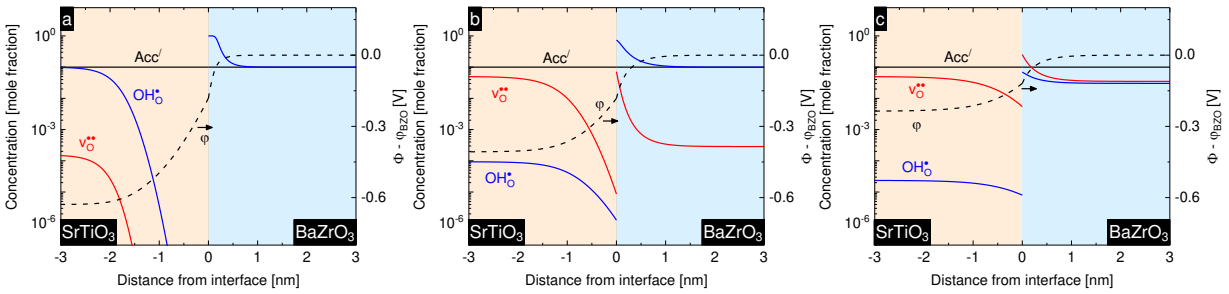

Fig. 5. The concentration profiles of defects as a function of distance from the interface at 150 (a), 600 (b) and 1200 K in wet (p_{H_2O} = 0.03 atm) oxygen.

Fig. 5b shows an important aspect of the difference in the defect structure of $BaZrO_3$ and $SrTiO_3$ that is encountered at intermediate temperatures where mass balance cannot be achieved within the isolated composite system as $SrTiO_3$ and $BaZrO_3$ are dominated by $v_O^{\bullet\bullet}$ and $OH_O^{\bullet}$, respectively.

Under such conditions, depletion of $v_O^{\bullet\bullet}$ in $SrTiO_3$ involves incorporation of O^{2-} that cannot be provided by $BaZrO_3$, at the same time $SrTiO_3$ cannot provide the $OH_O^{\bullet}$ that are enriched in $BaZrO_3$. Consequently, the surroundings are involved through a heterogeneous reaction where a job-sharing process results in incorporation of water when the two materials come into contact with each other. The same applies upon a change in Φ, for instance due to a change in temperature, in a system where the materials already are in contact with each other. In that respect, the process corresponds to reversible job-sharing storage of H_2O upon temperature cycling. Job-sharing mechanisms can as such be utilized to enhance the proton concentration through heterogeneous doping and thereby the conductivity. This can be achieved by choosing materials in which segregation of defects to, for instance, $BaZrO_3$ has negative enthalpy and strongly positive entropy such that in addition to enrichment of protons, dehydration of nanocomposites of $BaZrO_3$ is limited at high temperature. Even though $BaZrO_3$ still dehydrates with increasing temperature, increasingly negative Φ would result in more vacancies in the space-charge layer and therefore shift the hydration reaction to the right such that the overall proton concentration may become constant or even increase with increasing temperature.

Fig. 6 compares the defect concentration and electrostatic potential profiles calculated according to the Mott-Schottky and Gouy-Chapman models. The latter represents the situation in samples quenched from high temperatures. Therefore, the dopant concentration profile has been fixed to that at 1200 K – under which the concentration of dopant can be considered as frozen-in. The accumulation of dopants in $SrTiO_3$ results in enhanced concentration of $v_O^{\bullet\bullet}$ and $OH_O^{\bullet}$ and reduced space-charge layer width, compared to the Mott-Schottky model. This is in line with experimental observations near grain boundaries of $SrTiO_3$ and $BaZrO_3$, where dopant accumulation has been confirmed by high-resolution microscopy/spectroscopy methods [42, 43]. Similarly, the depletion of dopant is supposed to reduce the defect enrichment in $BaZrO_3$; however, that is not the case – in fact, the Gouy-Chapman model predicts that the concentration of $OH_O^{\bullet}$ in the space-charge layer is higher than predicted by the Mott-Schottky model, 0.44 vs. 0.41 C/m^2. This stems from the accumulation of acceptors in $SrTiO_3$, which is three times as high as the dopant depletion in $BaZrO_3$, and thus more than cancels its effect. Therefore, compared to grain boundaries and surfaces, equilibration of dopants at a heterogeneous interface has less influence on the concentration of defects in the space-charge zone.

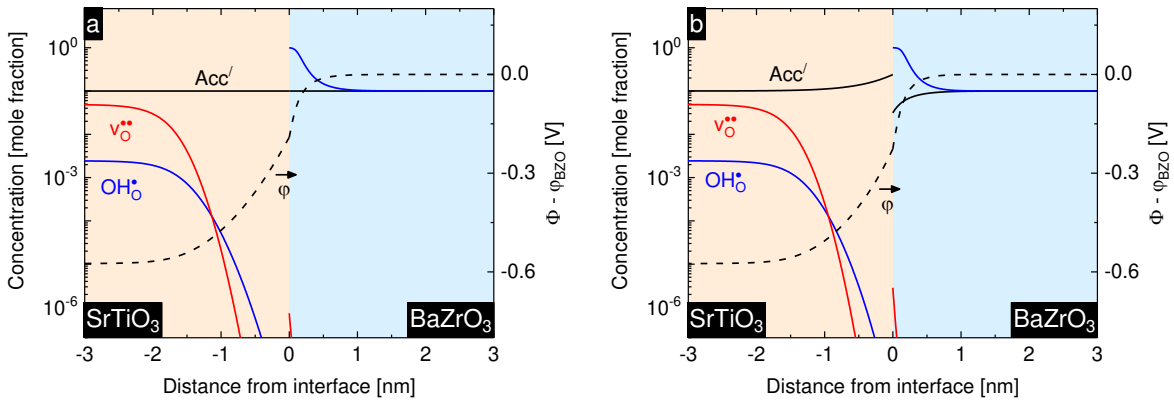

Fig. 6. The concentration profiles of defects as a function of distance from the interface at 300 K in wet ($p_{H_2O} = 0.03$ atm) oxygen, as calculated according to the Mott-Schottky (a) and Gouy-Chapman model (b).

So far the effect of strain on the physicochemical properties of the interface has not been considered. Strain may, however, affect both the dielectric constant and the formation energy of defects in the near-interface region of both materials. While changes in the dielectric constant have minor effects on the spatial distribution of defects in the near-interface space-charge zone, the integrated concentration practically remains unaffected. In contrast, the change in the defect formation energy may be more important. In general, compressive strain stabilizes defects that exhibit negative formation volume – such as $v_O^{\bullet\bullet}$ and $OH_O^{\bullet}$, where the formation volumes are –18 and –4 Å^3, respectively [44] – while tensile strain stabilizes defects that exhibit positive formation volume. In addition, the shape of a defect may also be instrumental. For an epitaxial (0 0 1) terminated $BaZrO_3/SrTiO_3$ interface, the average strain is 3 %. Calculations on bulk $BaZrO_3$ and $SrTiO_3$ subjected to 3 % compressive and tensile strain in the a-b plane changes the formation energy of $v_O^{\bullet\bullet}$ by –0.42 and 0.19 eV, respectively. For $OH_O^{\bullet}$, the corresponding changes are 0.27 and 0.05 eV, respectively. Although these numbers are significant, they represent an upper limit as formation of dislocations may moderate the strain to some extent. The change in formation energy (and defect affinity) as a function of strain in $BaZrO_3$ and $SrTiO_3$ are presented in **Fig. 7**. For $OH_O^{\bullet}$ in $BaZrO_3$, the effect of strain on the formation energy is opposite to that of $v_O^{\bullet\bullet}$ despite its negative formation volume. This may be a result of the shape of the two defects; while $OH_O^{\bullet}$ gives an anisotropic distortion of the lattice, $v_O^{\bullet\bullet}$ gives tetragonal distortion. For the current interface with

average compressive and tensile strain of 3 % in $BaZrO_3$ and $SrTiO_3$, the segregation energies become –1.71 and –0.60 eV for $v_O^{\bullet\bullet}$ and $OH_O^{\bullet}$, respectively.

Fig. 8 shows the electrostatic potential and defect concentration profiles across the interface by accounting for strain. Indeed, due to larger electrostatic potential difference, more defects are enriched (depleted) in the two materials, and the spatial extent of the space-charge layer is increased. At 600 and 1200 K, the concentration of $v_O^{\bullet\bullet}$ in the space-charge region of $BaZrO_3$ becomes significant, approaching unity. Likewise, the concentration of $OH_O^{\bullet}$ increases towards the interface, before it starts to flatten out and eventually decrease close to the phase boundary. This behavior stems from the competition between $v_O^{\bullet\bullet}$ and $OH_O^{\bullet}$, both of which form on the O-sublattice.

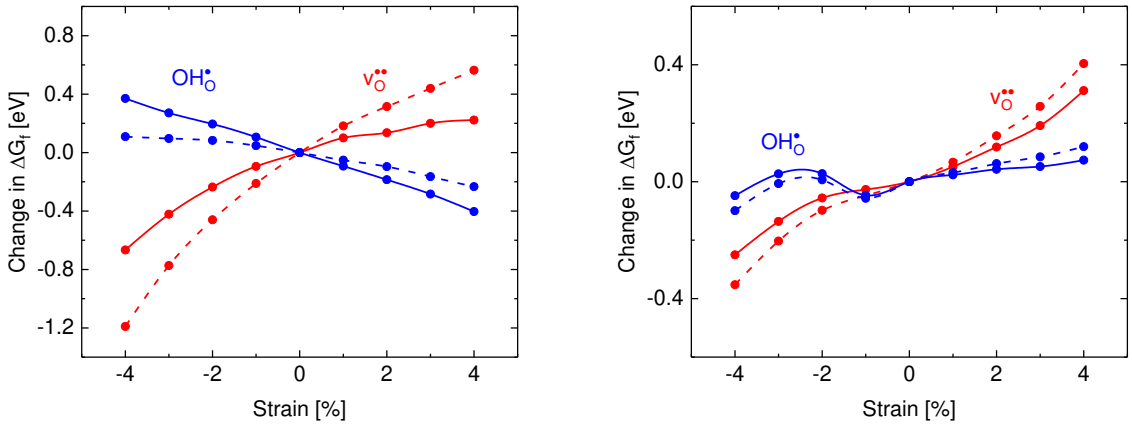

Fig. 7. Change in the formation energy of defects (relative to the unstrained material) as a function of strain in $BaZrO_3$ (a) and $SrTiO_3$ (b). The solid lines show the change in formation energy – the dashed lines also include alignment with respect to the vacuum level (*i.e.* represent the change in defect affinity). Notice the difference in scale.

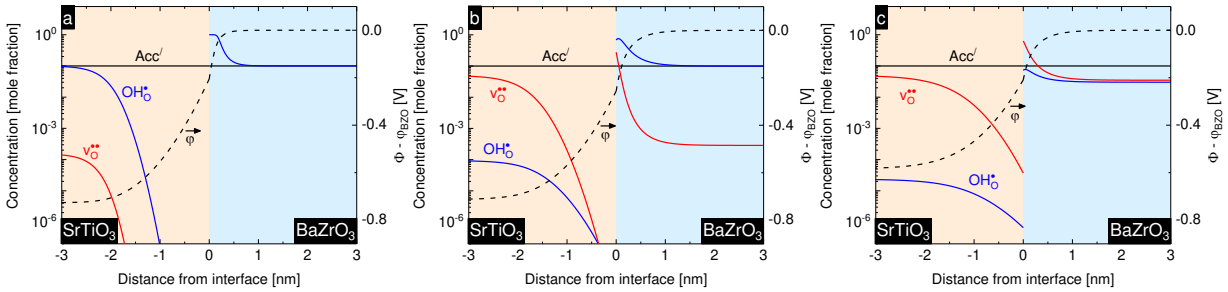

Fig. 8. The concentration profiles of defects as a function of distance from the interface at 150 (a), 600 (b) and 1200 K in wet (p_{H_2O} = 0.03 atm) oxygen.

These results show that the total concentration of protons at heterointerfaces and in nanocomposites can far exceed those of the parent bulk phases which in turn can enhance the in-plane proton transport properties of for instance multi-layered nanostructured films. This also demonstrate that the macroscopic properties of multilayered thin films differ significantly from those of the bulk materials. For instance, the electrical conductivity of $SrTiO_3$/$BaZrO_3$ films is expected to be dominated by the high electron hole conductivity of $SrTiO_3$, which in the bulk material is proportional to $p_{O_2}^{1/4}$ and has no dependence on p_{H_2O}. However, in a nanostructured, multilayered thin film with a proton conductor, where the volumetric concentration of interfaces is significant, a change in p_{H_2O} brings about a change in Φ, as shown in **Fig. 4**, which in turn affects the hole concentration in the space-charge layer, and consequently, the macroscopic conductivity.

4. Conclusions

First principles calculations reveal that $SrTiO_3$/$BaZrO_3$ nanostructures may lead to heterogeneous doping that strongly affects the defect chemical and transport properties of the two materials. Both $v_O^{\bullet\bullet}$ and $OH_O^{\bullet}$ exhibit negative segregation enthalpies of –0.64 and –0.56 eV, respectively, from $SrTiO_3$ to $BaZrO_3$, resulting in depletion of defects in $SrTiO_3$ and enrichment in $BaZrO_3$. Effectively, this corresponds to acceptor doping of $BaZrO_3$ and donor doping of $SrTiO_3$. At intermediate temperatures, reversible incorporation of H_2O occurs upon change in the electrostatic potential, which exhibits a strong temperature dependence that is determined by the segregation entropy of the two defects. Such job-sharing mass exchange may allow storage of H_2 in nanocomposites of proton conductors and electron conductors, such as metals or for instance donor-doped $SrTiO_3$. Furthermore, the total concentration of $OH_O^{\bullet}$ in nanostructured heterostructures and composites of $BaZrO_3$ and $SrTiO_3$ is significantly higher than in the bulk materials, suggesting that their ionic conductivity will be higher than in the individual phases since protons exhibit higher diffusivity than oxygen vacancies. Finally, strain may substantially affect the segregation energies of defects and may as such, together with homogeneous doping, be used to tailor the properties of interfaces. In conclusion, our results demonstrate how appropriate choice of materials with different physiochemical properties may enable heterogeneous doping in nanocomposites, yielding materials that are no longer subjected to the local electroneutrality constraints of the bulk materials.

Corresponding author

*E-mail: torsb@kjemi.uio.no.

Acknowledgements

The Norwegian Metacenter for Computational Science (NOTUR) is acknowledged for providing the computational resources under Project NN4604k.

References

1. Liang, C.C., *Conduction Characteristics of the Lithium Iodide-Aluminum Oxide Solid Electrolytes.* Journal of The Electrochemical Society, 1973. **120**(10): p. 1289-1292.
2. Brinkman, A., et al., *Magnetic effects at the interface between non-magnetic oxides.* Nature Materials, 2007. **6**: p. 493.
3. Ohtomo, A. and H.Y. Hwang, *A high-mobility electron gas at the $LaAlO_3/SrTiO_3$ heterointerface.* Nature, 2004. **427**: p. 423.
4. Reyren, N., et al., *Superconducting Interfaces Between Insulating Oxides.* Science, 2007. **317**(5842): p. 1196-1199.
5. Guo, X., et al., *Role of space charge in the grain boundary blocking effect in doped zirconia.* Solid State Ionics, 2002. **154-155**: p. 555-561.
6. Tschöpe, A., E. Sommer, and R. Birringer, *Grain size-dependent electrical conductivity of polycrystalline cerium oxide: I. Experiments.* Solid State Ionics, 2001. **139**(3): p. 255-265.
7. Denk, I., J. Claus, and J. Maier, *Electrochemical Investigations of $SrTiO_3$ Boundaries.* Journal of The Electrochemical Society, 1997. **144**(10): p. 3526-3536.
8. Kjølseth, C., et al., *Space–charge theory applied to the grain boundary impedance of proton conducting $BaZr_{0.9}Y_{0.1}O_{3-\delta}$.* Solid State Ionics, 2010. **181**(5): p. 268-275.
9. Chiang, Y.M., et al., *Defect and transport properties of nanocrystalline CeO_{2-x}.* Applied Physics Letters, 1996. **69**(2): p. 185-187.
10. Yamazaki, Y., et al., *Proton Trapping in yttrium-doped barium zirconate.* Nat. Mater., 2013. **12**: p. 647.
11. Björketun, M.E., P.G. Sundell, and G. Wahnström, *Effect of acceptor dopants on the proton mobility in $BaZrO_3$: A density functional investigation.* Physical Review B, 2007. **76**(5): p. 054307.
12. Jung, G.-B., T.-J. Huang, and C.-L. Chang, *Effect of temperature and dopant concentration on the conductivity of samaria-doped ceria electrolyte.* Journal of Solid State Electrochemistry, 2002. **6**(4): p. 225-230.
13. Bruce, P.G. and A.R. West, *Ion trapping and its effect on the conductivity of LISICON and other solid electrolytes.* Journal of Solid State Chemistry, 1984. **53**(3): p. 430-434.
14. Sata, N., et al., *Mesoscopic fast ion conduction in nanometre-scale planar heterostructures.* Nature, 2000. **408**: p. 946.
15. Maier, J., *Defect chemistry and ion transport in nanostructured materials: Part II. Aspects of nanoionics.* Solid State Ionics, 2003. **157**(1): p. 327-334.

16. Lauer, U. and J. Maier, *Conductivity enhancement and microstructure in AgCl/AgI composites.* Solid State Ionics, 1992. **51**(3): p. 209-213.
17. Balaya, P., et al., *Fully Reversible Homogeneous and Heterogeneous Li Storage in RuO_2 with High Capacity.* Advanced Functional Materials, 2003. **13**(8): p. 621-625.
18. Fu, L., et al., *"Job-Sharing" Storage of Hydrogen in Ru/Li_2O Nanocomposites.* Nano Letters, 2015. **15**(6): p. 4170-4175.
19. Polfus, J.M., T. Norby, and R. Bredesen, *Proton segregation and space-charge at the $BaZrO_3$ (0 0 1)/MgO (0 0 1) heterointerface.* Solid State Ionics, 2016. **297**: p. 77-81.
20. Chan, W.K., et al., *Direct View on Nanoionic Proton Mobility.* Advanced Functional Materials, 2011. **21**(8): p. 1364-1374.
21. Haverkate, L.A., W.K. Chan, and F.M. Mulder, *Large space-charge effects in a nanostructured proton conductor.* Advanced Functional Materials, 2010. **20**(23): p. 4107-4116.
22. Yang, N., et al., *Defective Interfaces in Yttrium-Doped Barium Zirconate Films and Consequences on Proton Conduction.* Nano Letters, 2015. **15**(4): p. 2343-2349.
23. Foglietti, V., et al., *Heavily strained $BaZr_{0.8}Y_{0.2}O_{3-x}$ interfaces with enhanced transport properties.* Appl. Phys. Lett., 2014. **104**: p. 081612.
24. Eglitis, R.I., *First-principles calculations of $BaZrO_3$ (001) and (011) surfaces.* Journal of Physics: Condensed Matter, 2007. **19**(35): p. 356004.
25. Eglitis, R.I. and D. Vanderbilt, *First-principles calculations of atomic and electronic structure of $SrTiO_3$ (001) and (011) surfaces.* Physical Review B, 2008. **77**(19): p. 195408.
26. Kresse, G. and J. Hafner, *Ab initio molecular-dynamics simulation of the liquid-metal--amorphous-semiconductor transition in germanium.* Physical Review B, 1994. **49**(20): p. 14251-14269.
27. Kresse, G. and J. Furthmüller, *Efficiency of ab-initio total energy calculations for metals and semiconductors using a plane-wave basis set.* Computational Materials Science, 1996. **6**(1): p. 15-50.
28. Kresse, G. and J. Furthmüller, *Efficient iterative schemes for ab initio total-energy calculations using a plane-wave basis set.* Physical Review B, 1996. **54**(16): p. 11169-11186.
29. Perdew, J.P., K. Burke, and M. Ernzerhof, *Generalized Gradient Approximation Made Simple.* Physical Review Letters, 1996. **77**(18): p. 3865-3868.
30. Dudarev, S.L., et al., *Electron-energy-loss spectra and the structural stability of nickel oxide: An LSDA+U study.* Physical Review B, 1998. **57**(3): p. 1505-1509.
31. Erhart, P., et al., *Efficacy of the DFT+U formalism for modeling hole polarons in perovskite oxides.* Physical Review B, 2014. **90**(3): p. 035204.
32. Blöchl, P.E., *Projector augmented-wave method.* Physical Review B, 1994. **50**(24): p. 17953-17979.
33. Kresse, G. and D. Joubert, *From ultrasoft pseudopotentials to the projector augmented-wave method.* Physical Review B, 1999. **59**(3): p. 1758-1775.
34. Togo, A. and I. Tanaka, *First principles phonon calculations in materials science.* Scripta Materialia, 2015. **108**: p. 1-5.
35. Eglitis, R.I., *Ab initio calculations of the atomic and electronic structure of $BaZrO_3$ (111) surfaces.* Solid State Ionics, 2013. **230**: p. 43-47.
36. Eglitis, R.I., *Comparative ab initio calculations of $SrTiO_3$ and $CaTiO_3$ polar (111) surfaces.* physica status solidi (b), 2015. **252**(3): p. 635-642.
37. Kreuer, K.D., et al., *Proton conducting alkaline earth zirconates and titanates for high drain electrochemical applications.* Solid State Ionics, 2001. **145**(1): p. 295-306.

38. Björketun, M.E., P.G. Sundell, and G. Wahnström, *Structure and thermodynamic stability of hydrogen interstitials in $BaZrO_3$ perovskite oxide from density functional calculations.* Faraday Discussions, 2007. **134**(0): p. 247-265.
39. Waser, R., *Proton Solubility in Undoped and Fe-doped $SrTiO_3$: Temperature Dependence and Formation of Defect Associates.* Zeitschrift fur Naturforschung - Section A Journal of Physical Sciences, 1987. **42**(11): p. 1357-1365.
40. Mi, S.B., et al., *High-resolution electron microscopy of microstructure of $SrTiO_3$/$BaZrO_3$ bilayer thin films on MgO substrates.* Journal of Crystal Growth, 2007. **300**(2): p. 478-482.
41. Polfus, J.M., et al., *Defect chemistry of a $BaZrO_3$ Σ3 (111) grain boundary by first principles calculations and space-charge theory.* Physical Chemistry Chemical Physics, 2012. **14**(35): p. 12339-12346.
42. Shirpour, M., et al., *Dopant Segregation and Space Charge Effects in Proton-Conducting $BaZrO_3$ Perovskites.* The Journal of Physical Chemistry C, 2012. **116**(3): p. 2453-2461.
43. Chiang, Y.-M. and T. Takagi, *Grain-Boundary Chemistry of Barium Titanate and Strontium Titanate: I, High-Temperature Equilibrium Space Charge.* Journal of the American Ceramic Society, 1990. **73**(11): p. 3278-3285.
44. Bjørheim, T.S., E.A. Kotomin, and J. Maier, *Hydration entropy of $BaZrO_3$ from first principles phonon calculations.* Journal of Materials Chemistry A, 2015. **3**(14): p. 7639-7648.

Manuscript II

First principles analyses of nanoionic effects at oxide heterointerfaces for electrochemical applications, S.W. Saeed, *To be submitted*

Manuscript III

Surface Segregation Entropy of Protons and Oxygen Vacancies in $BaZrO_3$, T.S. Bjørheim, M. Arrigoni, S.W. Saeed, E. Kotomin and J. Maier, *Chemistry of Materials*, 2016, **28** (5), 1363-1368

CHEMISTRY OF MATERIALS

Article

pubs.acs.org/cm

Surface Segregation Entropy of Protons and Oxygen Vacancies in $BaZrO_3$

Tor S. Bjørheim,*[,†] Marco Arrigoni,[‡] Sarmad W. Saeed,[†] Eugene Kotomin,[‡,§] and Joachim Maier[‡]

[†]Centre for Materials Science and Nanotechnology, Department of Chemistry, University of Oslo, FERMiO Gaustadalléen 21, 0349 Oslo, Norway

[‡]Max Planck Institute for Solid State Research, Heisenbergstrasse 1, D-70569 Stuttgart, Germany

[§]Institute for Solid State Physics, University of Latvia, Kengaraga 8, LV-1063 Riga, Latvia

ABSTRACT: The perovskite $BaZrO_3$ has attracted considerable attention in the recent decade due to its high temperature proton conducting properties, and possible application as electrolyte in intermediate temperature fuel cells and electrolyzers. In this contribution, we performed, for the first time, first-principles calculations of the phonon contribution to the defect thermodynamics of the ZrO_2 terminated (001) surface of $BaZrO_3$. The approach allows us to determine both the segregation *enthalpy* and *entropy* of defects, which we apply to two fundamental defects in $BaZrO_3$; fully charged oxygen vacancies ($v_O^{\bullet\bullet}$) and protonic defects ($OH_O^{\bullet}$). The calculations show that both defects exhibit favorable segregation enthalpies of −65 and −125 kJ/mol, respectively. Further, the vibrational formation entropy of the surface $v_O^{\bullet\bullet}$ is significantly higher than that of the bulk $v_O^{\bullet\bullet}$, due to smaller local structural relaxations of the surface defect, leading to a finite surface segregation entropy of 53 J/mol K. $OH_O^{\bullet}$, on the other hand, displays nearly identical vibrational spectra at the surface and in the bulk, and the segregation entropy is therefore negligible. Hence, phonons not only stabilize the surface $v_O^{\bullet\bullet}$ compared to the bulk defect thermodynamically at high temperatures, but also affect the relative stability of $v_O^{\bullet\bullet}$ and $OH_O^{\bullet}$ at the surface. Finally, we apply a simplified space charge model to the (001) surface, and show that neglect of phonons results in strongly underestimated surface concentrations of $v_O^{\bullet\bullet}$.

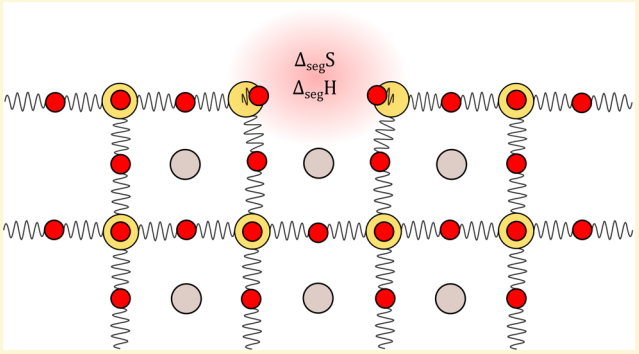

1. INTRODUCTION

ABO_3 type perovskite structured oxides comprise a broad family of materials with numerous technological applications ranging from electrolytes in solid oxide fuel cells and electrolyzers, to dielectrics, piezoelectrics, and catalysts.[1−4] $BaZrO_3$, a common perovskite, has attracted considerable attention over the past decade, mainly due to its high temperature proton conducting properties. Y-doped $BaZrO_3$ is currently considered the *most* promising electrolyte material for intermediate temperature proton conducting fuel cells.[5−9] The material is dominated by charge-compensating doubly charged oxygen vacancies, $v_O^{\bullet\bullet}$, which upon exposure to humid atmospheres, can be replaced by protonic defects, $OH_O^{\bullet}$:

$$H_2O(g) + O_O^{\times} + v_O^{\bullet\bullet} \rightleftharpoons 2OH_O^{\bullet} \quad (1)$$

The concentration of $v_O^{\bullet\bullet}$ and $OH_O^{\bullet}$ are determined by the hydration thermodynamics through the corresponding equilibrium constant

$$K = \frac{(c_{OH_O^{\bullet}})^2}{c_{v_O^{\bullet\bullet}} c_{O_O^{\times}} a_{P_{H_2O}}} = \exp\left(\frac{\Delta_{Hydr}S^{\circ}}{R}\right)\exp\left(-\frac{\Delta_{Hydr}H^{\circ}}{RT}\right) \quad (2)$$

where $\Delta_{Hydr}H^{\circ}$ and $\Delta_{Hydr}S^{\circ}$ are the standard enthalpy and entropy of hydration, respectively. $\Delta_{Hydr}H^{\circ}$ is usually found to depend on the electronegativity of the acceptor cations,[7,10,11] while the compositional dependency of $\Delta_{Hydr}S^{\circ}$ is somewhat unclear.[12]

While $BaZrO_3$ displays high bulk proton conductivity, grain boundary effects are known to deteriorate the functional properties of the polycrystalline ceramic. Polycrystalline $BaZrO_3$, for instance, displays high grain boundary resistance, which is attributed to positively charged grain boundary cores, resulting in $v_O^{\bullet\bullet}$ and $OH_O^{\bullet}$ depletion of the surrounding space charge layers.[13−19] Several authors have explored the segregation properties of $v_O^{\bullet\bullet}$ and $OH_O^{\bullet}$ to various grain boundaries in $BaZrO_3$ computationally, and shown that both $v_O^{\bullet\bullet}$ and $OH_O^{\bullet}$ display exothermic segregation enthalpies which result in their accumulation in the grain boundary core, and thus a positive space charge potential.[20−24]

Tauer et al.[25] recently reported that $OH_O^{\bullet}$ displays a favorable segregation enthalpy of around −100 kJ/mol to the ZrO_2 terminated (001) surface of $BaZrO_3$, while $v_O^{\bullet\bullet}$ was reported to be equally stable at the surface and in the bulk.[26] On the other hand, Bandura et al.[27] concluded that $v_O^{\bullet\bullet}$ formation is favored by

Received: November 9, 2015
Revised: January 12, 2016
Published: January 12, 2016

DOI: 10.1021/acs.chemmater.5b04327
Chem. Mater. 2016, 28, 1363−1368

>190 kJ/mol at the same surface compared to the bulk. In a more complete study of the BaO terminated (001) surface, Kim et al.[28] reported segregation energies of −93 and −41 kJ/mol of $OH_O^{\bullet}$ and $v_O^{\bullet\bullet}$, respectively. Hence, segregation of $OH_O^{\bullet}$ and/or $v_O^{\bullet\bullet}$ to $BaZrO_3$ surfaces has a similar effect as that in grain boundaries, giving rise to a positively charged surface, and negatively charged subsurface space charge regions,[28] which ultimately may affect the kinetics of, e.g., proton incorporation at the surfaces of $BaZrO_3$ thin film based membranes. It is therefore imperative to understand the defect thermodynamics of $BaZrO_3$, both of the bulk material and its surfaces and interfaces. The majority of numerous first-principles investigations of defect properties of $BaZrO_3$, and also oxides in general, have, however, neglected the vibrational properties of the materials and thus the phonon contribution to the defect thermodynamics. This approximation has recently been justified for neutral oxygen vacancies $v_O^{\times}$ in, e.g., $SrTiO_3$[29] and also $BaZrO_3$,[30] where the phonon contribution is small. For $v_O^{\bullet\bullet}$ on the other hand, we showed, from first-principles density functional theory (DFT) calculations, that the phonon contribution to the formation entropy is as large as −120 J/mol K at 1000 K.[12] The effect was attributed to both local structural relaxations and a significant negative formation volume of $v_O^{\bullet\bullet}$, leading to a general blue-shift of the phonon spectrum. As the entropy of a defect is closely related to its effect on the local structure, surfaces and interfaces may display widely different defect entropies from the bulk oxide. While numerous studies have evaluated the segregation *enthalpy* of defects with respect to grain boundaries[21−23,31] and surfaces[25,26] in a variety of oxides, the respective segregation *entropy* of defects is largely neglected.

In this contribution, we, to the best of our knowledge, for the first time determine the phonon contribution to the thermodynamic stability of surface $v_O^{\bullet\bullet}$ and $OH_O^{\bullet}$ in $BaZrO_3$ and, thus, their surface segregation entropies. We adopt first-principles calculations and phonon calculations within the harmonic approximation through the finite displacements method. We investigate $v_O^{\bullet\bullet}$ and $OH_O^{\bullet}$ at the (001) ZrO_2 terminated surface of $BaZrO_3$, and address the effect of slab thickness on the defect entropies. The calculated vibrational entropies are compared with those of the corresponding defects in the bulk of $BaZrO_3$, allowing for the determination of their segregation entropies. Finally, we discuss the effect of phonons on the space charge potential at this typical surface termination of $BaZrO_3$ assuming a simplified surface defect structure.

2. COMPUTATIONAL METHODOLOGY

The calculations are performed with two comparative methods: the plane-wave projector augmented wave (PAW) method[32] in VASP[33,34] with the pure DFT GGA-PBE functional,[35] and LCAO based calculations with the hybrid Hartree−Fock DFT exchange-correlation functional, PBE0, in CRYSTAL. The plane-wave calculations were performed with constant cutoff energy of 500 eV, and Ba, Zr, and O potentials with the valence configurations $5s^25p^66s^2$, $4s^24p^64d^25s^2$, and $2s^22p^4$, respectively. The calculations were performed using a reciprocal projection scheme with ionic and electronic convergence criteria of 10^{-4} eV/Å and 10^{-8} eV, respectively. Symmetric ZrO_2 terminated slab models consisting of 7−21 atomic layers were constructed from the bulk unit cell, and separated by a vacuum layer of 25 Å. Defect calculations were performed with either 3 × 3 or 4 × 4 supercell expansions of the surface unit cell in the *ab*-plane, with **k**-point sampling performed according to a 2 × 2 × 1 Monkhorst−Pack scheme for the supercells. Due to the large number of atomic displacements required for determination of the phonon spectra of the defective slabs, the phonon calculations were only performed with 3 × 3 *ab*-plane supercell expansions.

LCAO calculations were performed with the CRYSTAL code using atomic basis sets consisting of Gaussian type functions and pseudopotentials, and the hybrid DFT-HF functional PBE0. The basis sets included quasirelativistic pseudopotentials, with 46 and 28 core electrons of Ba and Zr, respectively, and the all-electron basis set 8-411G for O. For the oxygen vacancy, the basis set of the vacant oxygen atom was maintained by means of a spurious "ghost" atom with no atomic mass. Further details on the adopted pseudopotentials may be found in ref 30. The energy-convergence criterion for the self-consistent calculations was set to 10^{-7} eV. With CRYSTAL, the slab calculations were performed without periodic boundary conditions in the direction normal to the surface (i.e., no need for a vacuum layer). Due to the large computational costs associated with the PBE0 functional, the CRYSTAL/PBE0 calculations were limited to 7 atomic layer thick slabs.

With both codes, all calculations were performed by optimiziation of the *ab* lattice parameters and the slab thickness upon defect formation, and therefore represent *zero/constant pressure* conditions.

The phonon frequencies were obtained within the harmonic approximation using finite ionic displacements of ±0.005 Å. The electronic structure of all distorted cells was converged to within 10^{-8} eV, and the resulting Hellmann−Feynman forces acting on all ions were used to build the force constant matrices. With VASP, phonon frequencies and thermodynamic properties were evaluated using the Phonopy code.[36] Anharmonic effects were not included for any of the studied systems. For the defect-free slabs, the phonon dispersion along the high symmetry directions Γ → X → M → Γ was calculated using 2 × 2 and 3 × 3 *ab*-plane supercell expansions of the slab unit cell, revealing no imaginary frequencies for any of the slab thicknesses. In addition, all slab models displayed only minor structural relaxations in the near-surface layers, indicating that the ZrO_2 terminated (001) $BaZrO_3$ surface does not induce any long-range structural distortions such as those shown for $SrTiO_3$ grain boundaries.[37]

The main objective of this work is to determine the contribution from phonons to the thermodynamic stability of $v_O^{\bullet\bullet}$ and $OH_O^{\bullet}$ at the ZrO_2 terminated (001) surface of $BaZrO_3$, compared to that in the bulk, i.e., both the segregation enthalpy, $\Delta_{seg}H$, and entropy, $\Delta_{seg}S$. By including phonon contributions, the expression for the free energy of formation of a defect, $\Delta_F F_{defect}$, becomes

$$\Delta_F F_{defect} = \Delta_F E_{defect}^{el} + \Delta_F F_{defect}^{vib} + \sum_1^i \Delta n_i \mu_i(T, p) + q(\varepsilon_f + \Delta\epsilon) \tag{3}$$

where $\Delta_F E_{defect}^{el}$ and $\Delta_F F_{defect}^{vib}$ are the electronic and vibrational (phonon) part of the formation energy, respectively. Further, Δn_i is the change in the number of atom i with chemical potential μ_i, q is the effective charge of the defect, ε_f is the Fermi level, and $\Delta\epsilon$ aligns the core potentials of the perfect and the defective supercells to remedy shifts in the band edges due to the jellium background charge. The phonon contribution to the free energy and entropy can be determined from changes in the phonon spectrum upon defect formation according to

$$F^{vib} = \frac{1}{2}\sum_{\mathbf{q},s} h\nu(\mathbf{q}, s) + k_B T \sum_{\mathbf{q},s} \ln\left[1 - \exp\left(-\frac{h\nu(\mathbf{q}, s)}{k_B T}\right)\right] \tag{4}$$

$$S^{vib} = -k_B \sum_{\mathbf{q},s} \ln\left(1 - \exp\left(-\frac{h\nu(\mathbf{q}, s)}{k_B T}\right)\right) + \frac{1}{T}\sum_{\mathbf{q},s} \frac{h\nu(\mathbf{q}, s)}{\exp\left(\frac{h\nu(\mathbf{q},s)}{k_B T}\right) - 1} \tag{5}$$

where $\nu(\mathbf{q}, s)$ are the phonon frequencies at each **q**-point. Although eqs 4 and 5 sum over all **q**-points, the defect thermodynamics have in this contribution only been evaluated from phonon frequencies at the Γ-point of the 3 × 3 slab supercell expansions due to the large size of these slabs.

The phonon calculations were performed by introducing a $v_O^{\bullet\bullet}$ or $OH_O^{\bullet}$ on each side of the slab to maintain symmetry and avoid structural instabilities. The charge of the slabs was adjusted to simulate the desired

DOI: 10.1021/acs.chemmater.5b04327
Chem. Mater. 2016, 28, 1363−1368

charge state of the defects, which was compensated by standard means of an opposite homogeneous background charge. $\Delta_{seg}S$ was in turn determined from the entropy of the surface defect relative to the entropy of the defect in the central plane of the slabs.

To remedy shifts in the reference energy (i.e., the Hartree potential) of the defective slabs, the segregation enthalpies, $\Delta_{seg}H$, were determined by introducing charge-compensating defects in the central plane of the slabs, as adopted for defects at, e.g., TiO_2 surfaces.[38] For $v_O^{\bullet\bullet}$, we used either a central plane $v_{Ba}^{//}$ together with a single surface $v_O^{\bullet\bullet}$ (i.e., asymmetric defective slab), or a central plane $v_{Zr}^{////}$ and one surface $v_O^{\bullet\bullet}$ at each side of the slab (symmetric). For $OH_O^{\bullet}$, we used a single central plane $N_O^{/}$ defect and one surface $OH_O^{\bullet}$ (asymmetric), and a symmetric configuration with a single central plane $v_{Ba}^{//}$ with one $OH_O^{\bullet}$ at each side of the slab. To minimize in-plane defect interactions, the calculations were performed using 4×4 *ab*-plane expansions of the 11 layer (for the pairs $v_{Ba}^{//} + v_O^{\bullet\bullet}$, $v_{Ba}^{//} + 2 \times OH_O^{\bullet}$, and $N_O^{/} + OH_O^{\bullet}$) and 13 layer (for $v_{Zr}^{////} + 2 \times v_O^{\bullet\bullet}$) thick slabs. To account for the slab thickness dependence of $\Delta_{seg}H$ due to electrostatic interactions between the oppositely charged defects, $\Delta_{seg}H$ was also calculated using 3×3 *ab*-plane expansions of 11 and 19 layer thick slabs with $v_{Ba}^{//}$ as the charge-compensating defect for both $v_O^{\bullet\bullet}$ and $OH_O^{\bullet}$. $\Delta_{seg}H$ was subsequently determined from the formation energy difference of the defect pair in the slabs with respect to that of the isolated defects in a $4 \times 4 \times 4$ bulk $BaZrO_3$ supercell, thus avoiding effects from association/complex formation with the compensating defects.

3. RESULTS AND DISCUSSION

The calculations yielded $\Delta_{seg}H$ of −90 kJ/mol (asymmetric, 11 layers) and −75 kJ/mol (symmetric, 13 layers) for $v_O^{\bullet\bullet}$, and −133 kJ/mol (asymmetric, 11 layers) and −131 kJ/mol (symmetric, 11 layers) for $OH_O^{\bullet}$. $\Delta_{seg}H$ was for both defects found to depend on the slab thickness, increasing by 25 and 5 kJ/mol for $v_O^{\bullet\bullet}$ and $OH_O^{\bullet}$, respectively, from the 11 to the 19 atomic layer thick slabs. With $v_O^{\bullet\bullet}$ in the central layers of the 19 layer thick slab, the calculated $\Delta_{seg}H$ was only slightly less exothermic, −50 kJ/mol, thereby lending support to our adopted method. To account for this slab thickness dependence, and in order to not overestimate $\Delta_{seg}H$, we have in space charge model used the values −125 for $OH_O^{\bullet}$, and −65 kJ/mol for $v_O^{\bullet\bullet}$. For $v_O^{\bullet\bullet}$, our segregation energy is in contrast to Tauer et al.[26] who showed no tendency for $v_O^{\bullet\bullet}$ segregation to the ZrO_2 terminated (001) surface, while our $\Delta_{seg}H$ for $OH_O^{\bullet}$ is more exothermic by ∼25 kJ/mol. We suggest that this stems from the adopted PW91 functional in the study of Tauer et al.,[26] which affects the stability of the cubic $BaZrO_3$ structure. Our calculated segregation enthalpies are also somewhat more exothermic than those found by Kim et al. for the BaO terminated (001) surface.[28]

Figure 1 shows the zero/constant pressure phonon contribution to the formation entropy ($\Delta_F S^{vib}$) of $v_O^{\bullet\bullet}$ in the central plane of the slab and at the surface, compared with that of $v_O^{\bullet\bullet}$ in a $3 \times 3 \times 3$ bulk supercell from ref 12. $\Delta_F S^{vib}$ of the surface $v_O^{\bullet\bullet}$ is well-converged even within the 7 atomic layer slabs, while that of the central plane $v_O^{\bullet\bullet}$ changes somewhat between the different slabs. Further, $\Delta_F S^{vib}$ calculated with the 9 layer slab is nearly identical to that of the "true" bulk $v_O^{\bullet\bullet}$, while those calculated with the 7 and 11 layer slabs are somewhat less negative. This slab thickness dependence may in part be attributed to the decreasing frequency of the 3 lowest frequency modes (i.e., with origin at the R-point of bulk cell), especially for the 11 layer slab, and also to whether BaO or ZrO_2 constitutes the central plane of the slab. $\Delta_F S^{vib}$ of the surface $v_O^{\bullet\bullet}$ is notably less negative than that for the central plane/bulk $v_O^{\bullet\bullet}$, and phonons therefore give rise to a finite and positive segregation entropy ($\Delta_{seg}S$) for $v_O^{\bullet\bullet}$ (Figure 2). While $\Delta_F S^{vib}$ of both the surface and bulk $v_O^{\bullet\bullet}$ is strongly temperature dependent, $\Delta_{seg}S$ reaches a constant value between

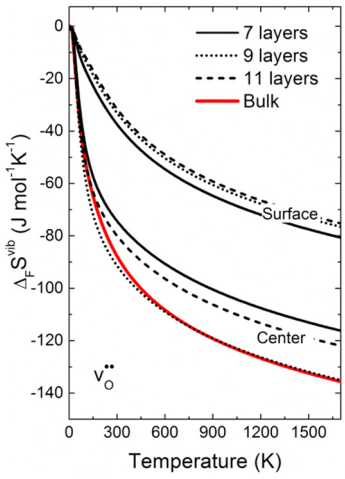

Figure 1. Phonon contribution to the formation entropy ($\Delta_F S^{vib}$) of $v_O^{\bullet\bullet}$ in 7, 9, and 11 layer thick (001) ZrO_2 terminated slabs, and bulk $BaZrO_3$, calculated with VASP/PBE. The calculations are performed with zero/constant pressure.

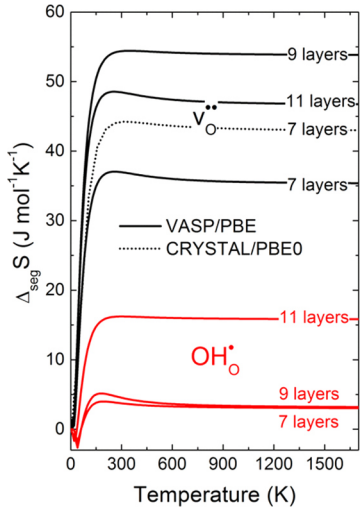

Figure 2. $\Delta_{seg}S$ of $v_O^{\bullet\bullet}$ and $OH_O^{\bullet}$ calculated with 7, 9, and 11 atomic layer thick slabs of the ZrO_2 terminated (001) surface of $BaZrO_3$. For $v_O^{\bullet\bullet}$, the calculations are performed with both VASP/PBE (solid black) and CRYSTAL/PBE0 (dotted black) for comparison. The "bulk" references for calculation of $\Delta_{seg}S$ are taken as the central plane defects as shown for $v_O^{\bullet\bullet}$ in Figure 1.

35 and 53 J/mol K with the different slab thicknesses above ∼350 K. The $\Delta_{seg}S$ of $v_O^{\bullet\bullet}$ calculated with VASP/PBE is also in very good agreement with the 43 J/mol K obtained with CRYSTAL/PBE0 and a 7 layer slab.

The $\Delta_{seg}S$ of $OH_O^{\bullet}$ is considerably smaller than that of $v_O^{\bullet\bullet}$, reflecting that the lattice relaxation of the surface $OH_O^{\bullet}$ is similar to that of the bulk species. As noted for $\Delta_F S^{vib}$ of $v_O^{\bullet\bullet}$, the $\Delta_{seg}S$ for both $v_O^{\bullet\bullet}$ and $OH_O^{\bullet}$ also display a notable slab thickness dependence. Since the 9 layer thick slab gives a $\Delta_F S^{vib}$ of the central plane $v_O^{\bullet\bullet}$ in closest agreement with that of the "true" defect, we conclude that this slab thickness gives the most realistic representation of the vibrational segregation properties of $v_O^{\bullet\bullet}$ and $OH_O^{\bullet}$. Hence, the vibrational $\Delta_{seg}S$ of $v_O^{\bullet\bullet}$ and $OH_O^{\bullet}$ are 53 and 5 J/mol K, respectively.

Protons in bulk $BaZrO_3$ may take on four distinct configurations around each O ion.[12] The number of O−H

DOI: 10.1021/acs.chemmater.5b04327
Chem. Mater. 2016, 28, 1363−1368

configurations affects the chemical potential of $OH_O^{\bullet}$ in the bulk and at the surface, and neglecting these configurations therefore gives rise to an "apparent" $\Delta_{hydr}S$, and $\Delta_{seg}S$ (see ref 12 for details). At the ZrO_2 terminated (001) surface, we find that the two configurations with the O−H axis aligned parallel with the surface plane are more favorable than those with the O−H axis normal to the surface. Neglecting these configurations in the statistical description of bulk and surface protons gives rise to a factor $R\ln(2/4)$, or −5.7 J/mol K, in $\Delta_{seg}S$, and the apparent, or effective, $\Delta_{seg}S$ (i.e., including vibrational and configurational contributions) of $OH_O^{\bullet}$ is therefore close to zero.

Figure 3 shows the structural relaxations around the surface and bulk $v_O^{\bullet\bullet}$. Both defects lead to an outward relaxation of the

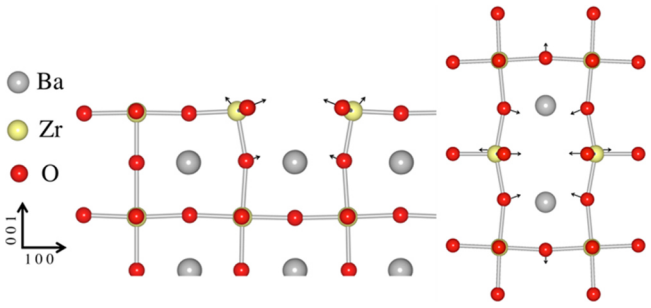

Figure 3. Local structural relaxations around $v_O^{\bullet\bullet}$ (left) at the ZrO_2 terminated (001) surface, and (right) in bulk $BaZrO_3$.

two nearest Zr ions, and an inward relaxation of the nearest-neighbor O ions. The relaxations are somewhat smaller for the surface $v_O^{\bullet\bullet}$, which explains the positive $\Delta_{seg}S$ of $v_O^{\bullet\bullet}$. In addition, $\Delta_{seg}S$ may stem from the lower coordination number of O and Zr ions at the surface and hence the fewer Zr−O bonds/modes which are broken/affected by $v_O^{\bullet\bullet}$ formation. The difference in the vibrational PDOS of bulk and surface O ions was found to account for merely 10−15% of the calculated $\Delta_{seg}S$, and the major contribution therefore stems from the effect of $v_O^{\bullet\bullet}$ on the local structure as shown in Figure 3.

The calculated bulk $\Delta_{Hydr}H^{\circ}$ (according to eq 1) at 0 K is −72 kJ/mol (see ref 12 for details), in good agreement with the experimental value of −80 kJ/mol.[6,7] From $\Delta_{seg}H$ of $v_O^{\bullet\bullet}$ and $OH_O^{\bullet}$, $\Delta_{Hydr}H^{\circ}$ of the ZrO_2 terminated (001) surface is significantly more favorable, −257 kJ/mol. Figure 4 compares the apparent $\Delta_{Hydr}S^{\circ}$ (i.e., including the configurational contributions stemming from the number of proton configurations around each O ion, 23 J/mol K for bulk, and 11.5 J/mol

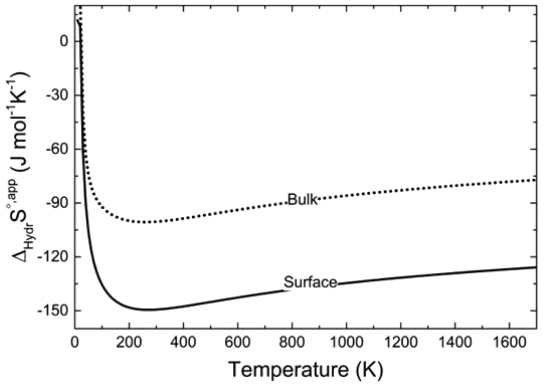

Figure 4. Bulk and surface hydration entropy (apparent $\Delta_{Hydr}S^{\circ}$) of $BaZrO_3$ and its ZrO_2 terminated (001) surface.

K for the surface) for bulk $BaZrO_3$ and the surface. Throughout the temperature interval, the hydration entropy of the surface is ∼50 J/mol K more negative than that of the bulk due to the positive segregation entropy of $v_O^{\bullet\bullet}$. Hence, inclusion of the segregation entropies destabilizes protons relative to oxygen vacancies at the surface.

We finally assess the effect of phonons (i.e., the entropy of segregation) on the surface defect chemistry of $BaZrO_3$, and corresponding space charge properties. The appropriate model is the core−space charge model as described in refs 39 and 40 in which the core layer has an electrical potential different from the adjacent space charge layers. Here, we apply the simplified Gouy−Chapman space charge model after Kliewer and Koehler,[41] which often is adopted in numerical analyses of grain boundaries and surfaces in $BaZrO_3$, and similar materials.[21−24,42] We assume that the defect structure of the bulk oxide is dominated by the simplified electroneutrality

$$c_{Acceptor} = 2c_{v_O^{\bullet\bullet}} + c_{OH_O^{\bullet}} \tag{7}$$

according to eqs 1 and 2, and that only $v_O^{\bullet\bullet}$ and $OH_O^{\bullet}$ segregate/are formed at the surface (i.e., neglecting surface ad-ions). The electrochemical potentials are taken as

$$\tilde{\mu}_i(x) = \mu_i^{\circ}(x) + RT\ln\left(\frac{c_i(x)}{c_i^0 - c_i(x)}\right) + z_iF\varphi(x) \tag{8}$$

where $\mu_i^{\circ}(x)$ is the free energy of formation of species i, and $c_i(x)$ and c_i^0 are the defect and lattice site concentrations, respectively, while $\varphi(x)$ is the electrostatic potential at a distance x from the surface. From the requirement of constant electrochemical potentials

$$\tilde{\mu}_i(\infty) = \tilde{\mu}_i(x) = \tilde{\mu}_i^{surf} \tag{9}$$

the concentrations of defects in bulk, surface, and the space charge region can be determined through

$$\frac{c_i(x)}{c_{i,S}^0 - c_i(x)} = \frac{c_i(\infty)}{c_{i,bulk}^0 - c_i(\infty)}\exp\left(-\frac{\Delta\mu_i^{\circ} + z_iF\Phi_s}{RT}\right) \tag{10}$$

$\Delta\mu_i^{\circ}$ is the segregation free energy of species i, and Φ_s is the electrostatic potential difference between bulk and the surface (surface Schottky barrier height). For x between 0 and ∞ (i.e., the space charge region) we assume that $\Delta\mu_i^{\circ} = 0$, and the defect concentrations only depend on the bulk defect concentration and the electrostatic potential at point x.

The electrostatic potential and charge density are related through the Poisson equation

$$\frac{\delta^2\varphi(x)}{\delta x^2} = -\frac{\rho(x)}{\varepsilon_r\varepsilon} \tag{11}$$

where $\rho(x)$, the charge density, is given by $c_i(x)$. Equation 11 was solved numerically with the boundary conditions $\frac{\delta\varphi(x\to\infty)}{\delta x} = 0$ and $\varphi\ (x\to 0) = \Phi_s$ by iteration over Φ_s until the total charge density complied with the global electroneutrality condition of the interface/space charge region:

$$\sum_i z_i e c_{i,surface} + \sum_i \int_0^{\infty} z_i e c_i(x)\,dx = 0 \tag{12}$$

Figure 5 shows the resulting concentration and electrostatic potential profiles at 1000 K by assuming 10 mol % acceptor doped $BaZrO_3$, $\Delta_{Hydr}H^{\circ}$ = −72 kJ/mol, a constant "apparent"

DOI: 10.1021/acs.chemmater.5b04327
Chem. Mater. 2016, 28, 1363−1368

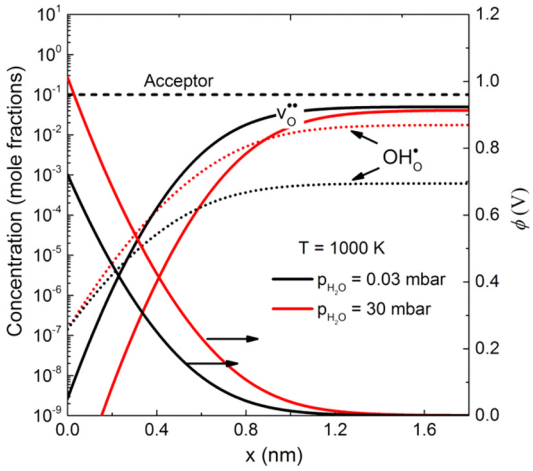

Figure 5. Defect concentrations and electrostatic potential profiles as a function of depth (in nm) from the ZrO_2 terminated (001) surface of 10 mol % acceptor doped $BaZrO_3$ at 1000 K with p_{H_2O} = 30 mbar or 0.03 mbar, under the assumption that only $v_O^{\bullet\bullet}$ and $OH_O^{\bullet}$ are formed on the surface, and a constant acceptor concentration.

$\Delta_{Hydr}S^{\circ}$ of −90 J/mol K (Figure 4), $\Delta_{seg}H$ = −65 kJ/mol, and $\Delta_{seg}S$ = 53 J/mol K for $v_O^{\bullet\bullet}$, and $\Delta_{seg}H$ = −125 kJ/mol and $\Delta_{seg}S$ = 0 J/mol K for $OH_O^{\bullet}$. The corresponding surface defect concentrations are shown in Table 1. Under both dry and wet conditions, Φ_s is large and positive, and increases with increasing water vapor partial pressure. The positive surface charge is primarily due to the strong segregation of $OH_O^{\bullet}$, and $v_O^{\bullet\bullet}$ is in complete minority with respect to $OH_O^{\bullet}$ at the surface, even under dry conditions. Our Φ_s values are in the range of values determined computationally for the BaO terminated (001) surface of $BaZrO_3$ by Kim et al.[28] A positive surface charge has also been inferred experimentally by De Souza et al.,[42] for TiO_2 terminated (001) oriented $SrTiO_3$ single crystals from ^{18}O concentration profiles, which was explained by segregation of $v_O^{\bullet\bullet}$ to the surface. On the other hand, we expect that $OH_O^{\bullet}$ are important defects also at the surfaces of $SrTiO_3$, which would affect the experimentally determined surface segregation energies of $v_O^{\bullet\bullet}$ reported in ref 42.

Due to the dominance of $OH_O^{\bullet}$ at the surface, inclusion of $\Delta_{seg}S$ barely affects Φ_s, the space charge concentration and potential profiles (i.e., width). Inclusion of $\Delta_{seg}S$, however, drastically increases the minority concentration of surface $v_O^{\bullet\bullet}$ under both dry and wet conditions, and is therefore important when evaluating the surface defect chemistry from, e.g., experimental defect concentration profiles. Although the strong $\Delta_{seg}H$ of $OH_O^{\bullet}$ in this particular case dominates the space charge properties, the effect of accounting for $\Delta_{seg}S$ of $v_O^{\bullet\bullet}$ will be somewhat larger at even higher temperatures, or for higher acceptor concentrations, when the surface concentration of $v_O^{\bullet\bullet}$ is higher. We also expect that the effect of $\Delta_{seg}S$ will be more significant in other oxides where bulk $OH_O^{\bullet}$ species are less dominant, such as $SrTiO_3$, or in oxides where $\Delta_{seg}H$ of $OH_O^{\bullet}$ is smaller. In addition, other surface species such as $OH_{ad}^{/}$ or acceptor defects (e.g., Y) will affect the surface defect structure and possibly reduce the surface space charge potential, especially at lower temperatures.

4. CONCLUSIONS

In conclusion, we have for the first time demonstrated that there is a notable difference in the entropy of fully charged $v_O^{\bullet\bullet}$ in the bulk and at the surface of an oxide, as exemplified by the ZrO_2 terminated (001) surface of $BaZrO_3$ (and also very likely applies to other ABO_3 type perovskites), resulting in a finite and positive surface defect segregation entropy, $\Delta_{seg}S$. The entropy of surface $OH_O^{\bullet}$ is, on the other hand, nearly identical to that of the bulk species due to a significantly smaller relaxation of the surrounding lattice. The overall agreement between the plane-wave based calculations using the pure DFT GGA-PBE functional, and the LCAO calculations with PBE0 lend support to the adopted method. For the ZrO_2 terminated (001) surface, the more exothermic surface segregation enthalpy, $\Delta_{seg}H$, of $OH_O^{\bullet}$ (−125 kJ/mol) than $v_O^{\bullet\bullet}$ (−65 kJ/mol) results in $OH_O^{\bullet}$ defects dominating the surface compared to $v_O^{\bullet\bullet}$, even under relatively dry conditions at high temperatures. The surface space charge potential is thus large, and positive, and is only affected by $\Delta_{seg}S$ of $v_O^{\bullet\bullet}$ under dry conditions at very high temperatures where the surface concentration of $OH_O^{\bullet}$ is low. Neglect of $\Delta_{seg}S$ has, however, a significantly stronger effect on the minority concentration of $v_O^{\bullet\bullet}$ at the surface, and thus phonons should be accounted for upon evaluation of the defect chemistry of surfaces with charged defects.

Table 1. Concentration (Site Occupancy) of $v_O^{\bullet\bullet}$ and $OH_O^{\bullet}$ at the (001) Surface of $BaZrO_3$ Calculated with and without the Segregation Entropy under Dry (p_{H_2O} = 0.03 mbar) and Wet (p_{H_2O} = 30 mbar) Conditions

	dry		wet	
	with $\Delta_{seg}S$	without $\Delta_{seg}S$	with $\Delta_{seg}S$	without $\Delta_{seg}S$
$c_{OH_O^{\bullet}}$	0.14	0.15	0.16	0.17
$c_{v_O^{\bullet\bullet}}$	1.2×10^{-3}	2.0×10^{-6}	1.1×10^{-6}	1.9×10^{-9}
Φ_s	0.71	0.72	1.01	1.01

AUTHOR INFORMATION

Corresponding Author

*E-mail: torsb@kjemi.uio.no.

Notes

The authors declare no competing financial interest.

ACKNOWLEDGMENTS

T.S.B. and S.W.S gratefully acknowledge the Research Council of Norway (RCN) for funding under the project "HydraTherm-Pro" (Project 214252), and the BIGCCS Centre (Project 193816) under the Norwegian research program Centres for Environment-Friendly Energy Research (FME). E.K. acknowledges partial funding through EC GREEN-CC FP7 (project 608524). We also thank the Norwegian Metacenter for Computational Science (NOTUR) for computational resources and excellent support (Project NN4604k). Lastly, we thank Dr. G. Gregori, Dr. R. Merkle, and Dr. J. Polfus for fruitful discussions.

REFERENCES

(1) Lines, M. E.; Glass, A. M. *Principles and Applications of Ferroelectrics and Related Materials*; Clarendon Press: Oxford, 1977.

(2) Donnerberg, H. J. *Atomic Simulations of Electro-Optical and Magneto-Optical Materials*; Springer: Berlin, 1999; Vol. *151*.

(3) Walsch, A.; Sokol, A.; Catlow, C. R. A. *Computational Approaches to Energy Materials*; Wiley, 2013.

(4) Kuklja, M. M.; Kotomin, E. A.; Merkle, R.; Mastrikov, Yu. A.; Maier, J. Combined Theoretical and Experimental Analysis of Processes

DOI: 10.1021/acs.chemmater.5b04327
Chem. Mater. 2016, 28, 1363−1368

Determining Cathode Performance in Solid Oxide Fuel Cells. *Phys. Chem. Chem. Phys.* **2013**, *15*, 5443−5471.
(5) Bohn, H. G.; Schober, T. Electrical Conductivity of the High-Temperature Proton Conductor $BaZr_{0.9}Y_{0.1}O_{2.95}$. *J. Am. Ceram. Soc.* **2000**, *83*, 768−772.
(6) Kreuer, K. D.; Adams, S.; Münch, W.; Fuchs, A.; Klock, U.; Maier, J. Proton Conducting Alkaline Earth Zirconates and Titanates for High Drain Electrochemical Applications. *Solid State Ionics* **2001**, *145*, 295−306.
(7) Kreuer, K. D. Proton Conducting Oxides. *Annu. Rev. Mater. Res.* **2003**, *33*, 333−359.
(8) Duval, S. B. C.; Holtappels, P.; Vogt, U. F.; Pomjakushina, E.; Conder, K.; Stimming, U.; Graule, T. Electrical Conductivity of the Proton Conductor $BaZr_{0.9}Y_{0.1}O_{3-\delta}$ Obtained by High Temperature Annealing. *Solid State Ionics* **2007**, *178*, 1437−1441.
(9) Yamazaki, Y.; Hernandez-Sanchez, R.; Haile, S. M. High Total Proton Conductivity in Large-Grained Yttrium-Doped Barium Zirconate. *Chem. Mater.* **2009**, *21*, 2755−2762.
(10) Norby, T.; Widerøe, M.; Glöckner, R.; Larring, Y. Hydrogen in Oxides. *Dalton Transactions* **2004**, 3012−3018.
(11) Bjørheim, T. S.; Kuwabara, A.; Ahmed, I.; Haugsrud, R.; Stølen, S.; Norby, T. A Combined Conductivity and DFT Study of Protons in $PbZrO_3$ and Alkaline Earth Zirconate Perovskites. *Solid State Ionics* **2010**, *181*, 130−137.
(12) Bjørheim, T. S.; Kotomin, E.; Maier, J. Hydration Entropy of $BaZrO_3$ from First Principles Phonon Calculations. *J. Mater. Chem. A* **2015**, *3*, 7639.
(13) Park, H. J.; Kwak, C.; Lee, K. H.; Lee, S. M.; Lee, E. S. Interfacial Protonic Conduction in Ceramics. *J. Eur. Ceram. Soc.* **2009**, *29*, 2429−2437.
(14) Kjølseth, C.; Wang, L.-Y.; Haugsrud, R.; Norby, T. Determination of the Enthalpy of Hydration of Oxygen Vacancies in Y-Doped $BaZrO_3$ and $BaCeO_3$ by TG-DSC. *Solid State Ionics* **2010**, *181*, 1740−1745.
(15) Shirpour, M.; Merkle, R.; Lin, C. T.; Maier, J. Nonlinear Electrical Grain Boundary Properties in Proton Conducting Y-$BaZrO_3$ Supporting the Space Charge Depletion Model. *Phys. Chem. Chem. Phys.* **2012**, *14*, 730−740.
(16) Shirpour, M.; Rahmati, B.; Sigle, W.; van Aken, P. A.; Merkle, R.; Maier, J. Dopant Segregation and Space Charge Effects in Proton-Conducting $BaZrO_3$ Perovskites. *J. Phys. Chem. C* **2012**, *116*, 2453−2461.
(17) Shirpour, M.; Merkle, R.; Maier, J. Space Charge Depletion in Grain Boundaries of $BaZrO_3$ Proton Conductors. *Solid State Ionics* **2012**, *225*, 304−307.
(18) Shirpour, M.; Gregori, G.; Houben, L.; Merkle, R.; Maier, J. High Spatially Resolved Cation Concentration Profile at the Grain Boundaries of Sc-Doped $BaZrO_3$. *Solid State Ionics* **2014**, *262*, 860−864.
(19) Kim, J.-S.; Yang, J.-H.; Kim, B.-K.; Kim, Y.-C. Study of Σ3 $BaZrO_3$ (210)[001] Tilt Grain Boundaries Using Density Functional Theory and a Space Charge Layer Model. *J. Ceram. Soc. Jpn.* **2015**, *123*, 245−249.
(20) Joakim Nyman, B.; Helgee, E. E.; Wahnström, G. Oxygen Vacancy Segregation and Space-Charge Effects in Grain Boundaries of Dry and Hydrated $BaZrO_3$. *Appl. Phys. Lett.* **2012**, *100*, 061903.
(21) Polfus, J. M.; Toyoura, K.; Oba, F.; Tanaka, I.; Haugsrud, R. Defect Chemistry of a $BaZrO_3$ Σ3 (111) Grain Boundary by First Principles Calculations and Space-Charge Theory. *Phys. Chem. Chem. Phys.* **2012**, *14*, 12339−12346.
(22) Helgee, E. E.; Lindman, A.; Wahnström, G. Origin of Space Charge in Grain Boundaries of Proton-Conducting $BaZrO_3$. *Fuel Cells* **2013**, *13*, 19−28.
(23) Lindman, A.; Helgee, E. E.; Wahnström, G. Theoretical Modeling of Defect Segregation and Space-Charge Formation in the $BaZrO_3$ (210)[001] Tilt Grain Boundary. *Solid State Ionics* **2013**, *252*, 121−125.
(24) Lindman, A.; Helgee, E. E.; Nyman, B. J.; Wahnström, G. Oxygen Vacancy Segregation in Grain Boundaries of $BaZrO_3$ Using Interatomic Potentials. *Solid State Ionics* **2013**, *230*, 27−31.
(25) Tauer, T.; O'Hayre, R.; Medlin, J. W. An Ab Initio Investigation of Proton Stability at $BaZrO_3$ Interfaces. *Chem. Mater.* **2014**, *26*, 4915−4924.
(26) Tauer, T.; O'Hayre, R.; Medlin, J. W. Computational Investigation of Defect Segregation at the (001) Surface of $BaCeO_3$ and $BaZrO_3$: the Role of Metal-Oxygen Bond Strength in Controlling Vacancy Segregation. *J. Mater. Chem. A* **2013**, *1*, 2840−2846.
(27) Bandura, A. V.; Evarestov, R. A.; Kuruch, D. D. LCAO Calculations of (001) Surface Oxygen Vacancy Structure in Y-Doped $BaZrO_3$. *Integr. Ferroelectr.* **2011**, *123*, 1−9.
(28) Kim, J.-S.; Yang, J.-H.; Kim, B.-K.; Kim, Y.-C. Proton Conduction at BaO-Terminated (001) $BaZrO_3$ Surface Using Density Functional Theory. *Solid State Ionics* **2015**, *275*, 19−22.
(29) Evarestov, R.; Blokhin, E.; Gryaznov, D.; Kotomin, E. A.; Merkle, R.; Maier, J. Jahn-Teller Effect in the Phonon Properties of Defective $SrTiO_3$ From First Principles. *Phys. Rev. B: Condens. Matter Mater. Phys.* **2012**, *85*, 174303.
(30) Bjørheim, T. S.; Arrigoni, M.; Gryaznov, D.; Kotomin, E.; Maier, J. Thermodynamic Properties of Neutral and Charged Oxygen Vacancies in $BaZrO_3$ Based on First Principles Phonon Calculations. *Phys. Chem. Chem. Phys.* **2015**, *17*, 20765−20774.
(31) Dawson, J. A.; Tanaka, I. Proton Incorporation and Trapping in ZrO_2 Grain Boundaries. *J. Mater. Chem. A* **2014**, *2*, 1400−1408.
(32) Blöchl, P. E. Projector Augmented-Wave Method. *Phys. Rev. B: Condens. Matter Mater. Phys.* **1994**, *50*, 17953−17979.
(33) Kresse, G.; Furthmüller, J. Efficient Iterative Schemes for Ab Initio Total-Energy Calculations Using a Plane-Wave Basis Set. *Phys. Rev. B: Condens. Matter Mater. Phys.* **1996**, *54*, 11169−11186.
(34) Kresse, G.; Joubert, D. From Ultrasoft Pseudopotentials to the Projector Augmented-Wave Method. *Phys. Rev. B: Condens. Matter Mater. Phys.* **1999**, *59*, 1758−1775.
(35) Perdew, J. P.; Burke, K.; Ernzerhof, M. Generalized Gradient Approximation Made Simple. *Phys. Rev. Lett.* **1996**, *77*, 3865−3868.
(36) Togo, A.; Oba, F.; Tanaka, I. First-Principles Calculations of the Ferroelastic Transition Between Rutile-Type and $CaCl_2$-Type SiO_2 at High Pressures. *Phys. Rev. B: Condens. Matter Mater. Phys.* **2008**, *78*, 134106.
(37) Schusteritsch, G.; Pickard, C. J. Predicting Interface Structures: From $SrTiO_3$ to Graphene. *Phys. Rev. B: Condens. Matter Mater. Phys.* **2014**, *90*, 035424.
(38) Bjørheim, T. S.; Kuwabara, A.; Mohn, C. E.; Norby, T. Defects at The (1 1 0) Surface of Rutile TiO_2 from Ab Initio Calculations. *Int. J. Hydrogen Energy* **2012**, *37*, 8110−8117.
(39) Maier, J. Space Charge Regions in Solid Two Phase Systems and Their Conduction Contribution. IV: The Behaviour of Minority Charge Carriers Part A: Concentration Profiles, Conductivity Contribution, Determination by Generalized Wagner-Hebb-Procedure. *Berichte der Bunsengesellschaft für physikalische Chemie* **1989**, *93*, 1468−1473.
(40) Jamnik, J.; Maier, J.; Pejovnik, S. Interfaces in Solid Ionic Conductors: Equilibrium and Small Signal Picture. *Solid State Ionics* **1995**, *75*, 51−58.
(41) Kliewer, K. L.; Koehler, J. S. Space Charge in Ionic Crystals. I. General Approach with Application to NaCl. *Phys. Rev.* **1965**, *140*, A1226−A1240.
(42) De Souza, R. A.; Metlenko, V.; Park, D.; Weirich, T. E. Behavior of Oxygen Vacancies in Single-Crystal $SrTiO_3$: Equilibrium Distribution and Diffusion Kinetics. *Phys. Rev. B: Condens. Matter Mater. Phys.* **2012**, *85*, 174109.

DOI: 10.1021/acs.chemmater.5b04327
Chem. Mater. 2016, 28, 1363−1368

Manuscript IV

The role of space-charge at metal/oxide interfaces in protonic ceramic cells, S.W. Saeed, *To be submitted*

Manuscript V

Alkali metals as efficient A-site acceptor dopants in proton conducting $BaZrO_3$, A. Løken, S.W. Saeed, M.N. Getz, X. Liu and T.S. Bjørheim, *Journal of Materials Chemistry A,* 2016, **4** (23), 9229-9235

Journal of Materials Chemistry A

PAPER

View Article Online
View Journal | View Issue

Cite this: J. Mater. Chem. A, 2016, 4, 9229

Alkali metals as efficient A-site acceptor dopants in proton conducting $BaZrO_3$

Andreas Løken, Sarmad W. Saeed, Marit N. Getz, Xin Liu and Tor S. Bjørheim*

In the present contribution, we assess the efficiency of the alkali metals (Na, K, Rb and Cs) as A-site acceptor dopants in proton conducting $BaZrO_3$ by first principles calculations. The calculated acceptor–proton complexes become weaker with increasing dopant size, with binding energies ranging from −0.33 eV for Na to −0.10 eV for Cs, which is in the range of, or even lower than, those found for B-site doped $BaZrO_3$. By mapping out all relevant minimum energy pathways for the proton, we reveal that the highest migration energy barrier for most of the alkali metals is comparable or even lower than that of Y. Further, all A-site dopants display more exothermic hydration enthalpies compared to that of Y-doped $BaZrO_3$, ranging from −131 kJ mol^{-1} to −83 kJ mol^{-1} for Na and Cs, respectively. The calculated dopant solubility increases in the order Na < Cs < Rb < K, with the predicted solubilities of the two latter being in the range of that of *e.g.* Y. Although Cs would lead to the highest proton mobility, the higher solubility of K and Rb renders them more attractive A-site dopants for $BaZrO_3$. Overall, our results suggest that alkali metals as A-site dopants may enhance the bulk proton conductivity of $BaZrO_3$, compared to Y-doped $BaZrO_3$.

Received 17th February 2016
Accepted 24th April 2016

DOI: 10.1039/c6ta01446a

www.rsc.org/MaterialsA

1 Introduction

Acceptor doped $BaZrO_3$ is currently considered the most promising electrolyte for proton conducting solid oxide fuel cells and electrolysers operating at intermediate temperatures (400–700 °C).[1] These acceptors are charge compensated by oxygen vacancies ($v_O^{\bullet\bullet}$) or protons ($OH_O^{\bullet}$) under dry or wet conditions, respectively, in which the relative dominance of the two defects is given by the hydration reaction;

$$H_2O(g) + v_O^{\bullet\bullet} + O_O^{\times} \leftrightarrows 2OH_O^{\bullet} \quad (1)$$

The thermodynamics of this equilibrium, or the enthalpy ($\Delta_{hydr}H^{\circ}$) and entropy ($\Delta_{hydr}S^{\circ}$) of hydration, is strongly materials dependent, and has for $BaZrO_3$ been shown to vary with both type and amount of acceptor dopant.[2,3] The dopant dependency of $\Delta_{hydr}H^{\circ}$ is closely related to the strength of the complexes between the negatively charged acceptors and protons and oxygen vacancies, which again depends on the chemical mismatch between the dopant and the host ion.[4]

Bulk Y-doped $BaZrO_3$ exhibits a maximum proton conductivity of ~0.01 S cm^{-1} at 600 °C.[5] However, the practically achievable conductivity is often significantly lower and poorly reproducible. This has been attributed to a plethora of effects including large grain boundary resistances,[6] Ba loss and partial Y dissolution on the A-site,[7,8] and complex formation and trapping.[9–13] While undoped bulk $BaZrO_3$ exhibits an activation energy of proton mobility of merely 0.16–0.20 eV,[9,11,12] nearly all B-site acceptor dopants (*e.g.* Sc, Y, Gd, Nd) increase this considerably due to complex formation between the acceptors and the mobile protons, thus lowering the proton conductivity. In this contribution, we explore A-site acceptor doping by alkali metals as a possible strategy to reduce the degree of proton trapping in $BaZrO_3$, and thereby increase the proton conductivity.

Although A-site doping of $BaZrO_3$ has been largely overlooked in literature, it has been shown to reduce the degree of defect trapping significantly compared to B-site doping in other oxides such as $LaScO_3$, $LaGaO_3$ and $LaNbO_4$.[14–17] Additionally, experimental work on $BaZrO_3$ co-doped with K on the A-site and Y on the B-site demonstrated that the partial proton conductivity was enhanced relative to that of Y-doped $BaZrO_3$. However, due to the presence of multiple dopants, it is difficult to ascertain how these compositions are actually affected by K-doping.[18,19] Recently, Sherafat *et al.*[20] measured the electrical conductivity of 15 mol% K-doped $BaZrO_3$, from which they evaluated its transport and defect chemical properties. K was shown to yield a hydration enthalpy of −90 kJ mol^{-1}, which is more negative than that of Y-doped $BaZrO_3$, while the activation energy of the proton conductivity was argued to be somewhat higher than that of Y-doped $BaZrO_3$. However, these parameters were extracted by curve-fitting a defect chemical model to the total conductivity, which is often overshadowed by the grain boundary

Centre for Materials Science and Nanotechnology, Department of Chemistry, University of Oslo, FERMiO, Gaustadalléen 21, 0349 Oslo, Norway. E-mail: t.s.bjorheim@kjemi.uio.no

contribution in the temperature interval investigated (550–700 °C), and may therefore not represent the true bulk properties of $BaZrO_3$.

In this contribution, we therefore assess the efficiency of the alkali metals (M = Na, K, Rb and Cs) as A-site acceptor dopants in $BaZrO_3$ from first principles calculations. We determine their tendency for proton and oxygen vacancy trapping, and evaluate the relevant minimum energy pathways for the proton around the dopants, thus addressing the dopant effect on both the proton conductivity and hydration thermodynamics. Further, the dopants' effect on the chemical expansion properties of $BaZrO_3$, and solubilities under typical synthesis conditions, are estimated.

2 Computational methodology

All first principles calculations were performed using Density Functional Theory (DFT) as implemented in the VASP code.[21,22] We applied the GGA-PBE exchange correlation functional[23] and the core potentials were treated by the projector augmented-wave (PAW) method.[24] The electronic wave functions were expanded using a set of plane waves with a constant plane-wave cut-off energy of 500 eV. The defect calculations were carried out using a 3 × 3 × 3 supercell (135 atoms) expansion of an optimised unit cell of cubic $BaZrO_3$. Electronic integration was performed using a 2 × 2 × 2 Monkhorst–Pack *k*-mesh for the supercell. Additional test calculations using 4 × 4 × 4 supercells (320 atoms) yielded similar results suggesting that the supercell expansions used were large enough in correspondence with other computational work on $BaZrO_3$.[25] Ionic and electronic relaxations were carried out using convergence criteria of 0.02 eV $Å^{-1}$ and 10^{-6} eV for self-consistency, respectively.

The defect formation energies were calculated by

$$\Delta_f E_{defect} = E^{tot}_{defect} - E^{tot}_{perfect} - \sum_i \Delta n_i \mu_i + q(\varepsilon_f + \Delta\varepsilon) \quad (2)$$

where E^{tot}_{defect} is the total energy of a supercell with a defect in charge state q, while $E^{tot}_{perfect}$ represents the total energy of the host supercell. Δn_i is the difference in the number of constituent atoms with chemical potential μ_i between the defect and perfect supercells. ε_f is the Fermi level while $\Delta\varepsilon$ is the shift in the core potentials of the perfect and defective supercell to correct shifts in the band edges due to the jellium background charge.

The enthalpies of hydration of $v_O^{\bullet\bullet}$ in undoped and A-site acceptor doped, *i.e.* $(M_{Ba}v_O)^{\bullet}$, were calculated according to

$$\Delta_{hydr}H_{v_O^{\bullet\bullet}} = 2E^{tot}_{OH_O^{\bullet}} - E^{tot}_{v_O^{\bullet\bullet}} - E^{tot}_{perfect} - E^{tot}_{H_2O} \quad (3)$$

$$\Delta_{hydr}H_{(M_{Ba}v_O)^{\bullet}} = 2E^{tot}_{(M_{Ba}OH_O)^{\times}} - E^{tot}_{(M_{Ba}v_O)^{\bullet}} - E^{tot}_{(M_{Ba}O_O)'} - E^{tot}_{H_2O} \quad (4)$$

where $E^{tot}_{OH_O^{\bullet}}$, $E^{tot}_{v_O^{\bullet\bullet}}$, $E^{tot}_{(M_{Ba}O_O)'}$, $E^{tot}_{(M_{Ba}OH_O)^{\times}}$ and $E^{tot}_{(M_{Ba}v_O)^{\bullet}}$ are the total energies of the defect supercell for the proton, oxygen vacancy, dopant, the proton–dopant and oxygen vacancy–dopant complexes, respectively. $E^{tot}_{perfect}$ is the total energy of the perfect supercell while $E^{tot}_{H_2O}$ is the total energy of a single water molecule as determined by DFT. Note that the total energies in eqn (3) and (4) have been adjusted with the potential alignment term in (2), although this is not explicitly included in the expressions. Proton migration pathways were evaluated for all dopants by the climbing image nudged elastic band (CI-NEB) method.[26,27]

Upon defect formation, the lattice may chemically expand or contract, which for a defect i can be expressed through the volumetric chemical expansion coefficient;

$$\varepsilon_i = \frac{1}{\delta}\left(\frac{V_i}{V_0} - 1\right) \quad (5)$$

where V_i and V_0 are the volumes of the defective and perfect supercell, respectively, while δ is the number of defects per formula unit.

Free energies of dopant dissolution have been evaluated under the assumption that the dopants dissolve from M_2O as binary oxides are commonly used as starting materials for the synthesis of $BaZrO_3$. We further assume ZrO_2 rich conditions as BaO evaporation is often encountered in the fabrication of $BaZrO_3$,[3,4,7] and that the acceptors are fully charge-compensated by oxygen vacancies

$$2Ba^{\times}_{Ba} + O^{\times}_O + M_2O(s) + 2ZrO_2(s) = 2M'_{Ba} + v_O^{\bullet\bullet} + 2BaZrO_3(s) \quad (6)$$

with the dissolution free energy determined by

$$\Delta_{diss}G = 2\Delta_f G_{M'_{Ba}} + \Delta_f G_{v_O^{\bullet\bullet}} \quad (7)$$

$\Delta_f G_{M'_{Ba}}$ and $\Delta_f G_{v_O^{\bullet\bullet}}$ are given by the following expressions, respectively

$$\Delta_f G_{M'_{Ba}} = E_{M'_{Ba}} - E_{perfect} + \mu_{BaZrO_3} - \mu_{ZrO_2} - \frac{1}{2}\mu_{M_2O} - \frac{1}{4}\mu_{O_2} - (\varepsilon_f + \Delta\varepsilon) \quad (8)$$

$$\Delta_f G_{v_O^{\bullet\bullet}} = E_{v_O^{\bullet\bullet}} - E_{perfect} + \frac{1}{2}\mu_{O_2} + 2(\varepsilon_f + \Delta\varepsilon) \quad (9)$$

The temperature dependency of the chemical potentials, μ_{M_2O}, μ_{ZrO_2} and μ_{BaZrO_3}, were taken from the HSC Chemistry 8.2.0 database.[28] For $v_O^{\bullet\bullet}$, we have also included vibrational contributions to the formation energy as reported in previous work.[2] For the dopants, the vibrational contributions were found to be negligible, and were therefore disregarded.

Further, the dopant solubilities have been estimated from the corresponding equilibrium constant

$$\exp\left(-\frac{\Delta_{diss}G}{RT}\right) = \left(\frac{[M'_{Ba}]}{[Ba^{\times}_{Ba}]}\right)^2 \frac{[v_O^{\bullet\bullet}]}{[O^{\times}_O]} \frac{a_{BaZrO_3(s)}{}^2}{a_{M_2O(s)}a_{ZrO_2(s)}{}^2} \quad (10)$$

with the following site restrictions imposed for the concentration of regular sites

$$[Ba^{\times}_{Ba}] = 1 - [M'_{Ba}] \quad (11)$$

$$[O^{\times}_O] = 3 - [v_O^{\bullet\bullet}] - [OH_O^{\bullet}] \quad (12)$$

where 1 and 3 (mole fractions) are the concentrations of Ba and O lattice sites, respectively.

3 Results and discussion

Defect configurations and complex formation

In the perfect $BaZrO_3$ structure, there is only a single distinct oxygen site with four symmetrically equivalent proton configurations.[10] A-site doping reduces the symmetry, resulting in two distinct proton configurations within the first coordination sphere of the dopant, one pointing towards the dopant and one away from it. In addition to these nearest-neighbour (N) positions, we have evaluated two distinct configurations within the second coordination sphere (NN) (Fig. 1).

The calculations reveal that for all A-site dopants, the proton is always most stable in configuration 1, *i.e.* closest to the acceptor dopant, while configurations 2–4 are less favourable (see Fig. 1). For instance for Rb, the relative energies of configurations 1–4 are 0, 0.12, 0.11 and 0.10 eV, respectively.

Fig. 2 compares the local atomic relaxations around a proton in its most stable configuration in undoped, B-site doped and A-site doped $BaZrO_3$. The lattice distortions are significantly larger in the B-site doped structure compared to that of the undoped system. The distortion extends far beyond the neighbouring atoms, causing a minor tilting of all surrounding octahedra. In the A-site doped system, on the other hand, the lattice distortion is minimal and barely affects the two neighbouring zirconium ions, which may indicate a local trapping effect for the A-site acceptor doped systems. Similar effects of lattice distortions on ionic conductivity have previously been observed for oxide ion transport in *e.g.* CeO_2, where the lattice strain caused by doping increases the activation energy of oxide ion mobility by as much as 0.3 eV.[29]

The effect of the dopant on the activation energy of proton and oxygen vacancy mobility can be estimated by evaluating the binding energies of the complexes formed between the acceptors and protons or oxygen vacancies $(M_{Ba}OH_O)^{\times}$ and $(M_{Ba}v_O)^{\bullet}$. This is determined by the formation energy differences between the complexes and isolated point defects;

$$E_{\text{bind}}(M_{Ba}OH_O)^{\times} = \Delta_f E_{(M_{Ba}OH_O)^{\times}} - \Delta_f E_{M'_{Ba}} - \Delta_f E_{OH^{\bullet}_O} \quad (13)$$

$$E_{\text{bind}}(M_{Ba}v_O)^{\bullet} = \Delta_f E_{(M_{Ba}v_O)^{\bullet}} - \Delta_f E_{M'_{Ba}} - \Delta_f E_{v^{\bullet\bullet}_O} \quad (14)$$

The calculated binding energies of $(M_{Ba}OH_O)^{\times}$ and $(M_{Ba}v_O)^{\bullet}$ are presented in Fig. 3(a) and (b), respectively, as a function of the ionic radius of all the A-site dopants studied. These energies are calculated by placing the positive defects either in the nearest (1–2) or next nearest (3–4) neighbour positions to the dopant, resulting in two separate binding energies for both $v^{\bullet\bullet}_O$ and $OH^{\bullet}_O$. Only the most stable nearest (N) and next nearest (NN) configurations to the dopant are used. The dashed vertical line represents the ionic radius of Ba^{2+}, for reference, while the horizontal dotted line denotes zero associations between the defects, *i.e.* $E_{\text{bind}} = 0$. Additional calculations taking the relative energy differences between defects placed near and far away from the acceptors in the same supercell yielded similar values. As the figure demonstrates, almost all binding energies are exothermic, reflecting that the formation of complexes is favoured over the isolated point defects. For the proton, the binding energies for the nearest neighbour (N) configuration show an almost linear trend with respect to the ionic radii of the dopant, becoming less exothermic with increasing size ranging from −0.33 to −0.10 eV for Na to Cs, respectively. These values are also of a similar magnitude to what has been reported for B-site doped $BaZrO_3$.[2,10,11,30] For the next nearest neighbour (NN) configurations on the other hand, the binding energies are virtually independent of the dopant. Furthermore, the binding energies for the oxygen vacancy, regardless of the coordination sphere (N or NN), generally become more exothermic with larger differences in the ionic radii between the dopant and the host (Ba) in correspondence with other computational work on B-site doped perovskites.[2,4,10,11,31] These binding energies are otherwise very weakly exothermic with a minimum value of −0.08 eV for Cs, and are thus significantly less negative than all

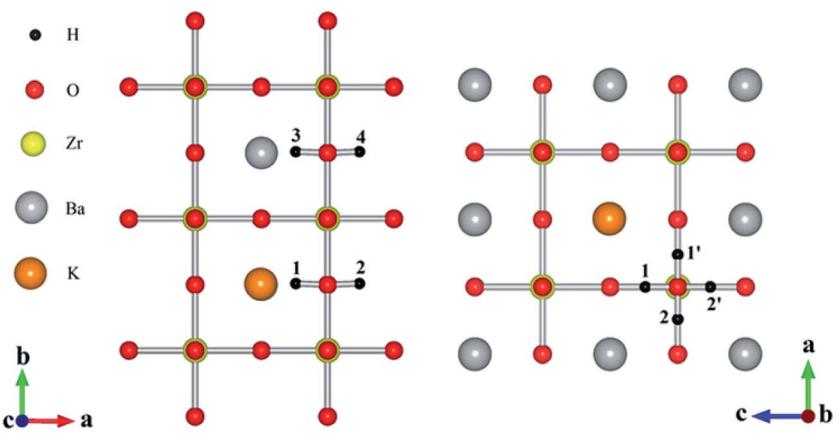

Fig. 1 The four proton configurations within the first (1 and 2) and second (3 and 4) coordination spheres considered in this work along two different projections. Note that configurations 1′ and 2′ are symmetrically equivalent to 1 and 2, respectively.

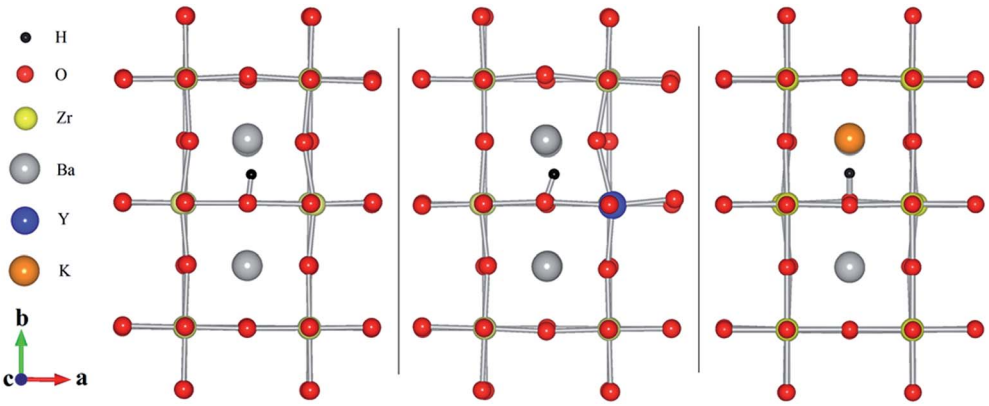

Fig. 2 Local atomic relaxations around the proton in undoped, B- and A-site doped $BaZrO_3$ (nearest neighbour configuration). B-site doping causes the most significant lattice distortions, while A-site doping results in less distortion than in undoped $BaZrO_3$. Note that Y and K have here been chosen as B- and A-site dopants, respectively, and the relaxations are similar for the other dopants.

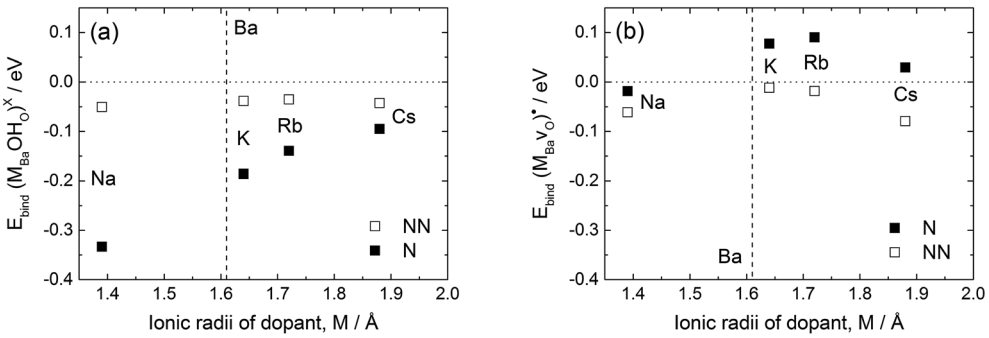

Fig. 3 (a) Calculated binding energies for the proton for A-site doped $BaZrO_3$as a function of the ionic radius of the dopant, M, and (b) the corresponding binding energies for the oxygen vacancy. These consider the most stable nearest (N) and next nearest configurations (NN) to the dopant. The vertical line denotes the ionic radius for Ba^{2+} for reference, while the horizontal line represents zero associations.

work on the B-site doped counterparts, which typically display values between −0.3 and −0.5 eV.[2,10]

Proton migration

To address the influence of the A-site dopants on proton mobility, minimum energy pathways for the rotation (R) and transport (T) of the proton for all dopants investigated have been mapped out. Similar proton migration pathways for Y-doped $BaZrO_3$ have also been included for comparison. All pathways considered are shown in Fig. 4 along with the corresponding energy profiles. While R1 and R2 refer to 90° rotations of the proton in the first and second coordination sphere of the dopant, respectively, T1 represents proton transport (migration) between two symmetrically equivalent sites in the nearest neighbour position. T2 and T3, on the other hand, involve proton transport further away from the dopant where in the case of T2, the proton moves from the first to the second coordination sphere of the dopant. As the results in Fig. 4 demonstrate, the highest proton migration energy barrier for the A-site dopants is associated with the rotation away from the dopant in the nearest neighbour configuration, and the barrier decreases with increasing size of the A-site cation, ranging from 0.24 to 0.56 eV for Cs to Na, respectively. The energy barriers for all other migration pathways are otherwise of a similar magnitude (~0.15–0.25 eV) being comparable to that of undoped $BaZrO_3$ [11] thus indicating that A-site acceptor dopants only act as local proton traps. This is in clear contrast to that of B-site dopants where the highest energy barrier involves a rotation away from the dopant in the next nearest neighbour (*cf.* Y in Fig. 4). Also, the highest migration energy barriers for all the alkali metals, except that of Na (R1), are either similar to or even lower than the highest corresponding barrier for Y-doped $BaZrO_3$ (R2), where the latter is 0.3 eV. Ultimately, this indicates that alkali metals as A-site acceptor dopants may improve the proton conductivity compared to that of Y-doped $BaZrO_3$.

Hydration thermodynamics

Fig. 5 presents the calculated hydration enthalpies for all the A-site dopants studied as a function of the ionic radius of the dopant. The horizontal dotted line indicates the hydration enthalpy for 10 mol% Y-doped and undoped $BaZrO_3$ determined experimentally.[3,32] The hydration enthalpies have been calculated by considering the most stable proton and oxygen vacancy positions. The enthalpies become increasingly negative

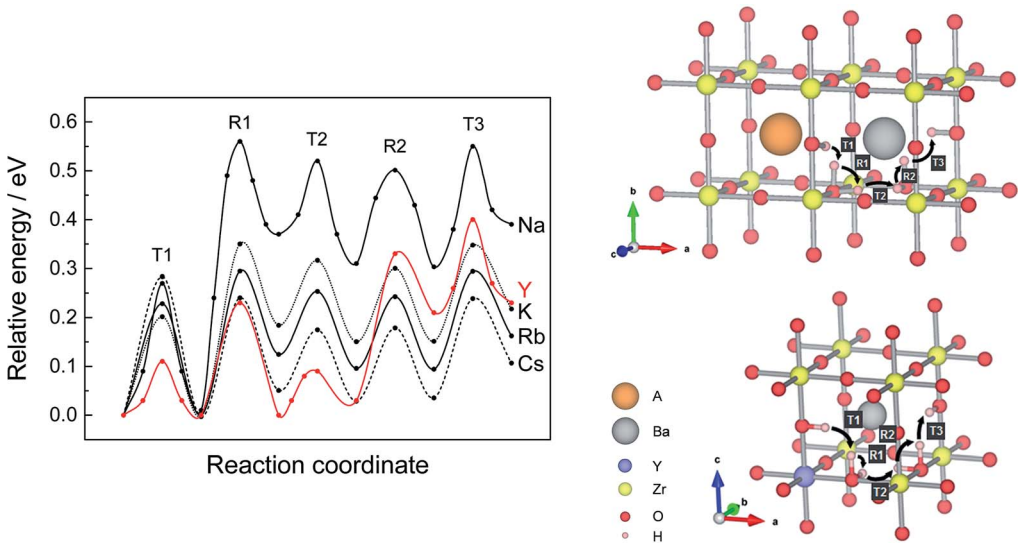

Fig. 4 NEB proton migration pathways and associated energy barriers for all A-site dopants considered (top structure) along with Y-doped $BaZrO_3$ (bottom structure) for comparison. The calculated points have been fitted to a modified Bézier curve to serve as a guide to the eye.

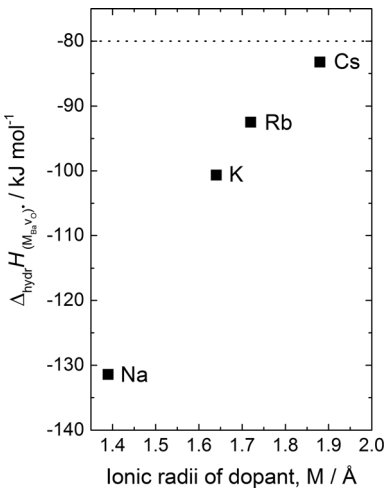

Fig. 5 Calculated hydration enthalpies of A-site doped $BaZrO_3$ as a function of the ionic radius of the dopant (M = Na, K, Rb and Cs). The dashed horizontal line represents experimentally determined hydration enthalpies for undoped and 10 mol% Y-doped $BaZrO_3$.[3,32]

with decreasing ionic radius, ranging from −83 kJ mol^{-1} to −131 kJ mol^{-1} for Cs and Na, respectively. These values are all consistently more negative than those of undoped and Y-doped $BaZrO_3$, suggesting that A-site doping may thermodynamically stabilise the protons to higher temperatures. This is also in agreement with experimental work on K-doped $BaZrO_3$ by Sherafat *et al.*[20] where the hydration enthalpy was determined to be −90 kJ mol^{-1}. Interestingly, the more negative hydration enthalpies actually stem from an instability of the oxygen vacancies compared to in *e.g.* Y-doped $BaZrO_3$, which makes them easily hydrate according to (1).

Chemical expansion

Chemical and thermal compatibility between the different components in a fuel cell or an electrolyser is essential to avoid cracking or delamination upon thermal cycling and hydration/dehydration. Y-doped $BaZrO_3$ exhibits a rather large chemical expansion upon hydration,[33] and a further enhancement of this expansion should be avoided when choosing alternative acceptor dopants.

The chemical expansion coefficients of $OH_O^{\bullet}$ and $v_O^{\bullet\bullet}$ in the A-site acceptor doped systems have been calculated from their most stable configurations. Since the dopant concentration can be assumed frozen in at lower temperatures, the cell with a single isolated acceptor dopant is taken as the perfect reference (*i.e.* V_0 in (5)). From $\varepsilon_{OH_O^{\bullet}}$ and $\varepsilon_{v_O^{\bullet\bullet}}$, the volumetric chemical expansion upon hydration (per mole of $v_O^{\bullet\bullet}$) is given by

$$\varepsilon_{hydr} = 2\varepsilon_{OH_O^{\bullet}} - \varepsilon_{v_O^{\bullet\bullet}} \quad (15)$$

As shown in Table 1, the formation volume is negative for both defect complexes, with the oxygen vacancy formation leading to the largest contraction of the cell, similar to what is

Table 1 Formation volumes of $OH_O^{\bullet}$ and $v_O^{\bullet\bullet}$, and the corresponding chemical expansion of hydration (ε_{hydr}) for A-site acceptor doped $BaZrO_3$, compared with similar values for undoped and Y-doped $BaZrO_3$ taken from Bjørheim *et al.*[2]

	$\Delta_f V_{(M_{Ba}OH_O)^{\times}}$ / Å^3	$\Delta_f V_{(M_{Ba}V_O)^{\bullet}}$ / Å^3	ε_{hydr}
Na	−5.04	−18.5	0.111
K	−4.84	−18.2	0.112
Rb	−4.48	−18.2	0.121
Cs	−3.53	−17.6	0.138
Undoped[2]	−4.48	−18.1	0.122
Y[2]	−6.2	−21.9	0.125

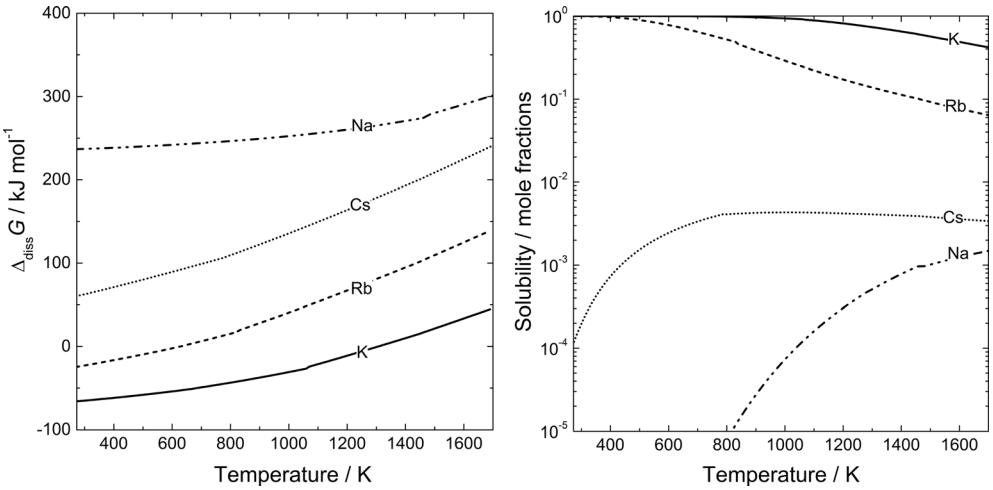

Fig. 6 Dissolution free energies and resulting equilibrium solubilities as a function of temperature according to (10) for the alkali metals in $BaZrO_3$.

previously reported for the undoped and B-site acceptor doped system.[2,34,35] These formation volumes lead to a slightly positive chemical expansion upon hydration for all four dopants, which increases with increasing dopant radii. Rb displays the smallest change in ε_{hydr} compared to the undoped system, which can be attributed to Rb having a similar ionic radius to Ba.

Dopant solubility

Our results so far suggest that the use of alkali metals as A-site acceptor dopants in $BaZrO_3$ is a promising strategy to increase its bulk proton conductivity, with the alkali metals displaying more exothermic hydration enthalpies and similar, if not better, proton migration energies compared to Y-doped $BaZrO_3$. However, the implementation of these dopants requires them to be readily soluble under normal experimental conditions. Fig. 6 presents the calculated dissolution free energies and solubilities of the A-site dopants calculated according to (10)–(12).

All dissolution energies increase with increasing temperature due to the negative entropy change associated with (6). There is in addition a noticeable effect of the dopant type on the dissolution energy, which generally decreases in the order Na < Cs < Rb < K. While Na exhibits dissolution energies in excess of 200 kJ mol^{-1}, that of K is exothermic throughout major parts of the temperature interval. This is reflected in the estimated solubilities in Fig. 6(b), with K, and to some extent Rb, reaching solubilities close to those of common B-site acceptor dopants such as Y. While Na is predicted to barely dissolve in $BaZrO_3$, Cs will only dissolve to a limited extent, at least when $BaZrO_3$ is in equilibrium with Cs_2O. One may however speculate whether for instance ion implantation, or a low temperature synthesis route where the dopant dissolves in combination with protons, could be used to promote Cs dissolution in $BaZrO_3$.

In summary, although Cs both shows the lowest proton binding energies and proton migration barriers (*cf.* Fig. 3(a) and 4), its predicted equilibrium solubility is most likely too low for practical applications. K and Rb, on the hand, are highly soluble and exhibit similar proton migration barriers to that of Y-doped $BaZrO_3$ rendering them as interesting candidates to increase the partial proton conductivity of $BaZrO_3$.

4 Conclusions

In this contribution, we have investigated the use of alkali metals as A-site acceptor dopants in $BaZrO_3$, as alternatives to common B-site dopants such as Y. First principles calculations reveal that all selected A-site dopants give rise to more negative hydration enthalpies compared to both undoped and Y-doped $BaZrO_3$. All dopants exhibit exothermic proton binding energies, which increase in the order Cs < Rb < K < Na, while the oxygen vacancy binding energies are significantly smaller. All relevant proton minimum energy pathways for the A-site dopants investigated have been mapped out and demonstrate that alkali metals only act as local proton traps where the largest barrier is associated with the rotation away from the dopant in the nearest neighbour configuration. Furthermore, the calculations reveal that the highest migration energy barrier for most of the alkali metals is comparable or even lower than that of Y. The calculated dopant dissolution energies increase in the order K < Rb < Cs < Na, and K and Rb are predicted to exhibit solubilities similar to those of *e.g.* Y, while that of Cs and especially Na will be limited. Although Cs, which displays the lowest proton migration energy barriers, would be the preferred A-site dopant in $BaZrO_3$ to maximise the proton mobility, the higher equilibrium solubility of Rb renders it a more optimum overall candidate. Not only does Rb exhibit similar proton migration energy barriers to that of Y-doped $BaZrO_3$, but it also displays a hydration enthalpy that is almost 30% more negative than Y-doped $BaZrO_3$, and would therefore stabilise protonic defects to higher temperatures. Lastly, all dopants show similar chemical expansion properties upon hydration to those of *e.g.* Y-doped $BaZrO_3$ and are therefore predicted to be thermally compatible with anodes/cathodes developed for Y-doped $BaZrO_3$.

Acknowledgements

The authors gratefully acknowledge the Research Council of Norway (RCN), project "HydraThermPro" (project 214252) and the BIGCCS Centre (project 193816) under the Norwegian research program Centres for Environment-Friendly Energy Research (FME), and the Centre for Materials Science and Nanotechnology, for financial support. The calculations were performed on resources provided by UNINETT Sigma2 – the National Infrastructure for High Performance Computing and Data Storage in Norway.

References

1 E. Fabbri, D. Pergolesi and E. Traversa, *Chem. Soc. Rev.*, 2010, **39**, 4355–4369.
2 T. S. Bjørheim, E. A. Kotomin and J. Maier, *J. Mater. Chem. A*, 2015, **3**, 7639–7648.
3 K. D. Kreuer, *Annu. Rev. Mater. Res.*, 2003, **33**, 333–359.
4 A. Løken, T. S. Bjørheim and R. Haugsrud, *J. Mater. Chem. A*, 2015, **3**, 23289–23298.
5 T. Norby, in *Perovskite Oxide for Solid Oxide Fuel Cells*, ed. T. Ishahara, 2009.
6 C. Kjølseth, H. Fjeld, Ø. Prytz, P. I. Dahl, C. Estournès, R. Haugsrud and T. Norby, *Solid State Ionics*, 2010, **181**, 268–275.
7 S. M. Haile, G. Staneff and K. H. Ryu, *J. Mater. Sci.*, 2001, **36**, 1149–1160.
8 A. K. Azad, C. Savaniu, S. Tao, S. Duval, P. Holtappels, R. M. Ibberson and J. T. S. Irvine, *J. Mater. Chem.*, 2008, **18**, 3414–3418.
9 Y. Yamazaki, F. Blanc, Y. Okuyama, L. Buannic, J. C. Lucio-Vega, C. P. Grey and S. M. Haile, *Nat. Mater.*, 2013, **12**, 647–651.
10 M. E. Björketun, P. G. Sundell and G. Wahnstrom, *Faraday Discuss.*, 2007, **134**, 247–265.
11 M. E. Björketun, P. G. Sundell and G. Wahnström, *Phys. Rev. B: Condens. Matter Mater. Phys.*, 2007, **76**, 054307.
12 M. Karlsson, D. Engberg, M. E. Björketun, A. Matic, G. Wahnström, P. G. Sundell, P. Berastegui, I. Ahmed, P. Falus, B. Farago, L. Börjesson and S. Eriksson, *Chem. Mater.*, 2010, **22**, 740–742.
13 A. Cammarata, P. Ordejón, A. Emanuele and D. Duca, *Chem.–Asian J.*, 2012, **7**, 1827–1837.
14 H. Fujii, Y. Katayama, T. Shimura and H. Iwahara, *J. Electroceram.*, 1998, **2**, 119–125.
15 C. K. Vigen, T. S. Bjørheim and R. Haugsrud, *Int. J. Hydrogen Energy*, 2012, **37**, 7983–7994.
16 M. S. Islam and R. A. Davies, *J. Mater. Chem.*, 2004, **14**, 86–93.
17 M. Huse, T. Norby and R. Haugsrud, *Int. J. Hydrogen Energy*, 2012, **37**, 8004–8016.
18 A. S. Patnaik and A. V. Virkar, *J. Electrochem. Soc.*, 2006, **153**, A1397–A1405.
19 X. Xu, S. Tao and J. T. S. Irvine, *J. Solid State Chem.*, 2010, **183**, 93–98.
20 Z. Sherafat, M. H. Paydar, I. Antunes, N. Nasani, A. D. Brandão and D. P. Fagg, *Electrochim. Acta*, 2015, **165**, 443–449.
21 G. Kresse and J. Furthmüller, *Phys. Rev. B: Condens. Matter Mater. Phys.*, 1996, **54**, 11169–11186.
22 G. Kresse and D. Joubert, *Phys. Rev. B: Condens. Matter Mater. Phys.*, 1999, **59**, 1758–1775.
23 J. P. Perdew, K. Burke and M. Ernzerhof, *Phys. Rev. Lett.*, 1996, **77**, 3865–3868.
24 P. E. Blöchl, *Phys. Rev. B: Condens. Matter Mater. Phys.*, 1994, **50**, 17953–17979.
25 A. Lindman, P. Erhart and G. Wahnström, *Phys. Rev. B: Condens. Matter Mater. Phys.*, 2015, **91**, 245114.
26 G. Henkelman, B. P. Uberuaga and H. Jónsson, *J. Chem. Phys.*, 2000, **113**, 9901–9904.
27 D. Sheppard, R. Terrell and G. Henkelman, *J. Chem. Phys.*, 2008, **128**, 134106.
28 *HSC Chemistry 8.2.0*, Outetec Technologies, 2015.
29 J. Faber, C. Geoffroy, A. Roux, A. Sylvestre and P. Abélard, *Appl. Phys. A: Solids Surf.*, 1989, **49**, 225–232.
30 S. J. Stokes and M. S. Islam, *J. Mater. Chem.*, 2010, **20**, 6258–6264.
31 E. Bévillon, J. Hermet, G. Dezanneau and G. Geneste, *J. Mater. Chem. A*, 2014, **2**, 460–471.
32 C. Kjølseth, L.-Y. Wang, R. Haugsrud and T. Norby, *Solid State Ionics*, 2010, **181**, 1740–1745.
33 A. K. E. Andersson, S. M. Selbach, C. S. Knee and T. Grande, *J. Am. Ceram. Soc.*, 2014, **97**, 2654–2661.
34 E. Jedvik, A. Lindman, M. Þ. Benediktsson and G. Wahnström, *Solid State Ionics*, 2015, **275**, 2–8.
35 T. S. Bjørheim, A. Løken and R. Haugsrud, *J. Mater. Chem. A*, 2016, **4**, 5917–5924.

4 Discussion

In the manuscripts, which constitute the main part of this thesis, several aspects related to the defect chemical and mass storage properties at heterogeneous interfaces where at least one of the components is a proton conducting oxide have been covered. In the following, some aspects and results that have not been presented or thoroughly addressed in the manuscripts are discussed.

4.1 Defect segregation to interfaces

In undoped semiconductors, the Fermi level, which represents the chemical potential of electrons, lies at or close to the middle of the band gap. The valence band and conduction band represent the standard chemical potential of electrons and electron holes. Upon doping with acceptors (*p*-type) or donors (*n*-type), the Fermi level shifts towards the valence or conduction band, respectively, by an amount that corresponds to the configurational term, $kT\ln\left(N_{V(C)}/N_{A(D)}\right)$, as shown in **Fig. 3a**. Joining acceptor and donor-doped semiconductors results in a *p*-*n* junction, where the difference in the chemical potential of electrons on either side of the junction constitutes the driving force for electron holes and electrons to cross the interface and recombine with each other. Consequently, a depletion layer is formed at the junction. The concentration of electrons and holes, and the spatial extent of the depletion layer, are governed by Poisson's equation and the difference in Fermi level. **Fig. 3b** shows a schematic representation of the band diagram of a *p*-*n* junction at equilibrium, where the Fermi level is constant. Although this representation is widely used among physicists as a convention,[63] it may be misleading as it indicates that the vacuum level is not constant. **Fig. 3c** shows a different representation where the vacuum level and band edges are constant while the Fermi level is not. Indeed, the difference in Fermi level on the two sides of the junction may be confusing as it indicates that even at equilibrium, there is an energy gain if electrons are transferred to the *p*-side. In this context, it should be noted that the property that governs the charge carrier distribution is the electrochemical potential rather than the Fermi level (which represents the chemical potential of the electrons). The electrostatic potential on the two sides of the interface is shifted with respect to each other, as shown in **Fig. 3c** (note that the electrostatic potential in **Fig. 3c** is arbitrarily placed in the band gap; the important message here is the relative position of the electrostatic potential in the two phases rather than its absolute position), which results

in a constant electrochemical potential across the interface. The electrochemical potential of electrons (ε_i) is unaffected by the electrostatic potential (or doping) and remains constant.

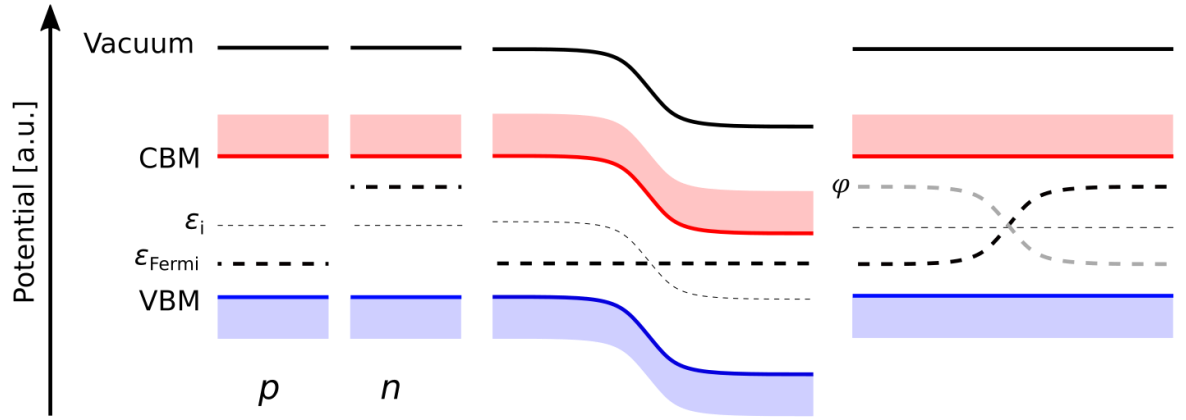

Fig. 3. Band diagram of acceptor (p) and donor (n) doped semiconductors prior to (a) and after (b) forming a p-n junction. (c) is a different representation of (b). VBM, CBM, ε_{Fermi}, ε_i and φ denote the valence band maximum, conduction band minimum, Fermi level, electrochemical potential of electrons and electrostatic potential. The electrostatic potential is arbitrarily placed.

Despite the differences in their chemistry, the situation at interfaces between ionic solids is similar to that of p-n junctions, except that the electronic levels are replaced with ionic levels. In line with the situation in semiconductors, the standard ionic levels, which reflect the formation energy of defects (and hence chemical bond strength), are constant in the bulk. **Fig. 4** illustrates the ionic band diagram of a homojunction/bulk, a surface and a heterointerface. In fact, one may also replace the ionic levels with ionic bands as the defect formation energy may show some dependence on the concentration due to defect-defect interactions, and thus broader energy states. As with semiconductors, homogeneous doping can be utilized to pin the ionic "Fermi" level (*i.e.* $\mu_{O^{2-}}$), which thus allows tuning the properties of homo- and heterointerfaces, while the standard levels remain constant. The difference in $\mu_{O^{2-}}$ across the interface provides the driving force for segregation of oxide ions/$v_O^{\bullet\bullet}$ from one side to the other, which in turn leads to the formation of space-charge layers that create the basis for nanoionics.

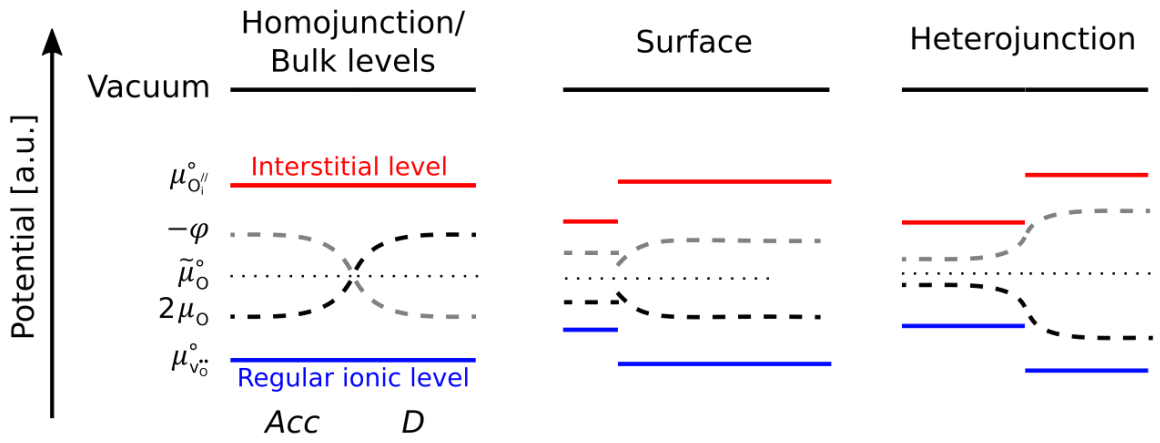

Fig. 4. Schematic of the ionic levels and electrostatic potential at a junction between an acceptor- and a donor-doped ion conductor (left), surface (middle) and acceptor-doped heterojunction. In all cases, it is assumed that only two defects are presented in the material(s); oxygen vacancies and oxygen interstitials. $-\mu_{V_O^{\cdot\cdot}}$, $\mu_{O^{2-}}$, $\tilde{\mu}_{O^{2-}}$, φ and $\mu^{\circ}_{O_i''}$ denote the standard chemical potential of lattice O^{2-}, and chemical and electrochemical potential of O^{2-}, electrostatic potential and standard chemical potential of oxygen interstitials. The electrostatic potential is arbitrarily placed.

Near heterogeneous interfaces and other higher dimensional defects such as surfaces, dislocations and grain boundaries where the chemistry of the lattice may change, the ionic energy levels may differ from in bulk. The shift in ionic levels at surfaces and grain boundaries may be viewed as the ionic counterpart of *e.g.* electronic surface states in semiconductors. **Fig. 4b** shows the ionic level diagram where the $\tilde{\mu}_{O^{2-}}$ and $\mu^{\circ}_{O^{2-}}$ are constant across the surface while $\mu_{O^{2-}}$ is not. In this case, the difference in electrostatic potential causes segregation of O^{2-} ions from the surface to the sub-surface and bulk layers, which in turn results in bending the electrostatic potential and $\mu_{O^{2-}}$. The situation at a heterointerface (**Fig. 4c**) is similar to that at the surface. In both cases, $\mu^{\circ}_{O^{2-}}$ may not be constant at the interface, as presented in **Fig. 4**, such that $\Delta\mu^{\circ}_{O^{2-}}$ either strengthens or wakens the driving force for defect segregation.

In practice, there are two factors that affect the bonding in solids and shift the levels as depicted in **Fig. 4b** and **c**; the first is change in coordination, for instance due to a change in the number of nearest neighbors as a result of structural aperiodicities (*e.g.* grain boundaries and surfaces), and/or due to different nearest neighbor type (*i.e.* second phase). The second factor is related to change in interatomic distances, *i.e.* strain, and mainly stems from the lattice mismatch of the joining phases. Strain affects both the band edges, which enter in the calculation of defect affinities, and the defect formation energies. From molecular orbital (MO) theory it can be deduced that compressive strain causes higher overlap of atomic orbitals, and thus lowers the

energy of the binding molecular orbitals while increasing the energy of the antibonding MO – the opposite applies to tensile strain. As such, compressive and tensile strain, respectively, increases and decreases the work function of the oxide. The effect of strain on the defect formation energy can be deduced from the defect formation volume; a defect that moderates the strain is further stabilized compared to bulk. Thus, compressive strain stabilizes defects that exhibit negative formation volume (such as $v_O^{\bullet\bullet}$, $\Delta V^f = -18$ Å^3), while tensile strain stabilizes defects that exhibit positive formation volume. In addition, the "shape" of a defect may also affect the change in formation energy that arises from strain. In Manuscript I and II, we showed that a compressive or tensile strain of 3 % in $BaZrO_3$ alters the $v_O^{\bullet\bullet}$ formation energy by −0.42 or 0.20 eV, respectively. Including the shift in band edges, the change in the formation energy of $v_O^{\bullet\bullet}$ becomes −0.79 or 0.44 eV, respectively, which is significant considering that the energy of $v_O^{\bullet\bullet}$ segregation from $SrTiO_3$ to $BaZrO_3$ is −0.64 eV, for the strain free interface.

The effect of strain on the formation energy of the various defects presented in a material may be different; consequently, the relative stability of the defects is affected. For instance in BaZrO3, a compressive strain of 1 % stabilizes the $v_O^{\bullet\bullet}$ by 0.09 eV and destabilizes $OH_O^{\bullet}$ by 0.11, while a tensile strain destabilizes the $v_O^{\bullet\bullet}$ by 0.10 eV and stabilizes $OH_O^{\bullet}$ by 0.09 eV. As such, the hydration enthalpy of a 1 % compressively strained $BaZrO_3$ increases (becomes less negative) by 0.31 eV to a total of −0.50 eV. A tensile strain of 1 % lowers the hydration enthalpy to −1.10 eV. Thus, in strained nanoparticles, thin films or near interfaces, the extent of hydration and concentration of defects may differ significantly from in bulk, not only due to space-charge effects but also due difference in the reaction thermodynamics.

The presence of higher dimensional defects not only affects the electronic contribution to formation energy on an absolute scale, but also the vibrational entropy, which is part of the standard chemical potential of a defect. In Manuscript I, II and IV, change in the vibrational modes near the interface was neglected and only the bulk-to-bulk segregation entropy was considered. Manuscript III shows that the change in the entropy of defect segregation to boundary planes may be significant. The calculated segregation entropy, $\Delta S_{\mathrm{seg}}^{\mathrm{vib}}$, for the surface $v_O^{\bullet\bullet}$ in $BaZrO_3$ is 0.53 J/mol K, which significantly stabilizes the $v_O^{\bullet\bullet}$ at higher temperatures. On the other hand, segregation of $v_O^{\bullet\bullet}$ to the grain boundaries in $BaZrO_3$ is considerably lower, 19 J/molK [64]. These values indicate that more open structures and larger absolute formation volumes result in higher defect formation entropy. It is also worth noting that these values apply for segregation to the boundary planes, which for the interfaces considered in this thesis is

unfavorable. In sub-surface planes (*i.e.* within the space charge layer) where the structure can be considered as part of the bulk, it is likely that the vibrational entropy difference is minute (compared to bulk), and in the absence of strain, similar to the bulk value. Thus, the contribution of vibrational entropy change of interface defects to the total free energy may be small (at least at lower temperatures), justifying it being neglected in this thesis.

4.2 Band electrons vs. polarons

In Manuscript II, the electrons in donor-doped $SrTiO_3$ have been assumed to be localised on the titanium atoms as small polarons although electrical conductivity measurements suggest the electrons to be delocalised.[65] Since the calculated reduction enthalpies are very close in both cases, the predicted defect concentrations in bulk are similar. However, near the interface, such an assumption may cause some differences in defect concentration profiles as polarons are subject to site restrictions. In addition, the limited number of available sites causes a high potential drop within $SrTiO_3$. On the other hand, in the case of delocalised electrons, such restrictions are not applicable as the number of available states is given by the density of states. Furthermore, a negligibly small potential is needed to pose a change in the electron concentration near the interface, which in turn results in higher space-charge potential in $BaZrO_3$ and thus more depletion of defects as **Fig. 5** and **Fig. 6** show. At 600 K, the depleted charge increases from 0.38 to 0.45 C/m^2. Consequently, also other properties, such as mass storage, electrical conductivity and capacitance, are affected.

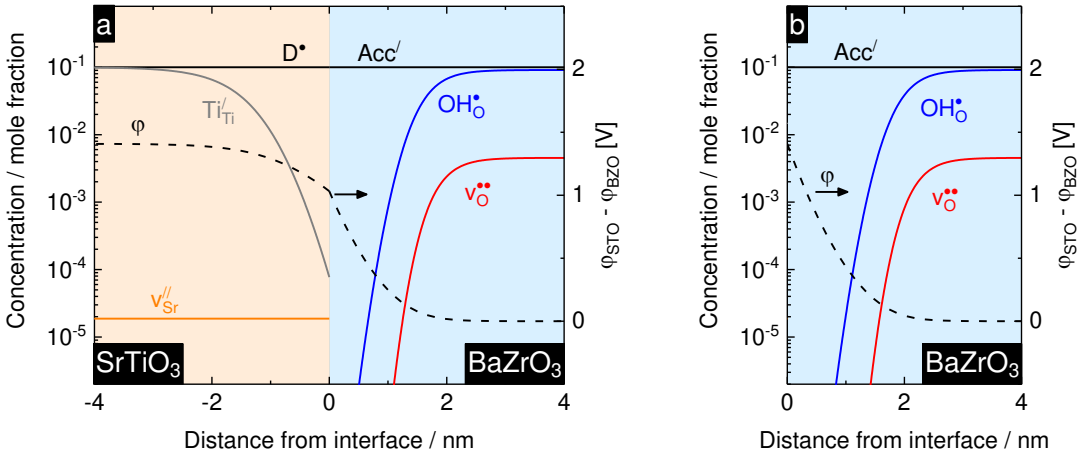

Fig. 5. The defect concentration profiles near the interface between donor-doped $SrTiO_3$ and acceptor-doped $BaZrO_3$. The electrons in $SrTiO_3$ are treated as polarons (a) or band electrons (b).

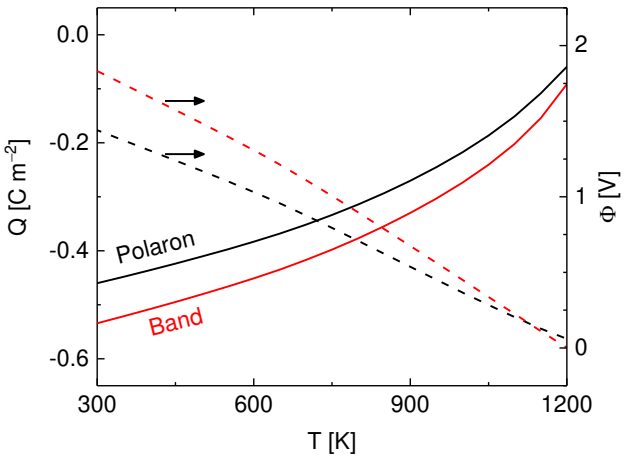

Fig. 6. The temperature dependency of the electrostatic potential and charge at the interface between donor-doped $SrTiO_3$ and acceptor-doped $BaZrO_3$, where the electrons are assumed to be localised or delocalised.

4.3 The phase boundary core

So far, segregation of defects to the phase boundary core/plane has not been addressed, as only epitaxial interfaces between materials exhibiting the same crystal structure have been considered. At such interfaces, segregation to the boundary core is weakly favoured or not favoured at all (even if strain is included). In the case of non-epitaxial interfaces, or epitaxial interfaces between materials exhibiting different crystal structure, segregation to the boundary core may be strongly favoured and thus affect the defect concentration profiles across the interface. In for instance epitaxial $BaZrO_3$ on MgO, segregation of $OH_O^{\bullet}$ to unterminated oxide ions at the interface (within MgO) is reported to be strongly favoured, with a segregation energy of −1.4 eV.[34] At non-epitaxial interfaces between for instance perovskites, the segregation energies of defects are expected to be similar to those of corresponding grain boundaries, which are typically around −0.8 eV for $OH_O^{\bullet}$ and somewhat similar for $v_O^{\bullet\bullet}$. To assess the significance of defect segregation to the core, the concentration profiles near the interface between acceptor-doped, undoped or donor-doped $SrTiO_3$ and acceptor-doped $BaZrO_3$ have been calculated assuming core segregation energies (relative to bulk $BaZrO_3$) of −0.80 and −0.65 eV for $OH_O^{\bullet}$ and $v_O^{\bullet\bullet}$, respectively. The resulting profiles are presented in Fig. 7, which shows that $OH_O^{\bullet}$ dominate the phase boundary core in systems with acceptor-doped or undoped $SrTiO_3$. Upon inclusion of core segregation, the charge goes from 0.30 to −0.08 C/m^2, *i.e.* from enrichment to depletion in acceptor-doped $BaZrO_3$, while being weakly affected in $SrTiO_3$ (−0.30 vs. −0.38

C/m^2) due to the high energy required to deplete it further. In the interface system with undoped $SrTiO_3$, $OH_O^{\bullet}$ segregation to the core is mainly charge compensated by depletion of $OH_O^{\bullet}$ and $v_O^{\bullet\bullet}$ in $BaZrO_3$. On the other hand, in the donor-doped system, $OH_O^{\bullet}$ to the core is limited as a result of the high electrostatic potential there. In conclusion, defect segregation to the phase boundary core occurs, and affects the interface defect structure only in situations where the electrostatic potential – that results from such segregation – is close to or larger than the built in potential that arises from segregation of defects across the phase boundary.

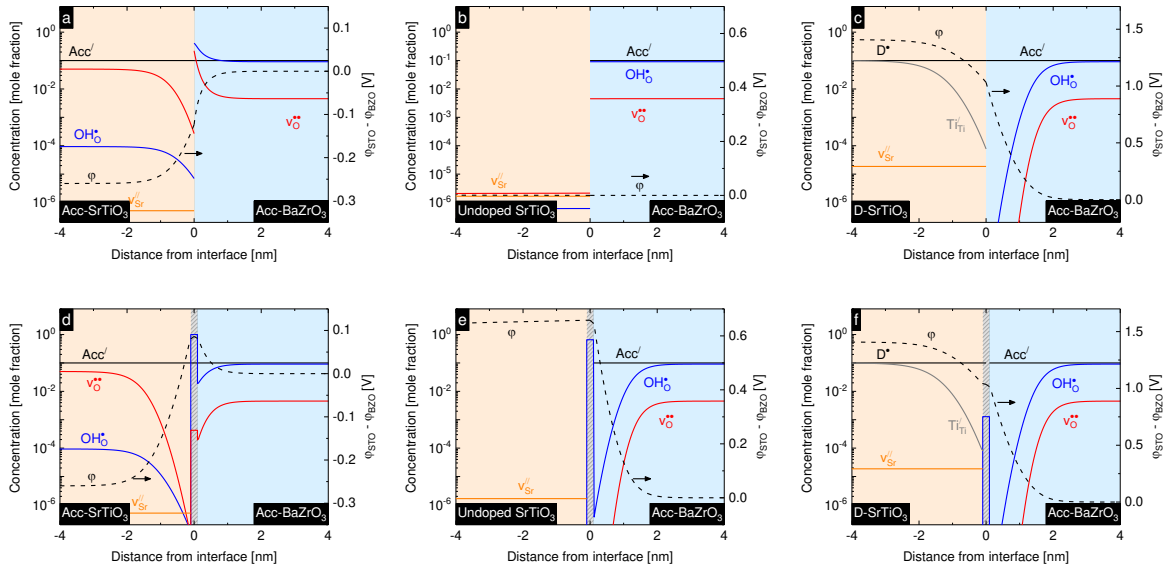

Fig. 7. The defect structure of interfaces between acceptor-doped, undoped or donor-doped $SrTiO_3$ and acceptor-doped $BaZrO_3$ with (a-c) and without (d-f) inclusion of defect segregation to the phase boundary core.

4.4 Tailoring nanoionic effects in oxides

In Manuscript I, II and IV, we showed that interfaces between materials exhibiting different electronic and/or defect structures may result in significant heterogeneous doping effects, causing enrichment or depletion of defects near the interface. The type and amount of accumulated (depleted) defects depend on the dominating electroneutrality in the bulk and the electrostatic potential across the interface. The latter is related to the segregation energy, which can be separated into two terms; the difference in the defect's standard formation energy on an absolute scale in the two materials and a configurational term that accounts for differences in defect concentrations. The first term is thus fixed by the choice of materials and may, to some extent, be tailored through substitution of lattice ions which may affect the defect formation

energy and the band structure of the material. The latter, *i.e*. the configurational term, may on the other hand be significantly affected by changing the concentration of defects in the bulk through for instance homogeneous doping (*i.e*. substitution of lattice ions with higher or lower valent ones). The electrostatic potential is also dependent on external parameters such as temperature and atmosphere, which affect both the formation energy and (relative) concentration of defects in the bulk oxide, and thereby the interface defect chemistry.

The effect of homogeneous doping on the interface defect chemistry was addressed in Manuscript II, demonstrating that for instance replacing the acceptor dopant in $SrTiO_3$ by a donor increased the electrostatic potential across the interface between the $SrTiO_3$ and acceptor-doped $BaZrO_3$ by 3 V. We suggested that such a large potential may be beneficial for charge storage and/or separation of charge compensating defects and concluded that homogeneous doping may even cause an inversion of electrostatic potential across the interface. In particular potential inversion and separation of charge compensating defects can be utilised to enhance the ionic conductivity in thin films and nano-composites. For instance the segregation of protons from acceptor-doped $BaZrO_3$ to acceptor-doped $SrTiO_3$ is unfavourable due to higher affinity for protons in the former. Reducing the concentration of charge carriers in $SrTiO_3$ (by lowering the concentration of dopants) lowers the chemical potential, and thus results in inversion of the electrostatic potential and consequently segregation of $OH_O^{\bullet}/v_O^{\bullet\bullet}$ from $BaZrO_3$ to $SrTiO_3$. Effectively, this corresponds to separating the dopant and the charge compensating defects in the two materials, which potentially lead to enhanced ionic conductivity in ionic solids since the transport of charge carriers no longer is subject to association with the dopants (which typically lowers the mobility). In spite of this, we discuss the defect chemistry of – and transport along – interfaces between undoped $BaZrO_3$ and a number of oxides were the standard segregation energies of $v_O^{\bullet\bullet}$ and $OH_O^{\bullet}$ to $BaZrO_3$ vary from strongly negative to strongly positive. The considered oxides are 10 mol-% acceptor-doped $SrTiO_3$, ZrO_2, $BaZrO_3$, and CeO_2, in order of increasing segregation energy of $v_O^{\bullet\bullet}$ (**Table 1**). In wet, reducing conditions, these materials are mainly dominated by $v_O^{\bullet\bullet}$, $OH_O^{\bullet}$ and localized electrons as shown in **Fig. 8**. Except for (acceptor-doped) $BaZrO_3$, which is dominated by $OH_O^{\bullet}$ below 700 °C, all of these oxides are dominated by $v_O^{\bullet\bullet}$ as charge compensating defects in the considered temperature range. At higher temperatures, $SrTiO_3$ and CeO_2 are prone to reduction, which results in increased concentration of $v_O^{\bullet\bullet}$ that are charge compensated by localized electrons, *i.e*. Ti_{Ti}' or Ce_{Ce}', respectively.

Table 1. Defect segregation energies to undoped $BaZrO_3$.

	$E_{v_O^{\bullet\bullet}}^{seg}$	$E_{OH_O^{\bullet}}^{seg}$
$SrTiO_3$	−0.64	−0.56
ZrO_2	−0.34	−1.40
$BaZrO_3$	0.00	0.00
CeO_2	1.41	0.03

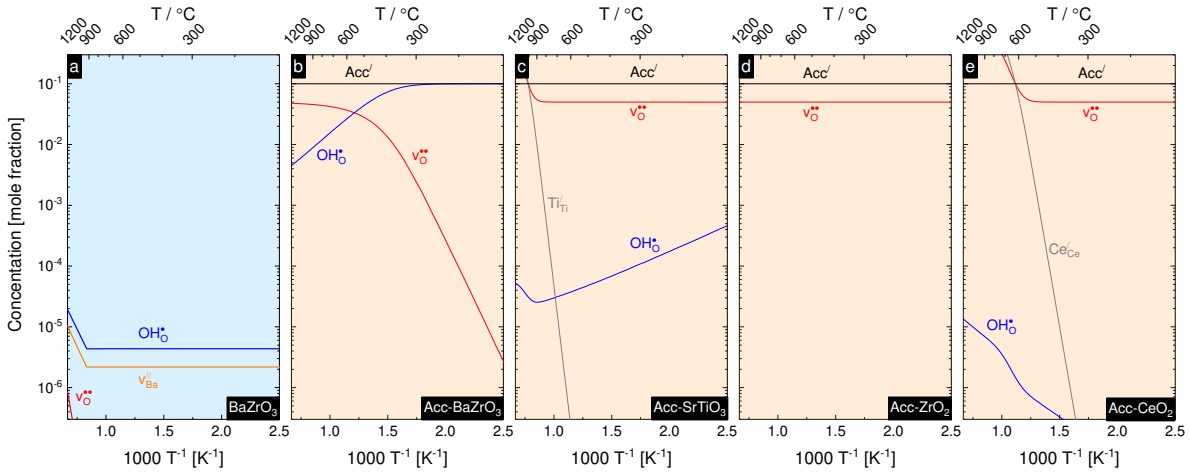

Fig. 8. Defect concentrations as a function of inverse temperature in wet, reducing atmosphere ($p_{H_2O} = 0.03$ atm and $p_{O_2} = 10^{-30}$ atm) in (a) undoped $BaZrO_3$ and 10 mole-% acceptor doped (b) $BaZrO_3$, (c) $SrTiO_3$, (d) ZrO_2 and (e) CeO_2. The concentration of cation vacancies and dopants is assumed frozen-in below 1200 K.

Fig. 9 shows examples of the electrostatic potential and concentration profiles as a function of distance from the interface between undoped $BaZrO_3$ and acceptor-doped $SrTiO_3$ and CeO_2 at 600 K. At this temperature Φ is strongly negative, favouring segregation of positively charged defects from $SrTiO_3$ to $BaZrO_3$, where the concentration of $OH_O^{\bullet}$ approaches unity at the interface. In the case of acceptor-doped CeO_2, Φ is weakly positive, 0.15 V, which causes a depletion of positively charged defects in $BaZrO_3$. The evolution of the electrostatic potential and accumulation (depletion) of charge near the interface in the range 300 – 1200 K are shown in **Fig. 10a** and **b**, respectively. Although Φ exhibits weak temperature dependence in this temperature range, the charge at the interface decreased by a factor 4 when $SrTiO_3$ is the second phase as a consequence of the thermal energy. In the case of CeO_2 as a second phase, Φ is initially positive and eventually changes sign above 900 K. Throughout this temperature range, the depleted (accumulated) charge is negligible.

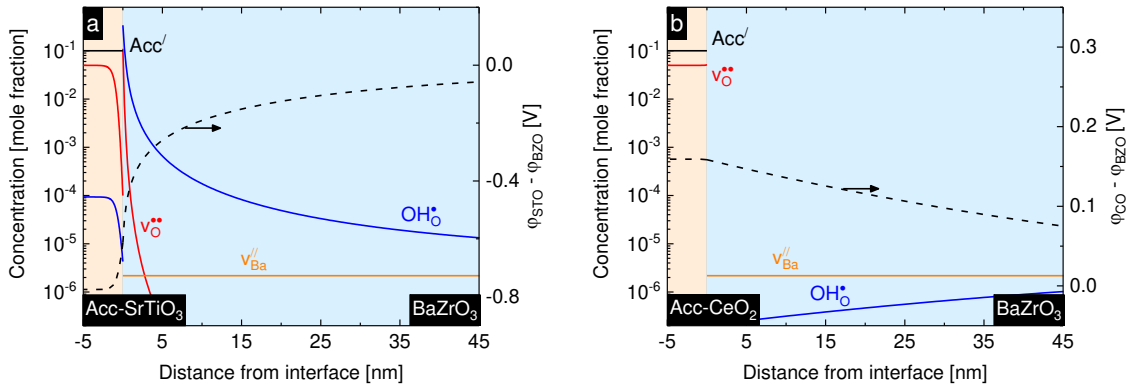

Fig. 9. The calculated defect concentration profiles across the interface between undoped $BaZrO_3$ and 10 mole-% acceptor-doped (a) $SrTiO_3$ and (b) CeO_2 at 600 K in wet, reducing atmosphere ($p_{H_2O} = 0.03$ atm and $p_{O_2} = 10^{-30}$ atm).

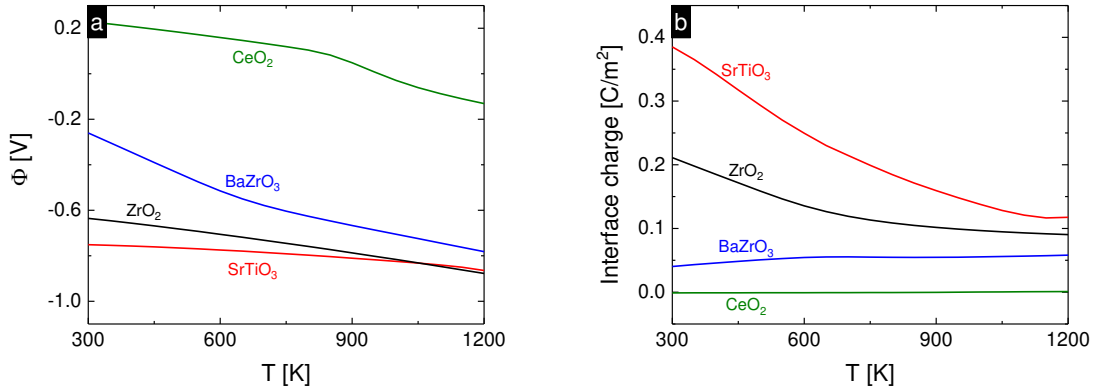

Fig. 10. The electrostatic potential across the interface between undoped $BaZrO_3$ and various 10 mole-% acceptor-doped oxides (a), and the charges transferred across the same interfaces (b) in wet, reducing atmosphere ($p_{H_2O} = 0.03$ atm and $p_{O_2} = 10^{-30}$ atm).

Across the interface between undoped and acceptor-doped $BaZrO_3$, the electrostatic potential is solely determined by the difference in chemical potential of $v_O^{\bullet\bullet}/OH_O^{\bullet}$ arising from the difference in configurational entropy. The latter is responsible for compliance with the requirement of constant dielectric function at the interface, and thus causes the concentration profiles of defects to be continuous there, as shown in **Fig. 11a**. Therefore, the equilibrium concentration of defects in undoped $BaZrO_3$ cannot exceed that in the acceptor-doped phase, even when the thickness of the latter is decreased below the screening length (see next section). However, in an interface system where defects in the second phase exhibit weakly favoured segregation to $BaZrO_3$, such the case is with ZrO_2, the situation changes significantly. As **Fig. 11b** shows, the $OH_O^{\bullet}$ concentration near the interface becomes one order of magnitude higher

compared to heterostructures with acceptor-doped $BaZrO_3$ as a second phase. Although Φ is similar when the second phase is acceptor-doped ZrO_2 or $SrTiO_3$, figure **Fig. 10** shows that ZrO_2 results in less charge enrichment in undoped $BaZrO_3$. This is a result of the lower dielectric constant of ZrO_2, which thus gives weaker screening, and hence lower total interface charge.

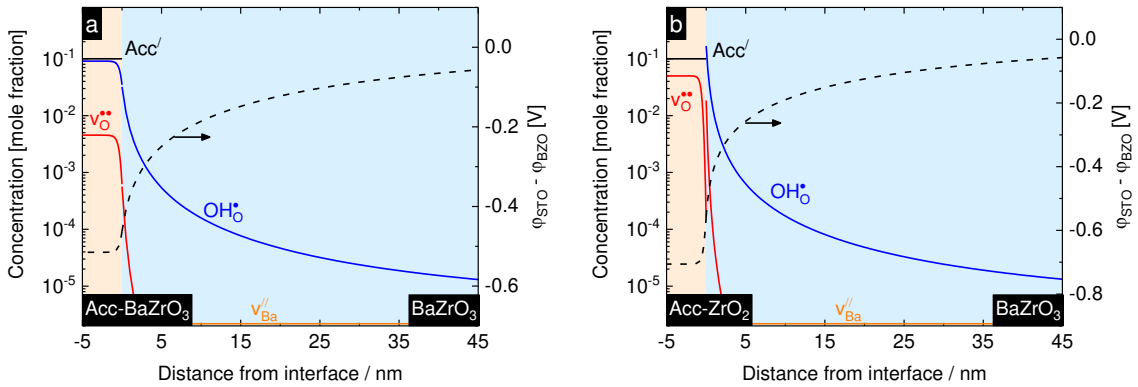

Fig. 11. The calculated defect concentration vs. distance from the interface between undoped $BaZrO_3$ and 10 mole-% acceptor-doped (a) $BaZrO_3$ and (b) ZrO_2 at 600 K in wet, reducing atmosphere ($p_{H_2O} = 0.03$ atm and $p_{O_2} = 10^{-30}$ atm).

4.5 Size effects

In nanostructured materials, one may distinguish between trivial and true size effects. In the former, the chemistry of an interface is independent of the presence of other interfaces such that macroscopic properties are only affected by the density of interfaces. In contrary, true size effects refer to situations where confinement effects and space charge zone overlap affect the charge carrier distribution and possibly also the formation energy of defects. Thus, true size effects result in a non-linear behaviour in the macroscopic properties when decreasing the particle size. In Manuscript II, the effect of space-charge overlap has been considered, showing that true size effects become significant when the particle size in the acceptor-doped $BaZrO_3$/donor-doped $SrTiO_3$ system is smaller than 5 nm. Due to depletion of mobile defects in both materials, the resulting electroneutrality of the heterostructures was dominated by donors in $SrTiO_3$ that are charge compensated by acceptors in $BaZrO_3$. In the case of undoped $BaZrO_3$, the space-charges extend to several nm, and size effects therefore occur even in large particles. However, due to rapid decay of the electrostatic potential as a function of the distance

from the interface plane, size effects may be neglected for particles that larger than ~10 nm. These effects are more important in very small particles where defect enrichment in the undoped material may lead to significantly improved ion transport. **Fig. 12** shows the defect concentration profiles in 2 nm thin films of acceptor-doped $BaZrO_3$ or ZrO_2 and undoped $BaZrO_3$. In the former system, decreasing the layer thickness would at some point cause the defect concentration to be constant throughout the heterostructure, which thus allows ion transport both along and across the interface. The concentration of defects in undoped $BaZrO_3$ may approach unity if ZrO_2 is used as a doped second phase and its thickness is larger than that of $BaZrO_3$ as a consequence of favoured segregation to the latter. Finally, it should be mentioned that local effects, *i.e.* strain and overlap of structural distortions around defects, have not been included, although these may affect the formation energy of defects even in relatively large particles.

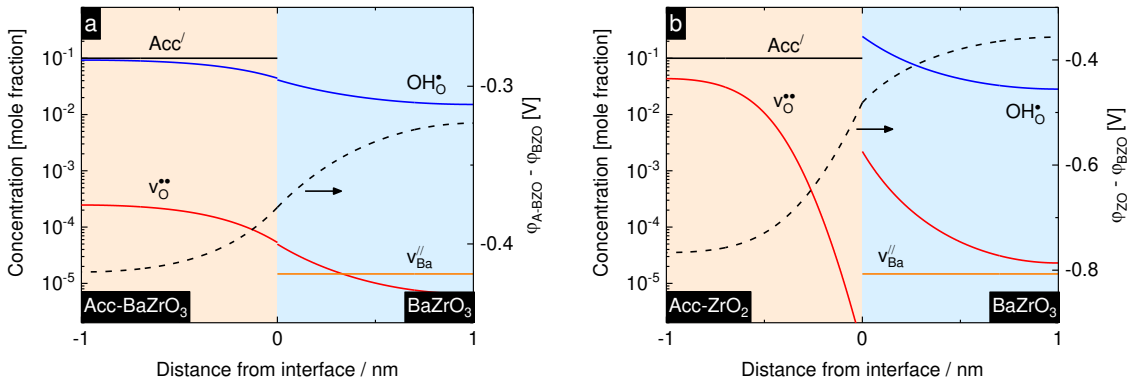

Fig. 12. The defect concentration profiles across the interface between undoped $BaZrO_3$ and 10 mole-% acceptor-doped (a) $BaZrO_3$ or (b) ZrO_2 at 600 K in wet, reducing atmosphere ($p_{H_2O} = 0.03$ atm and $p_{O_2} = 10^{-30}$ atm).

In the limit of an infinitely thin second phase, *i.e.* when the extent is limited to a single atomic plane, heterogeneous doping can be considered as layered homogeneous doping since the concentration of mobile defects becomes fixed by that of aliovalent ions in the dopant plane. Two alternatives exist for charge compensation within this limit; either as in homogeneously doped materials – where the dopant-plane (and possibly nearest planes) is subject to local electroneutrality, or as in heterogeneously doped materials – where charge compensation occurs through formation of space-charge layers. Though, a combination of both represents a more likely third alternative.

Which alternative that dominates would have a significant impact on the transport properties of the material. For instance in the first alternative, it is very likely that the presence of many acceptors on a single atomic plane may affect the formation energy and even cause ordering of defects in it. In such a case, the mobility of defects may be significantly lower than in a homogeneously doped material with a random distribution of dopants. In the other alternative – where the dopant plane is charge compensated by a space-charge layer – a significant number of defects would be distant from the dopant plane (**Fig. 13**) and thus exhibit a mobility that is higher than in a homogeneously doped material due to the absence of association between charge carriers and dopants. Also in this limit, the concentration of charge carriers is independent of temperature, which only affects the spatial extent of the space-charge layers. The defect concentration profiles as a function of distance from the dopant plane at different temperatures are presented in **Fig. 13**, which shows that above 600 K, $v_O^{\bullet\bullet}$ constitutes a significant contribution to the overall concentration of mobile charge carriers despite of being minority defects in the bulk. Though, most of these $v_O^{\bullet\bullet}$ may be strongly associated with the dopants and thus contribute little to the total electrical conductivity. **Fig. 14** shows the charge of $v_O^{\bullet\bullet}$ and $OH_O^{\bullet}$ that compensates the dopants – above 850 K $v_O^{\bullet\bullet}$ are the dominating defects although they would have been in minority for homogeneously doped $BaZrO_3$ at this temperature. This indicates that the chemistry of nano-structured solids may differ significantly from that of bulk materials. Decreasing the distance between the dopant planes does not affect the ratio of the concentration of $v_O^{\bullet\bullet}$ and $OH_O^{\bullet}$.

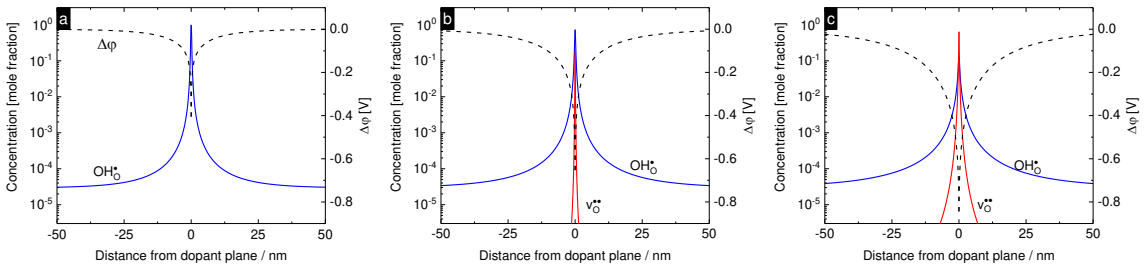

Fig. 13. The defect concentration and potential profiles as a function of distance from the dopant-plane at (a) 300, (b) 600 and (c) 1000 K.

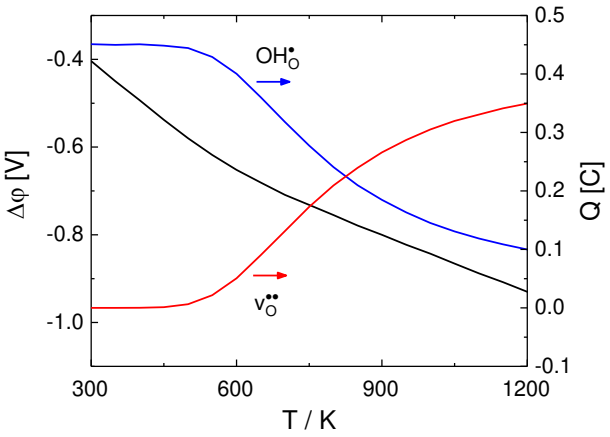

Fig. 14. The electrostatic potential difference at the dopant-plane relative to that in bulk and charge due to different defects in the space-charge zone. Note that the sum of charges is constant due to the electroneutrality requirement.

4.6 Electrical conductivity

Among the advantages of heterogeneous doping is the possibility for omitting substitutional dopants, which thus eliminates charge carrier trapping and results in higher electrical conductivity than in the homogeneously doped counterpart. For instance in $BaZrO_3$, the activation energy for proton transport, $E_{a,OH_O^\bullet}$, is 0.45 eV of which 0.29 eV is due to association between $OH_O^\bullet$ and the commonly used Y-dopant [2]. As shown in Manuscript V, doping on the A-site of the perovskite structure, may reduce the association energy by 0.10 - 0.15 eV for dopants that exhibit a significant solubility. Indeed, such reduction would result in a substantial increase in the conductivity; however, in unsubstituted $BaZrO_3$, $E_{a,OH_O^\bullet}$ is only 0.16 eV, which would significantly improve the conductivity at lower temperatures. **Fig. 15** shows the measured bulk conductivity of 10 mole-% acceptor-doped $BaZrO_3$ and ZrO_2, and that calculated for undoped $BaZrO_3$ assuming an activation energy of 0.20 eV and a $OH_O^\bullet$ concentration of 10 mole-%. At 0 °C, the conductivity in undoped $BaZrO_3$ is 20 mS/cm, 4 orders of magnitude higher than in the acceptor-doped counterpart. Nonetheless, such a high defect concentration, as assumed in the calculations of **Fig. 15**, may be difficult to achieve in a heterogeneously doped material unless the particle size is reduced to a few nm, where strain/"lattice distortion" may affect the carrier mobility. In addition, significant change in the defect concentration near interfaces may also affect the mobility. In composites of TiO_2 and $CsHSO_4$, low temperature superprotonic phase transition near interfaces in the latter was

ascribed to high concentration of proton vacancies near the interface.[32] Likewise, a significant enrichment of defects near interfaces may pose significant deviations in the mobility of charge carriers. **Fig. 16** illustrates how saturation of available lattice sites with $OH_O^{\bullet}$ may result in long range transport similar to the Grotthuss mechanism in water.

The high conductivity in the undoped phase suggests that even a limited number of interfaces may have a significant contribution to the total conductivity, as long as these are percolating. **Fig. 16** shows the conductance of thin films of acceptor-doped $BaZrO_3$ and ZrO_2 with and without a 5 nm thick layer of undoped $BaZrO_3$ as a function of thickness of the doped phases. The conductance of the $BaZrO_3$ film becomes independent of thickness below 100 nm reflecting that it is dominated by transport in the undoped layer. Due to lower conductivity in ZrO_2, its conductance is exceeded by that of the undoped $BaZrO_3$ layer at a thickness of 100 µm, below which the total conductivity is dominated by $OH_O^{\bullet}$. As such, nanostructured electrolytes may result in higher performance and smaller electrochemical devices than traditional electrolytes. Moreover, concentration enhancement near heterogeneous interfaces may compensate defect depletion at grain boundaries perpendicular to the phase boundary, which may further enhance the performance.

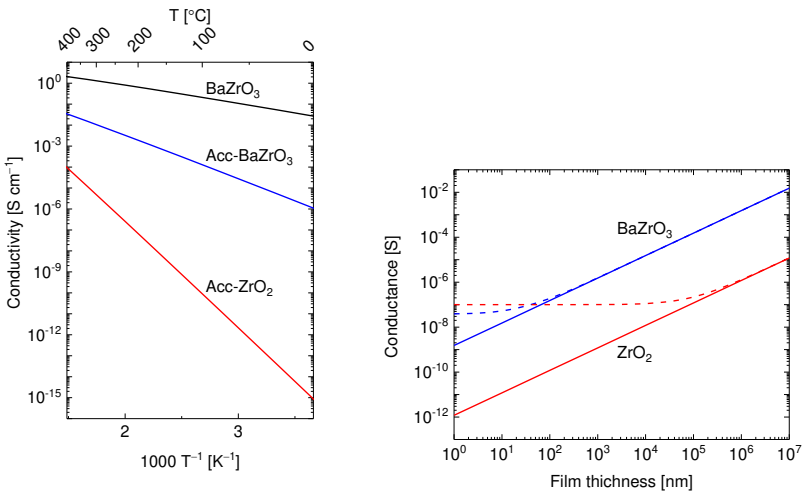

Fig. 15. The bulk conductivity in undoped $BaZrO_3$ and 10 mole-% acceptor-doped $BaZrO_3$ and ZrO_2 as a function of inverse temperature (a), and the calculated in-plane electrical conductance in films of 10 mole-% acceptor-doped $BaZrO_3$ and ZrO_2 (solid lines) compared to the same films containing one interface with undoped $BaZrO_3$ (dished lines) as a function of thickness. The conductivity of undoped $BaZrO_3$ is calculated assuming the same defect concentration as in the 10 mole-% acceptor-doped $BaZrO_3$. The distance between electrodes is 1 cm in (b). The conductivity data for the doped materials is extracted from references [66] and [67].

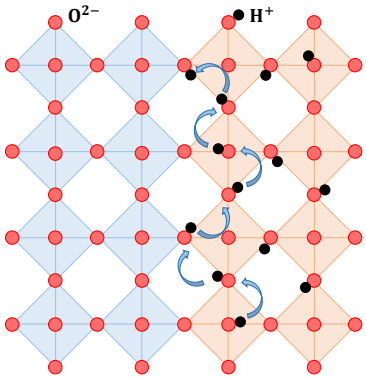

Fig. 16. A schematic of a possible transport mechanism (similar to the Grotthuss mechanism) near interfaces where the lattice sites are nearly saturated with $OH_O^{\bullet}$.

4.7 Segregation energy trends

Knowledge of the relative stability of defects in various materials is essential for describing their interface defect chemistry, and allows for prediction of the macroscopic properties of nanostructured composites and heterostructures. Measurement of relative defect stability is nontrivial and correlations with other, accessible physical and thermochemical parameters are therefore instrumental as a predictive tool in the search for materials with specific interfacial properties. As previously described in this thesis, the relative stability of defects is governed both by their standard chemical potentials and a configurational component, where the former reflects the chemical bond strength, while the latter is controlled by external factors such as doping, thermal and atmospheric conditions. The standard term is obtained by calculating the formation energy of defects with respect to the vacuum level.

Fig. 17 shows the calculated standard chemical potentials (*i.e.* standard segregation energies) for $v_O^{\bullet\bullet}$ and $OH_O^{\bullet}$ relative to those in $BaZrO_3$ for selected binary and ternary oxides, in which the ions exhibit a noble gas electron configuration. The figure shows a clear trend where the segregation energy of $v_O^{\bullet\bullet}$ (**Fig. 17a**) decreases (becomes more negative) down a group and increases (become more positive) to the right across a period in the periodic table of the elements (this also applies for ternary oxides). The same trend applies for the segregation energy of $OH_O^{\bullet}$ (**Fig. 17b**), both in-line with the findings in the work by Bjørheim *et. al.* [68], who studied the trend in $v_O^{\bullet\bullet}$ and $OH_O^{\bullet}$ affinity in in oxides, reporting a correlation between the affinity and ionization potential. As discussed by Bjørheim *et. al.* [68], the trend in $v_O^{\bullet\bullet}$ and $OH_O^{\bullet}$ affinity is similar to the trend in the electronegativity of the elements across the periodic table,

and a correlation between these is natural to expect. The electronegativity, in turn, is related to the ionization energy (for instance the Mulliken electronegativity is the average of the ionization energy and electron affinity, and is also proportional to the Pauling electronegativity) and would as such also correlate with the hydration enthalpy. Since the valence band of oxides with cations having noble gas configuration consist of oxygen states, relating the above mentioned properties to the ionization energy (which for a solid is equivalent to the valence band maximum) should give a better fit, at least for $v_O^{\bullet\bullet}$ as the valence band position reflects the O-bond strength.([68] and references therein)

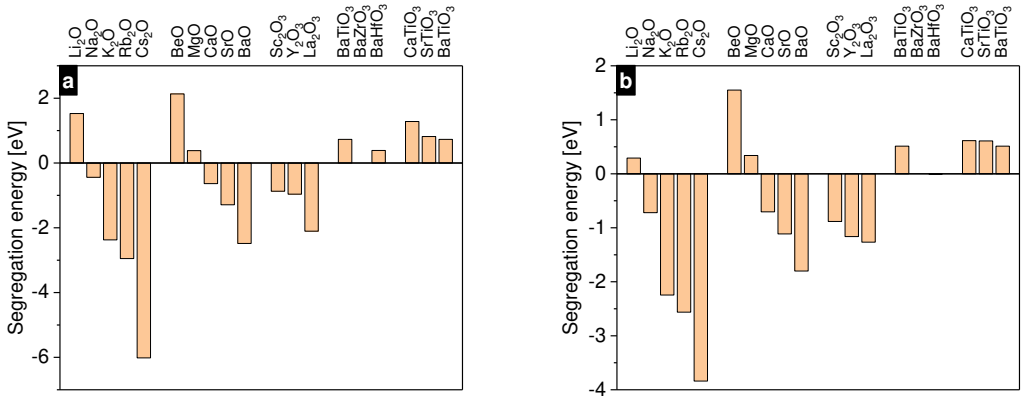

Fig. 17. The standard energy for segregation of $v_O^{\bullet\bullet}$ (a) and $OH_O^{\bullet}$ (b) from a range of binary and ternary oxides to $BaZrO_3$. Negative values indicate favourable segregation to $BaZrO_3$.

Fig. 18a and **b** respectively show the energy for segregation of $v_O^{\bullet\bullet}$ and $OH_O^{\bullet}$ with respect to $BaZrO_3$ as a function of the ionization potential. For the considered oxides, the segregation energy of $v_O^{\bullet\bullet}$ exhibits little scatter, and for materials within one group, the scattering is negligible. Moreover, when considered separately, the different material groups exhibit similar slopes, but different Y-intercept. This may indicate that structural parameters, such as coordination, and charge of the cations may play a systematic role and has to be considered. A linear fit to the data in **Fig. 18a** gives

$$E_{v_O^{\bullet\bullet}}^{seg} = -8.04IE + 1.71 \text{ eV}, \tag{36}$$

which offers a reasonable prediction of the segregation energy of $v_O^{\bullet\bullet}$, $E_{v_O^{\bullet\bullet}}^{seg}$, given the ionization energy, IE, of the oxide is known. Contrary to $v_O^{\bullet\bullet}$, the segregation energy of $OH_O^{\bullet}$ is somewhat more scattered, and the scatter is less systematic, which may be due to the H-states being deeper

and stability of the O-H bond, as such, not directly related to the valence band top. In addition, coordination and interatomic distances may affect the strength of hydrogen bonds and thereby the stability of $OH_O^{\bullet}$. Fitting the data in **Fig. 18b** gives

$$E_{OH_O^{\bullet}}^{seg} = -6.42IE + 1.27 \text{ eV}. \quad (37)$$

Fig. 18 and Eq. (36) and (37) and as such predicts the direction of segregation of $OH_O^{\bullet}$ and $v_O^{\bullet\bullet}$ to $BaZrO_3$, based on their electronic structure. Oxides with smaller ionization potential than $BaZrO_3$ will lead to segregation of $OH_O^{\bullet}$ and $v_O^{\bullet\bullet}$ to $BaZrO_3$ and as such act as a heterogeneous acceptors, while oxides with larger ionization potential acts as heterogeneous dopants, causing depletion of these defects.

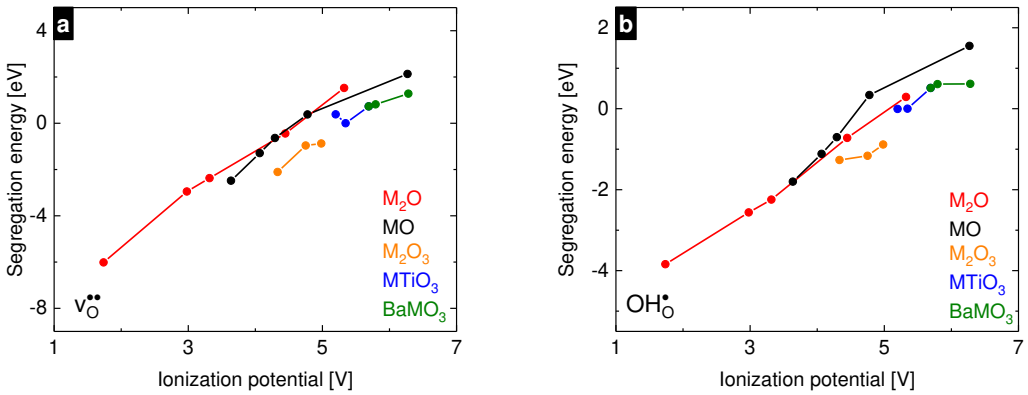

Fig. 18. The energy for segregation of $v_O^{\bullet\bullet}$ (a) and $OH_O^{\bullet}$ (b) from a range of binary and ternary oxides to $BaZrO_3$ as a function of oxides' ionization potential, showing a clear correlation between the two parameters. Negative values indicate favourable segregation to $BaZrO_3$.

4.8 The role of space-charge in catalysis

Although not the topic of this thesis, the relevance of space-charge formation at metal-oxide interfaces to catalysis is mentioned here, briefly. It is well known that the choice of support material, which typically is a solid oxide, affects the catalytic activity of metal nanoparticles [69-73]. Indeed, one possibility is the participation of the support surface in the chemical reactions as reported by for instance Mudiyanselage *et al.* [16]. The other possibility is that space-charge formation at the contact between the metal and the oxide both affects the concentration of point defects at and under the oxide surface (in the immediate vicinity of the metal), and the electronic properties of the metal itself. The former is particularly relevant for

electrocatalysis where for instance incorporation of H^+ or O^{2-} is involved but may also affect heterogeneous reactions, such as O_2 splitting on the surface. The second consequence of space-charge is related to enrichment or depletion of electrons in the metal, which thus affects the filling and center position of the *d*-band. As shown in Manuscript IV, the electrostatic potential at metal-oxide interfaces may be substantial, and lead to significant charging of a supported metal particle. In heterogeneous catalysis, the *d*-band center relative to the Fermi level is used to predict the binding energy of adsorbates on transition metal surfaces. The two properties correlate linearly and it is well established that the closer the *d*-band center is to the Fermi level, the stronger the interaction between the adsorbate and the metal surface, while lower *d*-band center results in weaker binding between the adsorbate and the surface [74-76]. This trend has been confirmed for oxygen adsorption on various transition metals [74, 76-78]. As such, space-charge is expected to influence the catalytic properties of supported metal particles. The change in *d*-band center imposed by space-charge depends on the charge transferred (*i.e.* sign and magnitude of the space-charge potential, and contact area between the metal and the oxide) and surface area of the metal particle (as the charge within a metal particle is mainly distributed at the surface, such that the particle interior is not affected).

4.9 Thermo-electrochemical splitting of H_2O

Manuscript I and II show that changes in control parameters can affect Φ, and result in a significant amount of charge/mass that is reversibly exchanged with the surroundings. In addition, Manuscript IV demonstrates that application of external electrical potential using blocking electrodes results in chemical capacitances close to 200 $\mu F/cm^2$, which is close to that of the best state of the art supercapacitors that employ redox active electrodes [79], but exhibits no overall mass storage (although mass is locally stored at each of the electrodes). However, in a chemical capacitor with an asymmetric electrolyte, both mass and charge may be stored and even production of H_2 may be possible, as described below.

Fig. 19 shows the capacitance and energy density, and charge density as a function of applied voltage for a capacitor composed of acceptor-doped $BaZrO_3$/undoped CeO_2 electrolyte with Pt electrodes. The capacitance exceeds 0.4 F/m^2 (40 $\mu F/cm^2$), which is significantly lower than when single-phase acceptor-doped $BaZrO_3$ is used as electrolyte. Upon application of a weakly negative potential (*i.e.* low potential on $BaZrO_3$), electrons and protons are enriched at the

CeO_2/Pt and $BaZrO_3$/Pt interfaces, respectively. At more negative potentials, also $v_O^{\bullet\bullet}$ are enriched in $BaZrO_3$. As such, charging the capacitor with a weakly negative potential (higher than −1.5 V) results in release of O_2. During discharge, H_2 is released, and the energy output is thus higher than the energy input (under the prerequisite of wet, H_2 poor atmosphere). Ideally, such charge-discharge may be maid self-sustaining at the cost of thermal energy. Upon charging with a positive potential, protons at the $BaZrO_3$/Pt interface are depleted, while $v_O^{\bullet\bullet}$ at the CeO_2/Pt interface are enriched, such that the overall process during charging or discharging corresponds to release or incorporation, respectively, of H_2O.

The chemistry of the charging-discharging process under negative potential corresponds to reduction of Ce^{4+} to Ce^{3+} and oxidation of O^{2-} in H_2O to O_2 under charging, and oxidation of Ce^{3+} and reduction of H^+ in $BaZrO_3$ under discharging. The heterogeneous defect reactions are

$$2O_O^{\times} + 2Ce_{Ce}^{\times} + H_2O(g) \rightleftharpoons 2OH_O^{\bullet} + 2Ce'_{Ce} + {}^1\!/_2\, O_2(g) \qquad (38)$$

and

$$OH_O^{\bullet} + Ce'_{Ce} \rightleftharpoons O_O^{\times} + Ce_{Ce}^{\times} + {}^1\!/_2\, H_2(g). \qquad (39)$$

The process is in some way equivalent to thermochemical H_2O splitting, where for instance CeO_2 is thermally reduced to Ce_2O_3 (Ce^{3+}) at high temperature and subsequently oxidized by H_2O at lower temperature, releasing H_2 [80-82]. However, in the process described above, which we term "thermo-electrochemical process", there is no need for thermal cycling and the process may be conducted at low temperatures since no oxide ion diffusion or structural changes are involved, such that for instance waste heat from other industrial processes may be utilised. It should be noticed that the extent of reactions (38) and (39) is not governed by the redox thermodynamic, but rather by the space-charge thermodynamics, which also involve electrical potential.

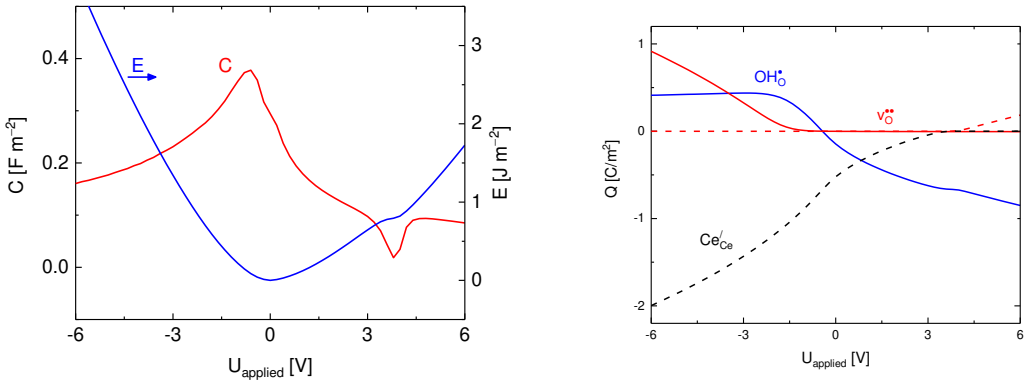

Fig. 19. Chemical capacitance and energy density (a) and charge density (b) as a function of applied voltage for a capacitor of acceptor-doped $BaZrO_3$/undoped CeO_2 at 600 K.

5 Conclusions and outlook

The fundamentals of the defect chemistry of heterointerfaces have been investigated by means of first principles calculations. The work has been focused on the interfaces between Ni and Cu group metals or $SrTiO_3$ and $BaZrO_3$ as model systems, although a wide range of materials has been considered, as well. The work addresses the possibility for tailoring the defect chemistry of interfaces, and the prospect for new applications based on interfacial effects.

Homogeneous doping represents an efficient means to improve the conductivity of materials by increasing the concentration of charged defects. However, it is well known that association between mobile defects and, for instance, the acceptor dopant significantly increases the activation energy of the charge carrier mobility compared to that in the undoped material. The association energy can be reduced through doping the $A^{II}B^{IV}O_3$ perovskite structure on A-site, rather than the common approach of doping on the B-site. The calculations performed here show that A-site doping of $BaZrO_3$ can reduce the activation energy of $OH_O^{\bullet}$ mobility by 0.1 eV compared to B-site doped $BaZrO_3$, where the association energy amounts to 0.29 eV. Yet, heterogeneous doping is a better approach to improve the electrical conductivity as separation of transporting and charge compensating defects completely eliminates defect association. The estimated conductivity of heterogeneously doped $BaZrO_3$ at room temperature is 20 mS/cm, which is four orders of magnitude higher than that of homogeneously (Y) doped $BaZrO_3$, and thus can enable room temperature applications of proton conducting oxides.

A model to calculate the formation energy of defects on an absolute scale, allowing determination of their relative stability in different material, has been developed and used to calculate the segregation energy of $OH_O^{\bullet}$ and $v_O^{\bullet\bullet}$ for a wide range of materials. The results show that defect's segregation energies scale with the ionization potential of the undoped oxides, suggesting that oxides with larger ionization potential than $BaZrO_3$ act as heterogeneous acceptors, causing enrichment of $OH_O^{\bullet}$ and $v_O^{\bullet\bullet}$ near the interface. On the other hand, oxides that exhibit smaller ionization potential than $BaZrO_3$ act as heterogeneous donors, causing depletion of these defects in the near-interface region of $BaZrO_3$. As such, the ionization potential of oxides can be used as a tool to predict the defect chemistry of heterointerfaces.

Calculations on the $BaZrO_3/SrTiO_3$ interface show that $OH_O^{\bullet}$ and $v_O^{\bullet\bullet}$ are stabilised by 0.58 and 0.64 eV, respectively, in $BaZrO_3$ relative to $SrTiO_3$. Consequently, the electrostatic potential

difference across the interface with respect to $BaZrO_3$, Φ, is negative, resulting in enrichment and depletion of all positively charged defects in acceptor-doped $BaZrO_3$ and $SrTiO_3$, respectively. Transfer of charged defects across the interface corresponds to a heterogeneous doping effect where $BaZrO_3$ becomes acceptor-doped while $SrTiO_3$ becomes donor-doped near the interface. Contrary to homogeneous doping, the heterogeneous doping effect is temperature dependent as a consequence of the temperature dependence of Φ, which is given by the segregation thermodynamics of the involved defects. It is shown that the concentration of defects in the bulk of the individual materials plays an important role, and can even result in reversal of the direction of defect segregation, as the situation is at the interfaces between acceptor-doped $BaZrO_3$ and undoped or donor-doped $SrTiO_3$.

At the interface between acceptor-doped $BaZrO_3$ and donor-doped $SrTiO_3$, $OH_O^{\bullet}$ and electrons in the respective materials are depleted, such that the resulting situation is similar to that at a *pn*-junction between semiconductors. As such, a nanocomposite based on an ionic "*pn*-junction" is not suitable for application as an electrode or a gas separation membrane, where the performance relies on ambipolar conductivity of ionic and electronic charge carriers. However, it is shown that the change in the stoichiometry of $OH_O^{\bullet}$ and electrons at the interface can be utilized for H_2 storage and/or thermochemical splitting of H_2O (similar to that in for instance CeO_2).

The role of space-charge at metal/oxide interfaces on the performance of negative electrodes (negatrodes) have been addressed. It is shown that for most metals, charge carriers are enriched at the interface at typical operation temperatures of electrochemical devices, suggesting that the charge transfer resistance is controlled by other steps than diffusion through the space-charge layer. However, at lower temperatures, depletion of charge carriers at the interface may reduce, or even limit, the performance of the negatrode. Moreover, it is shown that polarization at the metal/oxide contact can result in significant capacitances of up to 240 $\mu F/cm^2$, suggesting that proton conducting oxides may serve as promising electrolytes in solid state super capacitors. Finally, the results show that the polarization at metal/oxide interfaces may be utilized in electrical-field-assisted thermochemical splitting of H_2O, which in the thesis has been termed "thermo-electrochemical" H_2O splitting.

Altogether, the thesis emphasizes the potential of heterogeneous modification of materials a strategy to improve the functional properties of electrochemical devices beyond what can be

achieved by single-phase materials, and the prospect for new applications based on heterointerfaces. In the thesis it is shown that not only the choice materials can be used to tailor the properties of interface, but also the strain at the interface and the bulk concentrations, which both can be modified by homogeneous doping. In addition, control of temperature and atmospheric conditions represent additional degrees of freedom to modify the interface chemistry.

References

1. Bi, Z., et al., *Effect of Ca doping on the electrical conductivity of the high temperature proton conductor $LaNbO_4$.* International Journal of Hydrogen Energy, 2012. **37**(17): p. 12751-12759.
2. Yamazaki, Y., et al., *Proton Trapping in yttrium-doped barium zirconate.* Nat. Mater., 2013. **12**: p. 647.
3. Björketun, M.E., P.G. Sundell, and G. Wahnström, *Effect of acceptor dopants on the proton mobility in $BaZrO_3$: A density functional investigation.* Physical Review B, 2007. **76**(5): p. 054307.
4. Karlsson, M., et al., *Using Neutron Spin−Echo To Investigate Proton Dynamics in Proton-Conducting Perovskites.* Chemistry of Materials, 2010. **22**(3): p. 740-742.
5. Kjølseth, C., et al., *Space–charge theory applied to the grain boundary impedance of proton conducting $BaZr_{0.9}Y_{0.1}O_{3-\delta}$.* Solid State Ionics, 2010. **181**(5): p. 268-275.
6. Tschöpe, A., E. Sommer, and R. Birringer, *Grain size-dependent electrical conductivity of polycrystalline cerium oxide: I. Experiments.* Solid State Ionics, 2001. **139**(3): p. 255-265.
7. Chiang, Y.M., et al., *Defect and transport properties of nanocrystalline CeO_{2-x}.* Applied Physics Letters, 1996. **69**(2): p. 185-187.
8. Kreuer, K.D., *Proton-Conducting Oxides.* Annual Review of Materials Research, 2003. **33**(1): p. 333-359.
9. Bohn, H.G. and T. Schober, *Electrical Conductivity of the High-Temperature Proton Conductor $BaZr_{0.9}Y_{0.1}O_{2.95}$.* Journal of the American Ceramic Society, 2000. **83**(4): p. 768-772.
10. Duval, S.B.C., et al., *Electrical conductivity of the proton conductor $BaZr_{0.9}Y_{0.1}O_{3-\delta}$ obtained by high temperature annealing.* Solid State Ionics, 2007. **178**(25): p. 1437-1441.
11. De Souza, R.A., *The formation of equilibrium space-charge zones at grain boundaries in the perovskite oxide $SrTiO_3$.* Physical Chemistry Chemical Physics, 2009. **11**(43): p. 9939-9969.
12. Brinkman, A., et al., *Magnetic effects at the interface between non-magnetic oxides.* Nature Materials, 2007. **6**: p. 493.
13. Lüders, U., et al., *Room-temperature magnetism in $LaVO_3/SrVO_3$ superlattices by geometrically confined doping.* Physical Review B, 2009. **80**(24): p. 241102.
14. Ohtomo, A. and H.Y. Hwang, *A high-mobility electron gas at the $LaAlO_3/SrTiO_3$ heterointerface.* Nature, 2004. **427**: p. 423.
15. Reyren, N., et al., *Superconducting Interfaces Between Insulating Oxides.* Science, 2007. **317**(5842): p. 1196-1199.
16. Mudiyanselage, K., et al., *Importance of the Metal–Oxide Interface in Catalysis: In Situ Studies of the Water–Gas Shift Reaction by Ambient-Pressure X-ray Photoelectron Spectroscopy.* Angewandte Chemie International Edition, 2013. **52**(19): p. 5101-5105.
17. Liang, C.C., *Conduction Characteristics of the Lithium Iodide-Aluminum Oxide Solid Electrolytes.* Journal of The Electrochemical Society, 1973. **120**(10): p. 1289-1292.
18. Yamada, H., A.J. Bhattacharyya, and J. Maier, *Extremely High Silver Ionic Conductivity in Composites of Silver Halide (AgBr, AgI) and Mesoporous Alumina.* Advanced Functional Materials, 2006. **16**(4): p. 525-530.
19. Chen, C.-C. and J. Maier, *Decoupling electron and ion storage and the path from interfacial storage to artificial electrodes.* Nature Energy, 2018. **3**(2): p. 102-108.

20. Fu, L., et al., *"Job-Sharing" Storage of Hydrogen in Ru/Li_2O Nanocomposites.* Nano Letters, 2015. **15**(6): p. 4170-4175.
21. Li, H., P. Balaya, and J. Maier, *Li-Storage via Heterogeneous Reaction in Selected Binary Metal Fluorides and Oxides.* Journal of The Electrochemical Society, 2004. **151**(11): p. A1878-A1885.
22. Fu, L., et al., *Thermodynamics of Lithium Storage at Abrupt Junctions: Modeling and Experimental Evidence.* Physical Review Letters, 2014. **112**(20): p. 208301.
23. Lauer, U. and J. Maier, *Conductivity enhancement and microstructure in AgCl/AgI composites.* Solid State Ionics, 1992. **51**(3): p. 209-213.
24. Jin-Phillipp, N.Y., et al., *Structures of BaF_2–CaF_2 heterolayers and their influences on ionic conductivity.* The Journal of Chemical Physics, 2004. **120**(5): p. 2375-2381.
25. Maier, J., *Heterogeneous doping of silver bromide (AgBr:Al_2O_3).* Materials Research Bulletin, 1985. **20**(4): p. 383-392.
26. Kliewer, K.L., *Space charge in ionic crystals-III. Silver halides containing divalent cations.* Journal of Physics and Chemistry of Solids, 1966. **27**(4): p. 705-717.
27. Balaya, P., et al., *Fully Reversible Homogeneous and Heterogeneous Li Storage in RuO_2 with High Capacity.* Advanced Functional Materials, 2003. **13**(8): p. 621-625.
28. Yu, X.Q., et al., *Reversible lithium storage in LiF/Ti nanocomposites.* Physical Chemistry Chemical Physics, 2009. **11**(41): p. 9497-9503.
29. Zhukovskii, Y.F., et al., *Evidence for Interfacial-Storage Anomaly in Nanocomposites for Lithium Batteries from First-Principles Simulations.* Physical Review Letters, 2006. **96**(5): p. 058302.
30. Yang, N., et al., *Defective Interfaces in Yttrium-Doped Barium Zirconate Films and Consequences on Proton Conduction.* Nano Letters, 2015. **15**(4): p. 2343-2349.
31. Foglietti, V., et al., *Heavily strained $BaZr_{0.8}Y_{0.2}O_{3-x}$ interfaces with enhanced transport properties.* Applied Physics Letters, 2014. **104**(8): p. 081612.
32. Chan, W.K., et al., *Direct View on Nanoionic Proton Mobility.* Advanced Functional Materials, 2011. **21**(8): p. 1364-1374.
33. Haverkate, L.A., W.K. Chan, and F.M. Mulder, *Large space-charge effects in a nanostructured proton conductor.* Advanced Functional Materials, 2010. **20**(23): p. 4107-4116.
34. Polfus, J.M., T. Norby, and R. Bredesen, *Proton segregation and space-charge at the $BaZrO_3$ (0 0 1)/MgO (0 0 1) heterointerface.* Solid State Ionics, 2016. **297**: p. 77-81.
35. Matsumoto, H., et al., *Nanoprotonics in perovsikte-type oxides: Reversible changes in color and ion conductivity due to nanoionics phenomenon in platinum-containing perovskite oxide.* Solid State Ionics, 2011. **182**(1): p. 13-18.
36. Tong, J., et al., *Electrical conductivities of nano ionic composite based on yttrium-doped barium zirconate and palladium metal.* Solid State Ionics, 2012. **211**: p. 26-33.
37. Caldes, M.T., et al., *Metallic Nanoparticles and Proton Conductivity: Improving Proton Conductivity of $BaCe_{0.9}Y_{0.1}O_{3-\delta}$ Using a Catalytic Approach.* Chemistry of Materials, 2012. **24**(24): p. 4641-4646.
38. Kasamatsu, S., T. Tada, and S. Watanabe, *Theoretical analysis of space charge layer formation at metal/ionic conductor interfaces.* Solid State Ionics, 2011. **183**(1): p. 20-25.
39. Kasamatsu, S., T. Tada, and S. Watanabe, *Parallel-sheets model analysis of space charge layer formation at metal/ionic conductor interfaces.* Solid State Ionics, 2012. **226**: p. 62-70.
40. Tauer, T., R. O'Hayre, and J.W. Medlin, *An ab Initio Investigation of Proton Stability at $BaZrO_3$ Interfaces.* Chemistry of Materials, 2014. **26**(17): p. 4915-4924.

41. Malagoli, M., et al., *Protons crossing triple phase boundaries based on a metal catalyst, Pd or Ni, and barium zirconate.* Phys. Chem. Chem. Phys., 2013. **15**: p. 12525.
42. Hohenberg, P. and W. Kohn, *Inhomogeneous Electron Gas.* Physical Review, 1964. **136**(3B): p. B864-B871.
43. Kohn, W. and L.J. Sham, *Self-Consistent Equations Including Exchange and Correlation Effects.* Physical Review, 1965. **140**(4A): p. A1133-A1138.
44. Hafner, J., *Ab-initio simulations of materials using VASP: Density-functional theory and beyond.* Journal of Computational Chemistry, 2008. **29**(13): p. 2044-2078.
45. Perdew, J.P., K. Burke, and M. Ernzerhof, *Generalized Gradient Approximation Made Simple.* Physical Review Letters, 1996. **77**(18): p. 3865-3868.
46. Heyd, J., G.E. Scuseria, and M. Ernzerhof, *Hybrid functionals based on a screened Coulomb potential.* The Journal of Chemical Physics, 2003. **118**(18): p. 8207-8215.
47. Heyd, J., G.E. Scuseria, and M. Ernzerhof, *Erratum: "Hybrid functionals based on a screened Coulomb potential" [J. Chem. Phys. 118, 8207 (2003)].* The Journal of Chemical Physics, 2006. **124**(21): p. 219906.
48. Sholl, D.S. and J.A. Steckel, *Density Functional Theory: A Practical Introduction*. Density Functional Theory: A Practical Introduction. 2009. 1-238.
49. Kresse, G. and J. Hafner, *Ab initio molecular dynamics for liquid metals.* Physical Review B, 1993. **47**(1): p. 558-561.
50. Kresse, G. and J. Hafner, *Ab initio molecular-dynamics simulation of the liquid-metal--amorphous-semiconductor transition in germanium.* Physical Review B, 1994. **49**(20): p. 14251-14269.
51. Kresse, G. and J. Furthmüller, *Efficient iterative schemes for ab initio total-energy calculations using a plane-wave basis set.* Physical Review B, 1996. **54**(16): p. 11169-11186.
52. Kresse, G. and J. Furthmüller, *Efficiency of ab-initio total energy calculations for metals and semiconductors using a plane-wave basis set.* Computational Materials Science, 1996. **6**(1): p. 15-50.
53. Oba, F., et al., *Point defects in ZnO: an approach from first principles.* Science and Technology of Advanced Materials, 2011. **12**(3): p. 034302.
54. Togo, A. and I. Tanaka, *First principles phonon calculations in materials science.* Scripta Materialia, 2015. **108**: p. 1-5.
55. Maier, J., *Physical Chemistry of Ionic Materials: Ions and Electrons in Solids*. 2004, England: John Wiley & Sonds LTD.
56. Mattila, T. and A. Zunger, *Deep electronic gap levels induced by isovalent P and As impurities in GaN.* Physical Review B, 1998. **58**(3): p. 1367-1373.
57. Freysoldt, C., J. Neugebauer, and C.G. Van de Walle, *Fully Ab Initio Finite-Size Corrections for Charged-Defect Supercell Calculations.* Physical Review Letters, 2009. **102**(1): p. 016402.
58. Freysoldt, C., J. Neugebauer, and C.G. Van de Walle, *Electrostatic interactions between charged defects in supercells.* physica status solidi (b), 2011. **248**(5): p. 1067-1076.
59. Kumagai, Y. and F. Oba, *Electrostatics-based finite-size corrections for first-principles point defect calculations.* Physical Review B, 2014. **89**(19): p. 195205.
60. Komsa, H.-P., T.T. Rantala, and A. Pasquarello, *Finite-size supercell correction schemes for charged defect calculations.* Physical Review B, 2012. **86**(4): p. 045112.
61. Komsa, H.-P., T. Rantala, and A. Pasquarello, *Comparison between various finite-size supercell correction schemes for charged defect calculations.* Physica B: Condensed Matter, 2012. **407**(15): p. 3063-3067.

62. Paier, J., et al., *The Perdew-Burke-Ernzerhof exchange-correlation functional applied to the G2-1 test set using a plane-wave basis set.* J Chem Phys, 2005. **122**(23): p. 234102.
63. Roel van de, K. and G. Michael, *Photoelectrochemical Hydrogen Production, Chapter 2*. 2012: Springer US. 1-324.
64. Lindman, A., T.S. Bjørheim, and G. Wahnström, *Defect segregation to grain boundaries in $BaZrO_3$ from first-principles free energy calculations.* Journal of Materials Chemistry A, 2017. **5**(26): p. 13421-13429.
65. Okuda, T., et al., *Large thermoelectric response of metallic perovskites: $Sr_{1-X}La_XTiO_3$ ($0 < \sim x < \sim 0.1$).* Physical Review B, 2001. **63**(11): p. 113104.
66. Abelard, P. and J.F. Baumard, *The electrical conductivity of cubic stabilized zirconia The Results of an IUPAC Collaborative Study (Technical Report).* Pure and Applied Chemistry, 1995. **67**(11): p. 1891-1904.
67. Saeed, S.W., *The effect of metal nano-precipitates on the bulk and grain boundary conductivity of Y-doped $BaZrO_3$, M.Sc. thesis.* 2013.
68. Bjørheim, T.S., et al., *Proton, hydroxide ion, and oxide ion affinities of closed-shell metal oxides.* Submitted to Angewandte Chemie, July 2019, Presented at the 19th International Conference on Solid State Protonic Conductors, September 16-21, 2018, Stowe, VT, USA.
69. Cullis, C.F., T.G. Nevell, and D.L. Trimm, *Role of the catalyst support in the oxidation of methane over palladium.* Journal of the Chemical Society, Faraday Transactions 1: Physical Chemistry in Condensed Phases, 1972. **68**(0): p. 1406-1412.
70. Monyoncho, E.A., et al., *Role of the Metal-Oxide Support in the Catalytic Activity of Pd Nanoparticles for Ethanol Electrooxidation in Alkaline Media.* ChemElectroChem, 2016. **3**(2): p. 218-227.
71. Gadalla, A.M. and B. Bower, *The role of catalyst support on the activity of nickel for reforming methane with CO_2.* Chemical Engineering Science, 1988. **43**(11): p. 3049-3062.
72. Hernadi, K., et al., *On the role of catalyst, catalyst support and their interaction in synthesis of carbon nanotubes by CCVD.* Materials Chemistry and Physics, 2003. **77**(2): p. 536-541.
73. Jenness, G.R. and J.R. Schmidt, *Unraveling the Role of Metal–Support Interactions in Heterogeneous Catalysis: Oxygenate Selectivity in Fischer–Tropsch Synthesis.* ACS Catalysis, 2013. **3**(12): p. 2881-2890.
74. Hammer, B. and J.K. Nørskov, *Theoretical surface science and catalysis—calculations and concepts*, in *Advances in Catalysis*. 2000, Academic Press. p. 71-129.
75. Jeff Greeley, Jens K. Nørskov, and M. Mavrikakis, *ELECTRONIC STRUCTURE AND CATALYSIS ON METAL SURFACES.* Annual Review of Physical Chemistry, 2002. **53**(1): p. 319-348.
76. Tang, W. and G. Henkelman, *Charge redistribution in core-shell nanoparticles to promote oxygen reduction.* The Journal of Chemical Physics, 2009. **130**(19): p. 194504.
77. Mavrikakis, M., B. Hammer, and J.K. Nørskov, *Effect of Strain on the Reactivity of Metal Surfaces.* Physical Review Letters, 1998. **81**(13): p. 2819-2822.
78. Xu, Y., A.V. Ruban, and M. Mavrikakis, *Adsorption and Dissociation of O_2 on Pt-Co and Pt-Fe Alloys.* Journal of the American Chemical Society, 2004. **126**(14): p. 4717-4725.
79. Winter, M. and R.J. Brodd, *What Are Batteries, Fuel Cells, and Supercapacitors?* Chemical Reviews, 2004. **104**(10): p. 4245-4270.

80. Abanades, S. and G. Flamant, *Thermochemical hydrogen production from a two-step solar-driven water-splitting cycle based on cerium oxides.* Solar Energy, 2006. **80**(12): p. 1611-1623.
81. Bulfin, B., et al., *Thermodynamics of CeO_2 Thermochemical Fuel Production.* Energy & Fuels, 2015. **29**(2): p. 1001-1009.
82. Ishida, T., et al., *Kinetics of Thermal Reduction Step of Thermochemical Two-step Water Splitting Using CeO_2 Particles: MASTER-plot Method for Analyzing Non-isothermal Experiments.* Energy Procedia, 2014. **49**: p. 1970-1979.